

**Multiscale Lattice Boltzmann simulations
of droplet dynamics in time-dependent and
turbulent flows**

Felix Milan



This work is part of the European Union's Framework Programme for Research and Innovation Horizon 2020 (2014 - 2020) under the Marie Skłodowska-Curie Grant Agreement No.642069.

Cover image: Sub-Kolmogorov droplet in a homogeneous and isotropic turbulent flow.

Thesis printed by Gildeprint Drukkerijen, Enschede.

A catalogue record is available from the Eindhoven University of Technology Library

ISBN: 978-90-386-4936-8

Copyright © 2019 by Felix Milan, Eindhoven, The Netherlands.

All rights are reserved. No part of this publication may be reproduced, stored in a retrieval system, or transmitted, in any form or by any means, electronic, mechanical, photocopying, recording or otherwise, without prior permission of the author.

**Multiscale Lattice Boltzmann simulations
of droplet dynamics in time-dependent
and turbulent flows**

PROEFSCHRIFT

ter verkrijging van de graad van doctor aan de
Technische Universiteit Eindhoven, op gezag van de
rector magnificus, prof.dr.ir. F.P.T. Baaijens, voor een
commissie aangewezen door het College voor
Promoties in het openbaar te verdedigen
op woensdag 18 december 2019 om 13.30 uur

door

Felix Maria Niccolò Milan

geboren te Bamberg, Duitsland

Dit proefschrift is goedgekeurd door de promotoren en de samenstelling van de promotiecommissie is als volgt:

voorzitter: prof.dr.ir. G.M.W. Kroesen
1^e promotor: prof.dr. F. Toschi
2^e promotor: prof.dr. L. Biferale (Università degli Studi di Roma “Tor Vergata”)
copromotor(en): prof.dr. M. Sbragaglia (Università degli Studi di Roma “Tor Vergata”)
leden: prof.dr. P. Anderson
prof.dr. L. Brandt (KTH Stockholm)
dr.ir. W.-P. Breugem (Technische Universiteit Delft)

Het onderzoek of ontwerp dat in dit proefschrift wordt beschreven, is uitgevoerd in overeenstemming met de TU/e Gedragscode Wetenschapsbeoefening.

All details on simulations, data and scientific results shown in this thesis are recorded in the gitlab repository: <https://git.phys.tue.nl/phd/milan/blob/master/README.md>

Contents

1. Introduction	1
1.1. Motivation	1
1.2. Thesis outline	3
2. Theoretical Background	5
2.1. The equations of fluid flows	5
2.2. Multicomponent flows	6
2.3. Maffettone-Minale model (MM)	8
2.4. Turbulent flows	10
2.4.1. The Richardson energy cascade	12
2.4.2. The Kolmogorov microscales	14
3. The Lattice Boltzmann Method (LBM)	17
3.1. The Boltzmann and Lattice Boltzmann equation	17
3.2. The Chapman-Enskog Expansion (CEE)	22
3.3. Shan-Chen multicomponent model	23
3.4. Validation tests for confined droplets	24
3.5. A ghost node boundary flow scheme	28
4. Droplet in a time-dependent flow: LBM and MM comparison	31
4.1. Introduction	31
4.2. Static droplet deformation	33
4.3. Probing the parameter space: single component oscillating shear flow	35
4.4. Multicomponent oscillating flow	39
4.5. Conclusion	46
5. Droplet breakup in a confined and time-dependent flow	51
5.1. Introduction	51
5.2. Simulation set up and definitions	53
5.3. Droplet breakup in an oscillatory shear flow	55

5.4. Inertial effects	57
5.5. Confinement effects	59
5.6. Flow topology	63
5.7. Conclusion	65
6. LBM scheme for a sub-Kolmogorov droplet in HIT	67
6.1. Introduction	67
6.2. Structure of the algorithm	68
6.3. Validation results	69
6.4. Conclusion	73
7. Dynamics and breakup of a sub-Kolmogorov droplet in HIT	75
7.1. Introduction	75
7.2. Flow behaviour of the sub-Kolmogorov droplet	76
7.3. Breakup predictions: LBM vs MM	77
7.4. Conclusion	79
8. Conclusion and outlook	85
8.1. Droplets in laminar time-dependent flows	85
8.2. Sub-Kolmogorov droplets in turbulent flows	86
8.3. Outlook	86
A. Numerical solution of the MM-model	89
A.1. Simple shear flow	90
A.2. Uniaxial extensional flow	91
A.3. Planar hyperbolic flow	92
B. A linearised MM-model solution for an oscillatory shear flow	95
Bibliography	97
Summary	111
Acknowledgement	113
Curriculum Vitae	115
Cover Illustration	117

List of publications and conferences	119
---	------------

1. Introduction

1.1. Motivation

From natural occurring liquid aerosols, such as water droplets in clouds and mist, to industrially produced emulsions, such as cremes and pastes, droplets can be found almost anywhere in our everyday lives. It is therefore interesting to analyse the properties and in particular the dynamics of droplet suspensions. The focus in this work will be on stable droplet suspensions, i.e. the behaviour of two immiscible fluids, with the dispersed phase representing the droplet and the continuous phase the suspension. Droplet suspensions in liquids are called multicomponent systems, as they are comprised of two fluid components, the droplet and its suspension. On the other hand, bubbles in water or droplet aerosols would be examples of multiphase systems. A particularly interesting problem involving droplets is the mixing of two immiscible fluids, created by breakup of the droplets [1–4], which involves multiple scales and, in general, turbulent flow dynamics. The largest characteristic structures in turbulent flows are called eddies. In three dimensional turbulence the flow’s energy of the largest eddies is passed down to the smallest turbulent flow scales via a cascade mechanism, the Richardson cascade [5–8]. The droplets are typically of the size of the smallest scales. Consequently, the droplets may still be subjected to large shear and/or stress rates due to the Richardson cascade, which transfers energy from the largest eddies to the smallest scales. The mixing of the two immiscible fluids is achieved via the breakup of the droplets into smaller ones. A very first study on breakup of large droplets in turbulent flows was conducted by Hinze [9]. Further studies on droplet deformation in turbulence followed, both experimentally and numerically [10–13]. Numerical studies investigating small sub-Kolmogorov droplets, i.e. droplets with a characteristic length scale smaller than the Kolmogorov scale, used more sophisticated approaches, such as the one by Cristini et al. [14] coupling a pseudo-spectral solver for the outer flow with a boundary integral method to model the dynamics of the droplet. Furthermore Euler-Lagrangian approaches have been used to

simulate sub-Kolmogorov bubbles in turbulent Taylor-Couette flows [15]. A phenomenological model devised by Maffettone and Minale [16] has been used very effectively in conjunction with pseudo-spectral flow solvers to model the statistics of sub-Kolmogorov droplet dynamics and their breakup conditions [17, 18]. The Maffettone-Minale model is an extension to Taylor's theory, a perturbative approach to a droplet in Stokes flow [19–21]. Even in the absence of turbulence, droplet dynamics are complex flows to investigate and model [22–25], especially in the presence of strong confinement [26–38]. Theoretical models accounting for the effect of confinement exist as well, such as the Shapira-Haber model [39, 40] extending Taylor's theory [19, 20] and an extension to the Maffettone-Minale model [16] including the effect of confinement [41, 42]. Both the Shapira-Haber and the confined Maffettone-Minale model were experimentally validated [43, 44]. Further factors affecting the flow of multicomponent systems are the role of inertia [12, 25, 45–64], varying startup conditions [65–69] and the droplet dynamics in laminar time-dependent flows [70–74]. In order to model our multicomponent droplet system we use Lattice Boltzmann methods (LBM), which are a useful computational tool for the description of general multiscale flow problems. LBM's fame is due to its ability to couple physical phenomena on the microscale, such as interface dynamics, polymers and thermal fluctuations, and continuous hydrodynamical flows at the macroscopic scale, e.g. flow-structure coupling and capillary fluctuations. LBM are derived from physical laws on the mesoscale, but can describe macroscopic flow phenomena via a coarse grained procedure starting from probability distribution functions at the kinetic level [75, 76]. This makes LBM very successful in simulating the physics of fluids over a very broad range of scales. A further advantage of using LBM for multicomponent systems is a diffuse interface model called the Shan-Chen multicomponent model (SCMC) [77, 78], which is able to simulate the two-way coupling between the fluids, the droplet and the solvent. The nature of the SCMC model in the LBM framework made it possible to accommodate complex dynamics on the microscopic level, such as non-ideal effects [79], coupling with polymer micro-mechanics [80] and thermal fluctuations [81, 82]. This LBM multicomponent scheme has also been used widely for the modelling of breakup behaviour in laminar flows [12, 55, 83–90]. In this thesis we will study the effect of generic time-dependency on droplet dynamics and breakup in laminar flows and then move on to the study of sub-Kolmogorov droplet dynamics in homoge-

neous and isotropic turbulence (HIT). We find that breakup in confined and oscillatory shear flows is not only dependent on the degree of confinement, but also on the flow start up conditions and the explicit time-dependency of the solvent flow. For all problems treated in this work we use a newly developed LBM boundary flow scheme, and compare the LBM simulation results with the Maffettone-Minale model [16] and with other theoretical predictions, whenever suitable.

1.2. Thesis outline

The thesis is organized according to the following chapters. Chapter 1 concerns the general motivation of the studies of droplets in turbulent and complex flows. Chapter 2 gives a brief introduction to droplet flow models starting from perturbative models in the Stokes limit to phenomenological models, which are valid for generic flow fields. Furthermore, a brief introduction to turbulent flows and the Kolmogorov scales is given. Chapter 3 provides an overview of LBM and in particular SCMC, an extended LBM diffuse interface model. Chapter 4 discusses droplet behaviour in a low amplitude time-dependent shear flow, which is extended in chapter 5 to large amplitude droplet dynamics and breakup in time-dependent flows with and without confinement. Chapter 6 outlines the details of a multiscale LBM algorithm to model sub-Kolmogorov droplet dynamics and chapter 7 compares the breakup predictions of the Maffettone-Minale model [16] with the LBM predictions. In the end, chapter 8 provides an overall conclusion to the thesis and an outlook to further research on the sub-Kolmogorov droplet dynamics in homogeneous isotropic turbulence.

2. Theoretical Background

This chapter provides an introduction to the theoretical background necessary for the proceeding chapters. Firstly, we discuss the general Navier-Stokes and Stokes equations and then introduce models for multicomponent systems in Stokes flow. We also discuss in detail a phenomenological droplet deformation model, the Maffettone Minale [16], due to its adaptability to droplet dynamics in arbitrary flows. In the end, we give a brief overview of the phenomenology of turbulent flows with an emphasis on the energy cascade and the dissipative scales.

2.1. The equations of fluid flows

The governing equation for incompressible fluid flows are the Navier-Stokes equations (NSE):

$$\begin{aligned}\nabla \cdot \mathbf{v} &= 0 \\ \partial_t \mathbf{v} + (\mathbf{v} \cdot \nabla) \mathbf{v} &= -\frac{1}{\rho} \nabla p + \nu \nabla^2 \mathbf{v}\end{aligned}\tag{2.1}$$

The first equation represents the mass conservation of the incompressible fluid, while the second describes the change of the fluid's momentum due to pressure and dissipative forces. $\mathbf{v}(\mathbf{x}, t)$ represents the velocity field of the fluid at location \mathbf{x} and time t , p is the pressure of the flow, ρ the density of the fluid and ν represents the kinematic viscosity. We can define the Reynolds number Re in order to provide an order of magnitude estimate of the ratio of the inertial ($\mathbf{v} \cdot \nabla \mathbf{v}$) and viscous term ($\nu \nabla^2 \mathbf{v}$) in equation (2.1)

$$\text{Re} \equiv \frac{L_c U_c}{\nu}\tag{2.2}$$

with L_c and U_c being a characteristic length and velocity scale of the flow respectively [6]. Using the characteristic length and velocity scales L_c and

U_c in addition to the kinematic viscosity ν we can non-dimensionalise the NSE:

$$\partial_t \tilde{\mathbf{v}} + (\tilde{\mathbf{v}} \cdot \tilde{\nabla}) \tilde{\mathbf{v}} = -\tilde{\nabla} \tilde{p} + \frac{1}{\text{Re}} \tilde{\nabla}^2 \tilde{\mathbf{v}} \quad (2.3)$$

where $\tilde{\cdot}$ denotes that the physical quantity is given in units of L_c , U_c and ν . In the limit of low Reynolds numbers, i.e. $\text{Re} \rightarrow 0$, equation (2.3) reduces to the Stokes equation

$$-\nabla p + \eta \nabla^2 \mathbf{v} = 0 \quad (2.4)$$

where we use the dimensional quantities p and \mathbf{v} again. $\eta = \rho\nu$ is the dynamic viscosity of the flow. Both the non-linear term $\sim \mathbf{v} \cdot \nabla \mathbf{v}$ and the time dependency $\partial_t \mathbf{v}$ of equation (2.3) vanish. Thus, the Stokes equation is a stationary linear differential equation, whose solutions are unique [91]. This is of great importance in order to find analytical solutions to weakly deformed droplets in Stokes flow, as will be explained in the next section.

2.2. Multicomponent flows

We have derived the Stokes equation (2.4) in section 2.1 as a limiting case of the Navier-Stokes equations (2.1) for $\text{Re} \rightarrow 0$. We reformulate equation (2.4) for a two component system, where the subscript d denotes the droplet and the subscript s the solvent component:

$$\begin{aligned} -\nabla p_s + \eta_s \nabla^2 \mathbf{v}_s &= 0 \\ -\nabla p_d + \eta_d \nabla^2 \mathbf{v}_d &= 0 \end{aligned} \quad (2.5)$$

In order to solve (2.5) we employ a perturbation scheme developed by Taylor [19, 20], where we expand the pressure p and the velocity \mathbf{v} up to linear order in the capillary number Ca for both the droplet d and external flow phase s (subscripts are omitted).

$$\begin{aligned} p &= p_{\text{eq}} + \text{Ca} p_T + \mathcal{O}(\text{Ca}^2) \\ \mathbf{v} &= \mathbf{v}_{\text{eq}} + \text{Ca} \mathbf{v}_T + \mathcal{O}(\text{Ca}^2) \end{aligned} \quad (2.6)$$

with Ca being the capillary number, which serves as a control parameter for the droplet deformation. p_{eq} and \mathbf{v}_{eq} are the pressure and velocity of the undeformed droplet respectively. Ca is given by the ratio of viscous and interfacial forces of the droplet

$$\text{Ca} = \frac{\eta_s R G}{\sigma} \quad (2.7)$$

where G is the shear rate of the solvent flow \mathbf{v}_s , defined via $G \equiv \|\nabla \mathbf{v}_s\|$, R is the radius of the undeformed droplet, η_s the dynamic viscosity of the solvent and σ the surface tension between the two liquids at their interface. The interpretation of the capillary number can be deduced from the Stokes equations (2.5) of the two component system: it represents the ratio of the viscous shear stresses in the flow $\sim \eta_s$ to the surface tension σ . The extent of deformation of the spherical liquid droplet can then be given by

$$D = \frac{L - W}{L + W} \quad (2.8)$$

where L and W are the major and minor axis of the deformed ellipsoidal droplet respectively. With the help of Taylor's theory we may now determine the deformation parameter D_T of the droplet up to first order in the capillary number Ca [19, 20]

$$D_T = \text{Ca} \frac{16 + 19\chi}{16 + 16\chi} \quad (2.9)$$

with

$$\chi = \frac{\eta_d}{\eta_s} \quad (2.10)$$

being the viscosity ratio of the two immiscible fluids, where η_d is the dynamic viscosity of the droplet. Since the Taylor deformation theory considers the droplet to be unbounded, we employ an extension to Taylor's theory [19, 20], the Shapira-Haber model (SH-model) [39, 40], which has a similar line of reasoning as Taylor's theory, but takes the issue of confinement into account. Therefore, in the Shapira-Haber model [39, 40] the deformation parameter is given by

$$D_{SH} = \text{Ca} \frac{16 + 19\chi}{16 + 16\chi} \left[1 + \left(\frac{R}{L_c} \right)^3 \right] C_s \frac{\frac{5}{2}\chi + 1}{\chi + 1} \quad (2.11)$$

where C_s is the so called shape factor [40].

2.3. Maffettone-Minale model (MM)

A more refined model than the one proposed by Taylor [20, 21] is a phenomenological model developed by Maffettone and Minale [16] (to be referenced as MM-model from here on). In the MM-model the droplet is assumed to be always ellipsoidal, so that we can describe it via a second rank tensor M_{ij}

$$M_{ij} = \frac{1}{V_D} \int_{V_D} d^3\mathbf{x} \left(\delta_{ij} - \frac{x_i x_j}{\|\mathbf{x}\|^2} \right) \quad (2.12)$$

which is also referred to as the morphology tensor. V_D denotes the volume of the droplet and \mathbf{x} the distance from the droplet's centre of mass to a point inside V_D . Droplet deformations are characterised via the components of M_{ij} , for example an undeformed droplet has a morphology tensor of $M_{ij} = \delta_{ij}$. It should be noted, that the MM-model is able to model droplet dynamics in generic flows and is not limited to the special case of Stokes flow. The time evolution of M_{ij} due to an external flow field is given by the MM equation:

$$\frac{dM_{ij}}{dt} = \text{Ca} [f_2(S_{ik}M_{kj} + M_{ik}S_{kj}) + \Omega_{ik}M_{kj} - M_{ik}\Omega_{kj}] - f_1 \left(M_{ij} - 3\frac{III_M}{II_M}\delta_{ij} \right) \quad (2.13)$$

where S_{ij} is the strain-rate and Ω_{ij} the rotation-rate tensor of the solvent flow, which are the symmetric and anti-symmetric parts of the velocity gradient tensor $\partial_j v_i$ respectively:

$$S_{ij} = \frac{1}{2}(\partial_j v_i + \partial_i v_j) \quad (2.14)$$

$$\Omega_{ij} = \frac{1}{2}(\partial_j v_i - \partial_i v_j) \quad (2.15)$$

$III_M = \det(M_{ij})$ and $II_M \equiv \frac{1}{2}(M_{kk}^2 - M_{ij}M_{ij})$ are the third and second tensor invariants of M_{ij} . Unlike previous analytical approaches to model droplet deformation in laminar flows [20] the MM-model is not based on a perturbative expansion in the capillary number Ca . Thus we can increase

Ca to relatively large values in our LBM simulations, since we have a robust analytical model to compare it with. However, it should be noted, that the MM-model requires the droplet shape to be ellipsoidal at all times (an ad hoc assumption). Since we want to compare the LBM simulations with the MM-model, we need to make sure that we remain in the linear flow regime and check that our deformed LBM droplet is actually ellipsoidal at all times. We remark that the MM-model has to be modified to account for a confined droplet, as was the case for Taylor's theory, see equation (2.11). This can be achieved by modifying the parameters f_1 and f_2 in equation (2.13) for the confined case. In the unbounded case [16], which we call MM-unbounded, we have

$$\begin{aligned} f_1^{\text{un}}(\chi) &= \frac{40(\chi + 1)}{(3 + 2\chi)(16 + 19\chi)} \\ f_2^{\text{un}}(\chi, \text{Ca}) &= \frac{5}{3 + 2\chi} + \frac{3 \text{Ca}^2}{2 + 6 \text{Ca}^2} \end{aligned} \quad (2.16)$$

and for the confined case [41] which we call MM-confined

$$\begin{aligned} f_1(\chi, \alpha) &= \frac{f_1^{\text{un}}(\chi)}{1 + f_1^c(\chi)C_s \frac{\alpha^3}{8}} \\ f_2(\chi, \text{Ca}, \alpha) &= f_2^{\text{un}}(\chi, \text{Ca}) \left(1 + f_2^c(\chi)C_s \frac{\alpha^3}{8} \right) \end{aligned} \quad (2.17)$$

with

$$\begin{aligned} f_1^c(\chi) &= \frac{44 + 64\chi - 13\chi^2}{2(1 + \chi)(12 + \chi)} \\ f_2^c(\chi) &= \frac{9\chi - 10}{12 + \chi} \end{aligned} \quad (2.18)$$

C_s denotes a form factor, which depends on the degree of confinement [39, 40], and

$$\alpha = \frac{2R}{L_z} \quad (2.19)$$

is the aspect ratio of the droplet length scale, the droplet diameter $2R$, to the scale of the confinement L_z , e.g. the width of a channel, see figure 3.3. The MM-model is originally designed for highly viscous flows, i.e. flows which are close to the Stokes limit (see equation 2.4). Nevertheless, we will see in chapter 7 that the MM-model can be used to study droplet deformation in turbulent flows on the sub-Kolmogorov scale, as the limit of highly viscous flows is still applicable on this scale, see section 2.4.

2.4. Turbulent flows

So far we have only dealt with laminar flows, be it for single or multicomponent systems. However, most flows in nature are not laminar but turbulent. Turbulent flows show specific characteristics which are [5]:

1. **Irregularity:** Turbulent flows are inherently unpredictable, which is most evident by the absence of a general solution to the Navier-Stokes equations in the turbulent regime. Nevertheless, one might think that there might be an effective theory of turbulence even in the absence of a general solution to the NSE. However, this is not the case, as for example the distance $s(t)$ between the trajectories of two tracer particles in a turbulent flow shows chaotic behaviour, because it is highly sensitive to its initial condition. This can be expressed by the Lyapunov exponent [92]:

$$s(t) = s_0 e^{\lambda_L t} \quad (2.20)$$

with $s_0 = s(t = 0)$. $\lambda_L > 0$ is the Lyapunov exponent for the distance $s(t)$ between the two tracer particle trajectories. We see from equation (2.20), that a slight difference in the initial conditions s_0 , leads to an exponential growth of the distance $s(t)$ between the two tracer particle trajectories according to equation (2.20), even if s_0 is infinitesimally small. Due to this sensitivity on initial conditions [92], statistical models are used to investigate turbulent flow properties [8].

2. **Diffusivity of energy:** The transfer of energy from large scales to smaller ones, the so called Richardson cascade, can be seen as the most iconic characteristic of turbulence. The transfer of energy is also

responsible for rapid mixing in case of a multicomponent turbulent flow.

3. **Large Reynolds numbers \mathbf{Re} :** For large \mathbf{Re} the non-linearities of the NSE are dominant, which causes the irregularity of the flow and thus the absence of an analytical solution to the NSE. In this regime only statistical models can adequately describe the flow.
4. **Three dimensional flow:** The transfer of energy from larger to smaller scales, the Richardson cascade, is only possible due to the vortex stretching and elongation in three dimensions ¹.
5. **Dissipative flow:** At the smallest scale of the Richardson cascade, the Kolmogorov scale, the viscous shear stresses dominate and dissipate energy. Every turbulent flow requires an energy input at the largest scales to compensate for the dissipated energy at the Kolmogorov scale.

In general, it is useful to decompose the velocity field $\hat{\mathbf{v}}(\mathbf{x}, t)$ into a mean flow and its fluctuations [5]:

$$\hat{\mathbf{v}}(\mathbf{x}, t) = \mathbf{v}_m(\mathbf{x}) + \mathbf{v}(\mathbf{x}, t) \quad (2.21)$$

where the mean flow field $\mathbf{v}_m(\mathbf{x})$ is the time average of the velocity field

$$\mathbf{v}_m(\mathbf{x}) = \langle \hat{\mathbf{v}}(\mathbf{x}, t) \rangle_t \quad (2.22)$$

with $\langle \dots \rangle_t$ denoting a time average. In this thesis we only deal with homogeneous and isotropic turbulence (HIT), for which the mean flow is $\mathbf{v}_m(\mathbf{x}) = 0$ and we are only left with the velocity fluctuations $\mathbf{v}(\mathbf{x}, t)$, which we shall also call the velocity field from here on. Homogeneous states that the flow is “statistically” invariant under spatial translations of

$$\mathbf{v}(\mathbf{x}, t) \mapsto \mathbf{v}(\mathbf{x} + \mathbf{a}, t) \quad (2.23)$$

with $\mathbf{a} \in \mathbb{R}^3$ being an arbitrary change in position [6]. Analogously, isotropic means that the flow is “statistically” invariant under arbitrary rotations of

¹It should be noted, that a cascade exists in 2D turbulence as well. However energy is transferred from the smallest to largest scales, so that the 2D turbulence cascade is often called an inverse cascade [6, 8].

$$\mathbf{v}(\mathbf{x}, t) \mapsto A \cdot \mathbf{v}(\mathbf{x}, t) \tag{2.24}$$

with $A \in SO(\mathbb{R}^3)$, where $SO(\mathbb{R}^3)$ denotes the special orthogonal transformation group in \mathbb{R}^3 [6]. Therefore, the HIT turbulent flow possesses both translational and rotational symmetry. These symmetries are of great importance in order to discuss the phenomenology of turbulence. There are two main phenomena of turbulence, which are central to this work: for one the Richardson cascade or turbulence cascade is the underlying mechanism of energy transfer in a turbulent flow and ultimately responsible for different flow behaviour on different length scales. Secondly, we will discuss the importance of the dissipative scales, the Kolmogorov microscales and even smaller scales, the sub-Kolmogorov scales.

2.4.1. The Richardson energy cascade

We have mentioned briefly that turbulent flows are dissipative. Yet, in many examples of turbulence structures appear to be stable [5, 6, 8]. How can this be the case for a dissipative flow? In 1922 Louis Fry Richardson gave an explanation to this apparent paradox [6], which is the Richardson or energy cascade: Every fully developed turbulent flow passes its energy from its largest scale of size l_0 , to its smallest scale of size η_K via a cascade mechanism, see figure 2.1. l_0 is taken to be the size of the largest eddies, with an eddy being loosely defined as the largest turbulent structure in the flow. We see from figure 2.1 that the energy is transferred via the energy dissipation ε to different intermediate length scales of sizes $r^n l_0$, where $n \in \mathbb{N}$ and $0 < r < 1$, before reaching the dissipative scale η_K . The region with scales of length $\eta_K < l_n < l_0$, with $l_n = r^n l_0$, is called the inertial subrange. Two key assumptions of the Kolmogorov theory of turbulence (1941) are fulfilled by the cascade mechanism [6]: The inertial subrange is statistically scale invariant, i.e. physical properties are merely rescaled by moving from larger to smaller scales. Secondly, the cascade gives rise to locality of interactions, e.g. if we deal with a length scale $l_n = r^n l_0$, it has received energy from the larger scale $l_{n-1} = r^{n-1} l_0$ and its energy is passed on to a smaller scale of size $l_{n+1} = r^{n+1} l_0$.

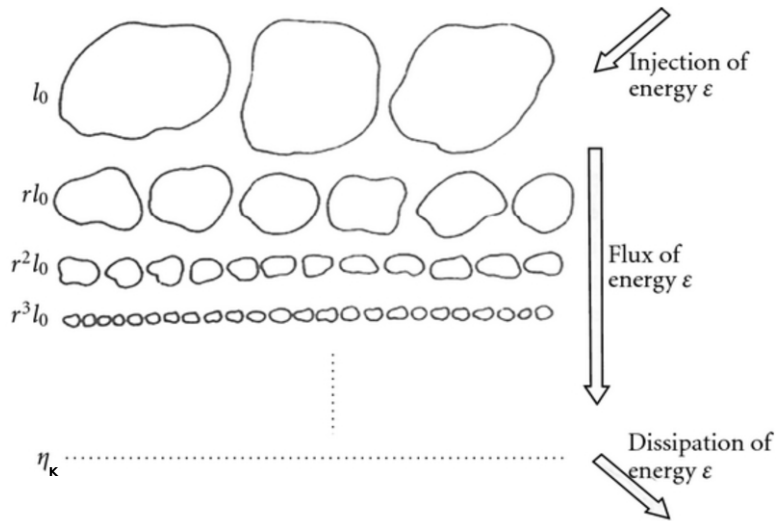


Figure 2.1.: Sketch of the Richardson energy cascade: the energy of the turbulent flow are transferred through a cascade mechanism from the size l_0 of the largest eddies, the integral scale, to the smallest scale η_κ , where energy starts to dissipate. The constraints on the intermediate lengths of size $r^n l_0$, with $n \in \mathbb{N}$, are $0 < r < 1$. The blobs on each length scale level represent the respective eddies of that scale, with l_0 being the length of the largest eddies in the flow. Courtesy of [6].

2.4.2. The Kolmogorov microscales

We have seen that the energy cascade transfers energy from the largest eddies of size l_0 to smaller scales. We now investigate the dissipative scales, the Kolmogorov microscales, at which energy will not only be transferred but starts to dissipate due to the kinematic viscosity ν . In order to investigate the importance of energy dissipation on the microscales, we Fourier transform the NSE (2.1) and investigate its spectral properties. The velocity field can be expressed in spectral space via a set of mode vectors \mathbf{k} .

$$\mathbf{v}(\mathbf{x}, t) = \sum_{\mathbf{k}} \mathbf{v}(\mathbf{k}, t) e^{-i\mathbf{k}\cdot\mathbf{x}} \quad (2.25)$$

and the Fourier transformed velocity field in spectral space is given by

$$\mathbf{v}(\mathbf{k}, t) = \frac{1}{L_{\mathbf{x}}^3} \int_{A_{L_{\mathbf{x}}}} d^3\mathbf{x} \mathbf{v}(\mathbf{x}, t) e^{i\mathbf{k}\cdot\mathbf{x}} \quad (2.26)$$

with $A_{L_{\mathbf{x}}} = L_{\mathbf{x}} \times L_{\mathbf{x}} \times L_{\mathbf{x}}$, where $L_{\mathbf{x}} \in \mathbb{R}$ is the length scale of the finite periodic real space $A_{L_{\mathbf{x}}}$ for the velocity field $\mathbf{v}(\mathbf{x}, t)$ [6]. The Fourier transformed incompressible Navier-Stokes equations (FTNSE) [7] in spectral space are then given by

$$\partial_t v_j(\mathbf{k}, t) + \nu k^2 v_j(\mathbf{k}, t) = -ik_m \left(\delta_{jl} - \frac{k_j k_l}{k^2} \right) \sum_{\mathbf{k}'} v_l(\mathbf{k}', t) v_m(\mathbf{k} - \mathbf{k}', t) \quad (2.27)$$

with δ_{jl} being the Kronecker Delta and $k^2 = k_j k_j$. The incompressibility condition in Fourier space $k_j v_j(\mathbf{k}, t) = 0$ has been implicitly used. After contracting equation (2.27) with the velocity field $v_j(\mathbf{k}, t)$, we obtain an energy balance equation [7]

$$\frac{\partial E(\mathbf{k}, t)}{\partial t} = T(\mathbf{k}, t) - 2\nu k^2 E(\mathbf{k}, t) \quad (2.28)$$

with $E(\mathbf{k}, t) \equiv \frac{1}{2} v_j(\mathbf{k}, t) v_j(\mathbf{k}, t)$ being the kinetic energy of the flow and $T(\mathbf{k}, t)$ an energy transport term. Equation (2.28) represents the transport of energy of the larger scales to smaller scales according to the procedure of the Richardson cascade, until energy dissipates on the Kolmogorov scale and sub-Kolmogorov scale, where the kinematic viscosity ν dominates. Thus, for scales in the inertial subrange, i.e. $k \ll \frac{1}{\eta_K}$, only the transport of energy is

relevant and the dissipative term in equation (2.28) can be neglected. If we sum over all k modes, thus averaging over all length scales, equation (2.28) reads

$$\left\langle \frac{d\bar{E}}{dt} \right\rangle_t = -\varepsilon \quad (2.29)$$

where

$$\bar{E} \equiv \sum_{\mathbf{k}} E(\mathbf{k}, t) = \frac{1}{2} \sum_{\mathbf{k}} v_j(\mathbf{k}, t) v_j(\mathbf{k}, t) \quad (2.30)$$

is the mean energy of the flow per unit mass and

$$\varepsilon \equiv 2\nu \left\langle \sum_{\mathbf{k}} k^2 E(\mathbf{k}, t) \right\rangle_t \quad (2.31)$$

is the mean energy dissipation of the flow per unit mass [6]. The transport function vanishes $\sum_{\mathbf{k}} T(\mathbf{k}, t) = 0$, because the energy is only transported via the energy cascade. We can now define the dissipative scale in turbulent flows, the Kolmogorov scale: The energy input is given by the energy dissipation ε according to equation (2.29). Since we are now in the dissipative region in terms of the Richardson cascade, the transferred energy from larger scales dissipates according to the kinematic viscosity ν . Consequently, we can define a length η_K , time t_η and velocity scale u_η through dimensional analysis

$$\begin{aligned} \eta_K &= \left(\frac{\nu^3}{\varepsilon} \right)^{\frac{1}{4}} \\ t_\eta &= \sqrt{\frac{\nu}{\varepsilon}} \\ u_\eta &= (\nu\varepsilon)^{\frac{1}{4}} \end{aligned} \quad (2.32)$$

which are the Kolmogorov microscales. An alternative definition of the dissipative scale, is the local Reynolds number of the Kolmogorov scale

$$\text{Re}_\eta \equiv \frac{\eta_K u_\eta}{\nu} = 1 \quad (2.33)$$

2. Theoretical Background

At this point we should also consider the Taylor Reynolds number [6]

$$\text{Re}_\lambda = \frac{\bar{E}}{\nu} \sqrt{\frac{10}{3\Omega_E}} \quad (2.34)$$

with

$$\Omega_E \equiv \frac{1}{2L_x^3} \int_{A_{L_x}} d^3\mathbf{x} \, \boldsymbol{\omega}(\mathbf{x}, t) \cdot \boldsymbol{\omega}(\mathbf{x}, t) \quad (2.35)$$

being the mean enstrophy per unit mass, where

$$\boldsymbol{\omega}(\mathbf{x}, t) = \nabla \times \mathbf{v}(\mathbf{x}, t) \quad (2.36)$$

is the vorticity of the flow. Enstrophy can be seen as a measure of vortices and rotation in a turbulent flow [8]. Since Re_λ is only defined via global flow quantities and not specific length or velocity scales, it is an appropriate measure for the degree of turbulence of a flow. Furthermore, it has to be stressed that the Kolmogorov microscale phenomenology still holds true for length scales $l < \eta_K$, where ε acts as an energy input from larger scales and ν is responsible for its dissipation. In this work we deal with sub-Kolmogorov length scales for droplet dynamics, whose radii R fulfil $R \ll \eta_K$, for which the local Reynolds number $\text{Re} < 1$.

3. The Lattice Boltzmann Method (LBM)

The equations for incompressible fluid flows, the Navier-Stokes equations (2.1), are continuum equations, i.e. they contain continuous functions, the scalar density $\rho(\mathbf{x}, t)$ and pressure $p(\mathbf{x}, t)$ fields and the fluid velocity field $\mathbf{v}(\mathbf{x}, t)$. In this chapter we will show that a discrete microscopic description, the Lattice Boltzmann equation (LBE), can be used to derive the equations of fluid flows (equation (2.1)) in the hydrodynamic limit. We will also outline the general algorithmic structure of the Lattice Boltzmann methods (LBM). Furthermore, we will introduce the Shan-Chen multicomponent model (SCMC) [77, 78], which is an LBM based diffuse interface model. Moreover, we report validation results for the SCMC model and introduce an LBM ghost node boundary scheme to be used in all simulations performed in chapters 4, 5, 6 and 7.

3.1. The Boltzmann and Lattice Boltzmann equation

The Boltzmann equation and Lattice Boltzmann equation can be derived from Hamiltonian classical mechanics. Let us consider a set of N classical particles $\{\mathbf{q}_j, \mathbf{p}_j\}_N$ with generalised coordinates \mathbf{q}_j and generalised momenta \mathbf{p}_j , which obey the symplectic Hamilton equations

$$\begin{aligned}\dot{\mathbf{q}}_j &= \frac{\partial H_N}{\partial \mathbf{p}_j} \\ \dot{\mathbf{p}}_j &= -\frac{\partial H_N}{\partial \mathbf{q}_j}\end{aligned}\tag{3.1}$$

where $H_N \equiv H(\{\mathbf{q}_j, \mathbf{p}_j\}_N)$ is the (time-independent) Hamilton function of the system of classical particles [93]. Thus, we can formulate a Liouville equation by introducing a particle density function $g_N(\{\mathbf{q}_j, \mathbf{p}_j\}_N, t)$ [93]:

$$\frac{\partial g_N}{\partial t} = -\sum_{j=1}^N \left(\frac{\partial g_N}{\partial \mathbf{p}_j} \dot{\mathbf{p}}_j + \frac{\partial g_N}{\partial \mathbf{q}_j} \dot{\mathbf{q}}_j \right) \quad (3.2)$$

Although the Liouville equation provides a time evolution for the particle distribution function g_N , we would like to have a simpler expression, ideally involving a single particle distribution function $g(\mathbf{q}_j, \mathbf{p}_j, t)$ for particle j . In order to derive a simpler equation we need to employ three approximations given in [93]:

1. only pairwise collisions of particles are considered (e.g. particle i with particle j)
2. the pre-collision velocities of colliding particles are uncorrelated
3. particle interactions are not influenced by external forces

Now we can derive an evolution equation for the single particle distribution function $g(\mathbf{x}, \mathbf{v}, t)$:

$$\frac{\partial g(\mathbf{x}, \mathbf{v}, t)}{\partial t} + \mathbf{v} \cdot \nabla g(\mathbf{x}, \mathbf{v}, t) = \Omega(g(\mathbf{x}, \mathbf{v}, t), g^{\text{eq}}(\mathbf{x}, \mathbf{v}, t)) \quad (3.3)$$

which is the Boltzmann equation without external forces, where $\mathbf{x} = \mathbf{q}_j$ and $\mathbf{v} = \frac{\mathbf{p}_j}{m}$ are the position and velocity of the single particle j respectively. m is the particle mass and $\Omega(g(\mathbf{x}, \mathbf{v}, t))$ is the collision operator, which depends on the single particle distribution function $g(\mathbf{x}, \mathbf{v}, t)$ and an equilibrium distribution function $g^{\text{eq}}(\mathbf{x}, \mathbf{v}, t)$. The equilibrium distribution function can be derived by looking at the stationary state of equation (3.3) $\Omega(g(\mathbf{x}, \mathbf{v}, t), g^{\text{eq}}(\mathbf{x}, \mathbf{v}, t)) = 0$ and we find

$$g^{\text{eq}}(\mathbf{x}, \mathbf{v}, t) = n \left(\frac{m}{2\pi k_B T} \right)^{\frac{3}{2}} e^{-\frac{m}{2\pi k_B T} (\mathbf{v} - \bar{\mathbf{v}})^2} \quad (3.4)$$

which is the Maxwell Boltzmann distribution function with velocity field \mathbf{v} , temperature $T(\mathbf{x})$, total particle density $n(\mathbf{x})$ and mean velocity $\bar{\mathbf{v}}(\mathbf{x})$, where k_B is the Boltzmann constant [93]. We can now discretise the Boltzmann equation in both space and time on a lattice and obtain [94, 95]:

$$\underbrace{g_i(\mathbf{x} + \mathbf{c}_i \Delta t, t + \Delta t) - g_i(\mathbf{x}, t)}_{\text{Streaming}} = \underbrace{\Omega_i(\{g_i(\mathbf{x}, t)\})}_{\text{Collision}} \quad (3.5)$$

which is the Lattice Boltzmann equation (LBE). \mathbf{x} are the discrete lattice positions and Δt is the discretised time step. The index i now denotes a lattice stencil for each lattice position \mathbf{x} with a set of discrete lattice velocities (or lattice vectors) \mathbf{c}_i , for which $i \in \{0 \dots N\}$ with N being the number of non-zero lattice vectors and $\mathbf{c}_{i=0} = 0$ indicating the lattice node at position \mathbf{x} . An example of such a lattice stencil is shown in figure 3.1 for a D3Q19 lattice (3D and 19 lattice velocities \mathbf{c}_i). We remark that the discretised single particle distribution functions $g_i(\mathbf{x}, t)$ are often called lattice populations or simply populations.

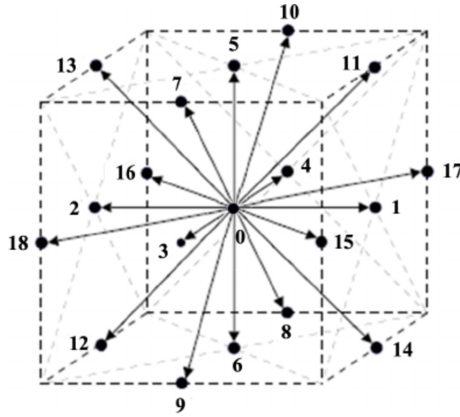


Figure 3.1.: Sketch of a 3DQ19 lattice with the discrete lattice velocities \mathbf{c}_i given as lattice directions.

The LBM equivalent of the equilibrium distribution function in equation (3.4) is given by [93, 94]:

$$g_i^{\text{eq}}(\rho, \mathbf{v}) = w_i \rho \left(1 + 3(\mathbf{c}_i \cdot \mathbf{v}) + \frac{9}{2}(\mathbf{c}_i \cdot \mathbf{v})^2 - \frac{3}{2}\mathbf{v}^2 \right) \quad (3.6)$$

with $\rho(\mathbf{x}, t)$ being the density of the system, \mathbf{v} being the equilibrium velocity and w_i lattice weights [94]. The LBM equilibrium distribution function g_i^{eq} is essentially a velocity truncated discretised Maxwell Boltzmann distribution function, see equation (3.4). The velocity truncation is especially necessary in the case of low compressibility, since in this region the Mach number

$$Ma = \frac{v}{c_s} \quad (3.7)$$

3. The Lattice Boltzmann Method (LBM)

should obey the limit $Ma \ll 1$. $v = \|\mathbf{v}(\mathbf{x}, t)\|_\infty$, with $\|\dots\|_\infty$ being the maximum norm, and c_s denotes the speed of sound in lattice Boltzmann units (lbu), which for a uniform lattice is $c_s = \frac{1}{\sqrt{3}}$. We have indicated two qualitatively different steps in equation (3.5), collision and streaming. The collision step merely evaluates the collision operator function $\Omega_i(\{g_i(\mathbf{x}, t)\})$. The streaming step updates the values of the populations $g_i(\mathbf{x} + \mathbf{c}_i \Delta t, t + \Delta t)$ at the neighbouring lattice nodes of node \mathbf{x} with the post collisional populations $g'_i(\mathbf{x}, t + \Delta t)$. This provides us with the essential LBM algorithm:

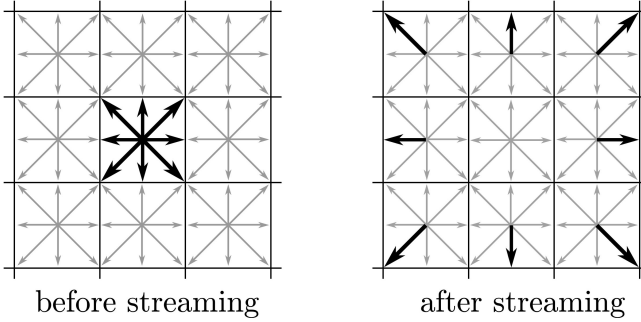


Figure 3.2.: Sketch of the streaming step: The values of the populations $g_i(\mathbf{x} + \mathbf{c}_i \Delta t, t + \Delta t)$ are updated with the post collisional population values $g'_i(\mathbf{x}, t + \Delta t)$ at the lattice node \mathbf{x} .

1. perform the collision step via the collision operator $\Omega_i(\{g_i(\mathbf{x}, t)\})$
2. carry out the streaming step
3. evaluate and update the macroscopic quantities $\rho(\mathbf{x}, t)$ and $\mathbf{v}(\mathbf{x}, t)$
4. repeat step 1

The density $\rho(\mathbf{x}, t)$ and velocity field $\mathbf{v}(\mathbf{x}, t)$ can be obtained via the LBM populations:

$$\begin{aligned} \rho(\mathbf{x}, t) &= \sum_i g_i(\mathbf{x}, t) \\ \mathbf{v}(\mathbf{x}, t) &= \frac{1}{\rho(\mathbf{x}, t)} \sum_i g_i(\mathbf{x}, t) \mathbf{c}_i \end{aligned} \quad (3.8)$$

$\Omega_i(\{g_i(\mathbf{x}, t)\})$ is now a generic discretised collision operator depending on the whole set of lattice distribution functions $\{g_i(\mathbf{x}, t)\}$ at lattice position \mathbf{x} and time t . It can be shown [95] that any generic LBM collision operator only depends linearly on the local populations $g_i(\mathbf{x}, t)$ and the equilibrium distribution functions $g_i^{\text{eq}}(\rho, \mathbf{v})$:

$$\Omega_i(\{g_i(\mathbf{x}, t)\}) = \mathcal{L}_{ij}(g_j(\mathbf{x}, t) - g_j^{\text{eq}}(\mathbf{x}, t)) = \mathcal{L}_{ij}g_j^{\text{neq}}(\mathbf{x}, t) \quad (3.9)$$

where $g_i^{\text{neq}}(\mathbf{x}, t) = g_i(\mathbf{x}, t) - g_i^{\text{eq}}(\mathbf{x}, t)$ is the non-equilibrium part of the distribution function g_i and L_{ij} the distribution function independent collision operator. The simplest collision operator is the BGK operator, for which L_{ij} is diagonal and equal to a constant:

$$\mathcal{L}_{ii} = \frac{1}{\tau} \quad (3.10)$$

with τ being called the relaxation time of the system. According to equation (3.9), τ indicates the speed at which the collision step takes place, i.e. at which rate the populations g_i approach the equilibrium populations $g_i^{\text{eq}}(\mathbf{x}, t)$ or equivalently at which rate the non-equilibrium parts of the populations $g_i^{\text{neq}}(\mathbf{x}, t) \rightarrow 0$. Consequently the BGK operator models the collision with a single relaxation time scale. For further numerical stability [96] we can use the multi relaxation time scheme (MRT) [97]. In MRT we perform a basis transformation into a mode space with a set of orthonormal basis vectors $\{e_{ij}\}_i$ and corresponding modes $m_i(\mathbf{x}, t)$:

$$m_i(\mathbf{x}, t) = \sum_j e_{ij}g_j(\mathbf{x}, t) \quad (3.11)$$

The collision step in mode space with relaxation parameters λ_i is then given via

$$m_i^{*\text{neq}}(\mathbf{x}, t) = (1 + \lambda_i)m_i^{\text{neq}}(\mathbf{x}, t) \quad (3.12)$$

where $m_i^{*\text{neq}}(\mathbf{x}, t)$ is the post-collision non-equilibrium mode, and $m_i^{\text{neq}}(\mathbf{x}, t)$ the pre-collision non-equilibrium mode. Important conserved modes are

- $m_0(\mathbf{x}, t) = \rho(\mathbf{x}, t)$
- $m_1(\mathbf{x}, t) = j_x(\mathbf{x}, t)\Delta t$
- $m_2(\mathbf{x}, t) = j_y(\mathbf{x}, t)\Delta t$

- $m_3(\mathbf{x}, t) = j_z(\mathbf{x}, t)\Delta t$

which represent the mass $\rho(\mathbf{x}, t)$ and momentum density $\mathbf{j}(\mathbf{x}, t) = \rho(\mathbf{x}, t)\mathbf{v}(\mathbf{x}, t)$ respectively. For MRT the collision operator contains several relaxation times linked to its relaxation modes (depending on the lattice stencil) [97]. In case of a fluid flow, one relaxation time τ is directly linked to the kinematic viscosity ν in the system (incidentally it is equivalent to the one in the BGK collision model)

$$\nu = c_s^2 \left(\tau - \frac{1}{2} \right) = \frac{1}{3} \left(\tau - \frac{1}{2} \right) \quad (3.13)$$

which is one of the primary links between the LBM scheme and hydrodynamics [75, 76]. In this work we use the MRT collision model for all simulations.

3.2. The Chapman-Enskog Expansion (CEE)

So far we have only dealt with LBM as a solver for the dynamics of particles, but have not seen their applicability to the continuum equations of fluid flows (equations (2.1)). The hydrodynamical manifold, i.e. the Navier-Stokes equations (NSE), can be recovered via the Chapman-Enskog expansion, a perturbation theory in the Knudsen number Kn , which is defined as

$$\epsilon = Kn = \frac{l_m}{L} \quad (3.14)$$

where l_m is the molecular mean free path length and L a macroscopic length scale. The Knudsen number Kn can therefore be seen as an indicator for the physical density ρ of a system, e.g. for a fixed macroscopic length scale L the Knudsen number Kn is directly proportional to the mean free path l_m , which decreases with increasing density. Now we define three relevant time scales and one length scale for our perturbative expansion in Kn . We will be following the outline given in [95].

$$\begin{aligned} \Delta t &\sim \mathcal{O}(1) \text{ lattice time scale} \\ t_1 = \epsilon \Delta t &\sim \mathcal{O}(\epsilon) \text{ convective time scale} \\ t_2 = \epsilon^2 \Delta t &\sim \mathcal{O}(\epsilon^2) \text{ diffusive time scale} \\ \mathbf{x}_1 = \epsilon \mathbf{x} &\sim \mathcal{O}(\epsilon) \text{ coarse grained position vector} \end{aligned} \quad (3.15)$$

With these scales defined we obtain a series expansion of equation (3.5) in orders of ϵ

$$\begin{aligned}
 \mathcal{O}(1) : \Omega_i^{(0)} &= 0 \\
 \mathcal{O}(\epsilon) : (\partial_{t_1} + \mathbf{c}_i \cdot \nabla_{\mathbf{x}_1}) g_i^{(0)} &= \frac{\Omega_i^{(1)}}{\Delta t} \\
 \mathcal{O}(\epsilon^2) : [\partial_{t_2} + (\partial_{t_1} + \mathbf{c}_i \cdot \nabla_{\mathbf{x}_1})^2] g_i^{(0)} + \frac{\Delta t}{2} (\partial_{t_1} + \mathbf{c}_i \cdot \nabla_{\mathbf{x}_1}) g_i^{(1)} &= \frac{\Omega_i^{(2)}}{\Delta t}
 \end{aligned} \tag{3.16}$$

with the indices (0), (1) and (2) denoting contributions of the order of $\mathcal{O}(1)$, $\mathcal{O}(\epsilon)$ and $\mathcal{O}(\epsilon^2)$ respectively. Thus, for the expansion of the LBE until $\mathcal{O}(\epsilon^2)$ we obtain

$$\begin{aligned}
 \partial_t \rho + \nabla \cdot (\rho \mathbf{v}) &= 0 \\
 \partial_t (\rho \mathbf{v}) + \nabla \cdot (\rho \mathbf{v} \mathbf{v}) &= -\nabla p + \nabla \cdot \sigma_S
 \end{aligned} \tag{3.17}$$

with $\nabla_{\mathbf{x}_1}$ representing ∇ in respect to \mathbf{x}_1 , the Euler stress $S_{ij}^{\text{eq}} = p\delta_{ij} + \rho v_i v_j$ and the non-equilibrium stress tensor $S^{*\text{neq}} + S^{\text{neq}} = -2\sigma^{(S)}$, where $\sigma_{ij}^{(S)} = \eta_{ijkl} \frac{\partial v_k}{\partial r_l}$ is the viscous stress tensor and η_{ijkl} the dynamic viscosity tensor. The pressure $p(\mathbf{x}, t)$ is given via an LBM equation of state

$$p(\mathbf{x}, t) = \rho(\mathbf{x}, t) c_s^2 \tag{3.18}$$

which can be seen as a pressure-density equivalency in the LBM framework. Equations (3.17) are the compressible Navier-Stokes equations (2.1) with a generic dynamic viscosity tensor, which reduce to the incompressible Navier-Stokes equations in the incompressible ($\rho(\mathbf{x}, t) = \rho = \text{constant}$) and the Newtonian ($\eta = \rho\nu = \text{constant}$) limits, where the dynamic viscosity η is a scalar quantity.

3.3. Shan-Chen multicomponent model

The classical Lattice Boltzmann Model (LBM) for single phase flows needs to be modified to account for a system containing two immiscible fluids, in particular the fluid-fluid interface between them. One of the most used

scheme to model the fluid-fluid interface is the Shan-Chen Multi-Component model (SCMC) [77, 78]. For two (or more) immiscible fluids we need to distinguish between the type of fluid component at hand, thus we get for the mass and momentum densities:

$$\begin{aligned}\rho(\mathbf{x}, t) &= \sum_{\sigma} \sum_i g_i^{\sigma}(\mathbf{x}, t) \\ \rho(\mathbf{x}, t)\mathbf{v}(\mathbf{x}, t) &= \sum_{\sigma} \sum_i g_i^{\sigma}(\mathbf{x}, t)\mathbf{c}_i\end{aligned}\quad (3.19)$$

where $g_i^{\sigma}(\mathbf{x}, t)$ denotes the populations in the LBM model for the fluid component σ and \mathbf{c}_i are the lattice velocities. The interaction at the respective fluid-fluid interface [98, 99] is given by:

$$\mathbf{F}^{\sigma}(\mathbf{x}) = -\psi_{\sigma}(\mathbf{x}) \sum_{\sigma' \neq \sigma} \sum_{i=1}^N \mathcal{G}_{\sigma, \sigma'} w_i \psi_{\sigma'}(\mathbf{x} + \mathbf{c}_i) \mathbf{c}_i \quad (3.20)$$

where $\psi_{\sigma}(\mathbf{x})$ is a local pseudo-potential which may be defined via the phase densities $\rho_{\sigma}(\mathbf{x}, t)$. $\mathcal{G}_{\sigma, \sigma'}$ is a coupling constant for the two phases σ and σ' at position \mathbf{x} and w_i are the lattice isotropy weights. One should note that the stencil for the SCMC pseudo-potential interaction does not necessarily have to coincide with the stencil populations for the LBM streaming, but could be a different lattice stencil, given that the interaction force $\mathbf{F}^{\sigma}(\mathbf{x})$ remains isotropic.

3.4. Validation tests for confined droplets

After having introduced the LBM as a fluid solver for both single phase and multicomponent flows, we give a LBM multicomponent flow example. We consider the static deformation of a 2D droplet centred in the middle of the simulation domain, with periodic boundary conditions [94] in the x- and bounce-back (wall) boundary conditions [94] in the z-direction, see figure 3.3. The aim of the LBM simulations is to determine the deformation of the 2D droplet as a function of the capillary number Ca under the influence of an external shear flow u_x at the boundary walls. u_x at the boundaries is a free parameter in our simulations and ranges from the static case $u_x = 0$ to $u_x = 0.05$ (lbu), which enables us to tune the capillary number Ca . In order

to determine the surface tension σ we carry out a Laplace measurement in the static case, before starting the dynamic simulations involving u_x . The Laplace pressure in 2D is:

$$\Delta p = \frac{\sigma}{R} \quad (3.21)$$

with $\Delta p \equiv |p_{\text{in}} - p_{\text{out}}|$ being the difference between the internal pressure (inner pressure) of the droplet and the external pressure of the surrounding fluid (outer pressure). The Laplace measurement is visualised in figure 3.4 from which we can determine the surface tension σ due to (3.21). For the dynamic simulations we use a constant shear flow u_x at the boundary walls in the z -direction, see figure 3.3. In order to measure the deformation parameter D , we calculate the moment of inertia tensor I_{ij} of the droplet at first:

$$I_{ij}(t) = \int_{V_D} d^3\mathbf{x} \rho(\mathbf{x}, t) (\delta_{ij} \|\mathbf{x}\|^2 - x_i x_j) \quad (3.22)$$

where V_D is the volume of the droplet [92]. Then we determine the major L and minor axis W of the deformed droplet via the relation

$$\begin{aligned} L &\sim \frac{1}{\sqrt{\mu_2}} \\ W &\sim \frac{1}{\sqrt{\mu_1}} \end{aligned} \quad (3.23)$$

with $\mu_1 \geq \mu_2 > 0$, where μ_1 and μ_2 are the eigenvalues of I_{ij} . This yields the degree of deformation D defined in (2.8). Furthermore, for a comparison of our simulations with the Shapira-Haber model [39, 40] we need the shape factor, which is $Cs \approx 5.6996$ for a centred droplet. We can see in figure 3.5 that our LBM simulations are in relatively good agreement with the Shapira-Haber model in the case of low capillary numbers Ca . The simulation results deviate significantly from the theoretical model, however, if we consider a range of larger Ca values. This is to be expected, since the Shapira-Haber model considers only the linear term in Ca of a perturbation series of p and \mathbf{v} , see equations (2.6) ¹.

¹The disagreement between LBM and the SH-model vanishes, if we reduce the inertia, i.e. lower Reynolds numbers Re , as will be shown in chapter 4

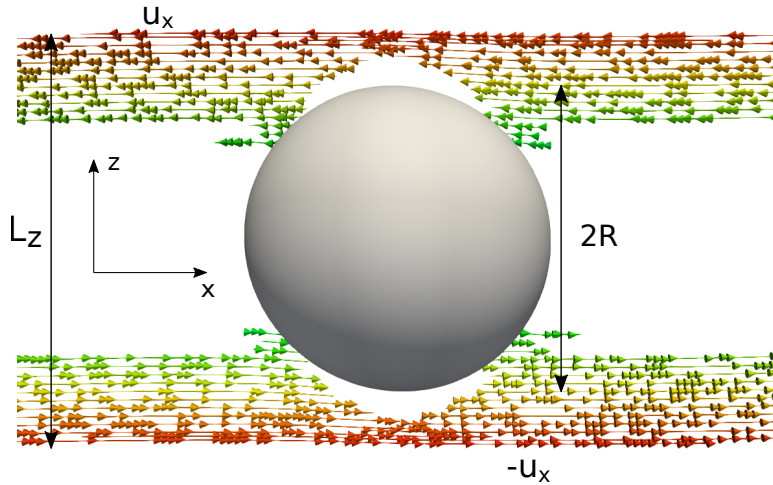


Figure 3.3.: Set up for the Laplace test and static droplet deformation of a 2D confined droplet in a shear flow. The droplet radius is given by R and the wall separation length by L_z . For the Laplace test the wall velocity $u_x = 0$ and $u_x \neq 0$ in the case of static deformation. The droplet is visualised in 3D for simplicity, even though the simulations were carried out in 2D.

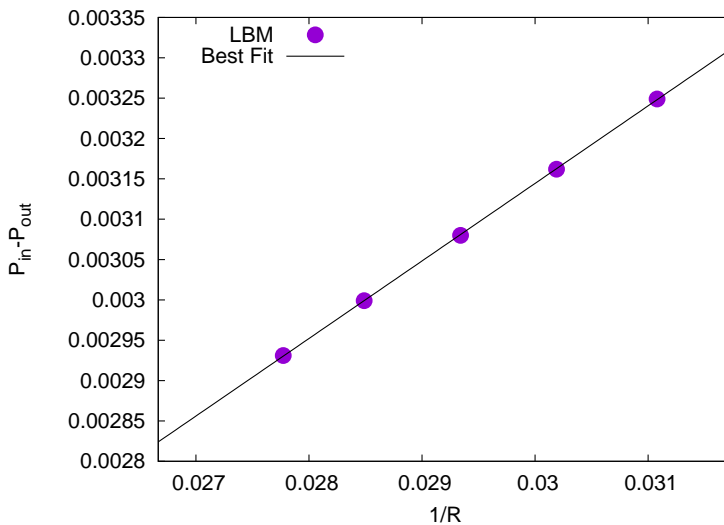


Figure 3.4.: Laplace test Δp against the interfacial curvature $\frac{1}{R}$. The surface tension σ is given via the slope of the best fit through the LBM data points.

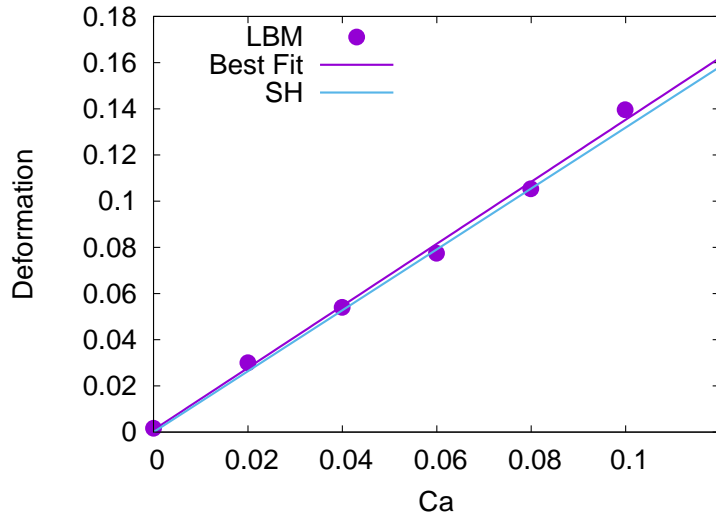


Figure 3.5.: Static droplet deformation test against the Shapira-Haber model (SH-model) [40] for a low Ca range. The best fit of the data points and the SH-model predictions agree well in this capillary number range.

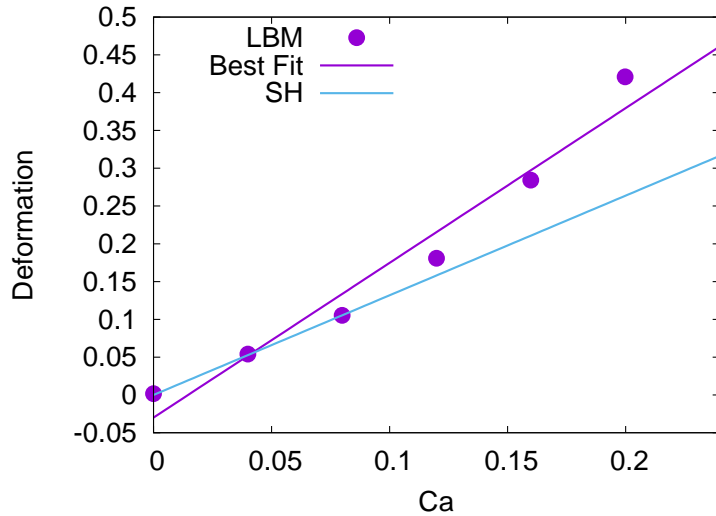


Figure 3.6.: Static droplet deformation test against the SH-model [40] for a high Ca range. The LBM data points do not follow a linear relationship and thus LBM disagrees with the SH-model in this capillary number range. This disagreement is due to inertia and vanishes for lower Reynolds numbers Re for the Ca range used here, see chapter 4.

3.5. A ghost node boundary flow scheme

In order to effectively simulate a time-dependent flow, we use specially modified boundary conditions. We make use of the ghost populations (or halos) to store the local LBM equilibrium population distributions given by the systems boundary values for the density $\rho_b(\mathbf{x}, t)$ and velocity $\mathbf{u}(\mathbf{x}, t)$ of the outer fluid (for simplicity we will treat a single component fluid).

$$g_i^{\text{eq}}(\mathbf{x}, t) = \rho_b(\mathbf{x}, t)w_i \left(1 + 3\mathbf{c}_i \cdot \mathbf{u} + \frac{9}{2}(\mathbf{c}_i \cdot \mathbf{u})^2 - \frac{3}{2}\mathbf{u}^2 \right) \quad (3.24)$$

with $\{w_i\}$ being the lattice weights for the set of lattice vectors $\{\mathbf{c}_i\}$. Thus the ghost distributions will update the boundary nodes during the LBM streaming step and let the system know about the previously chosen boundary conditions (see figure 3.7). Since the ghost nodes only stream into the system and not out of it, we have to correct the local population mass densities in order to keep the system mass conserving [11, 100–102], in the case of a confined system with a no slip boundary wall. Thus, the boundary scheme is equivalent to a mid-bounce-back rule [93, 94], if confinement is present. However, if we deal with an unconfined system, which we would have in the case of a sub-Kolmogorov droplet in a turbulent flow, mass conservation does not have to be strictly enforced and we use an anti evaporation scheme [11] to keep the mass of the droplet constant. This is a suitable procedure, since we are only interested in the dynamics of the droplet and not that of the solvent. In this way we keep a constant density ratio and keep the droplet's mass fixed, even though the mass of the solvent may vary.

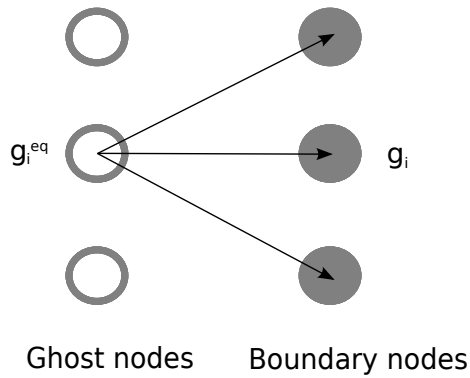


Figure 3.7.: Sketch of the streaming step from ghost to boundary nodes. The ghost nodes are initialised via the local equilibrium distributions g_i^{eq} . By initialising the ghost nodes with a given equilibrium density $\rho(\mathbf{x}, t)$ and equilibrium velocity field $\mathbf{u}(\mathbf{x}, t)$, we can effectively set the boundary conditions of the system.

4. Droplet in a time-dependent flow: LBM and MM comparison

This chapter ¹ deals with the ghost node boundary flow method outlined in chapter 3. The method is first tested for a simple single phase problem. An oscillatory shear flow in an infinitely long channel. Then we use this set up to investigate droplet deformation in confined systems with both stationary and time-dependent flows. The results of the LBM simulations are compared to the ones obtained via numerical and perturbative solutions to the MM-model [16, 41].

4.1. Introduction

The multiscale problem of interest in this chapter is the fluid dynamics of an emulsion, i.e. a collection of small deformable droplets dispersed in a solvent immiscible fluid: droplets can deform under the action of an imposed flow and can interact with neighboring droplets, they provide a back-reaction on the solvent component and ultimately determine the complex flowing properties of the emulsion at large scales. Far from being only an interesting multiscale physical problem, it also finds a variety of applications in industrial and engineering processes [1]. In order to describe these complex multicomponent flows, we reduce the system to the dynamics and deformation of a single droplet under the influence of an externally imposed flow. The literature on single droplet deformation is vast, especially when dealing with laminar flows: following the pioneering work by Taylor [20], the deformation properties of a droplet have been extensively studied and reviewed [25, 103]. Existing studies address the effects introduced by the nature of the flow [104–107], the effects of confinement [40, 41], as well as

¹Published as: Milan, F., Sbragaglia, M., Biferale, L., Toschi, F., *Lattice Boltzmann simulations of droplet dynamics in time-dependent flows*, Eur. Phys. J. E (2018) 41: 6. <https://doi.org/10.1140/epje/i2018-11613-0>

the effects introduced by the complex non-Newtonian nature of the bulk fluids [87, 108, 109]. Exact analytical approaches are typically limited to “small” deformation assumptions, i.e. perturbative results. Extensions to time-dependent laminar flows have also been carried out [21]. From the theoretical side, a popular model has been developed by Minale & Maffettone [16], the MM-model, which assumes the droplet to be an ellipsoid at all times [110, 111], and is constructed to recover the perturbative results on droplet deformation at small Ca (e.g. Taylor’s result [20]) in the presence of a steady flow. The MM-model has the key advantages to allow for time dynamics and also to extend the description of droplet deformation beyond the limits of applicability of perturbation theories [20], hence it has also been used to characterize the critical Ca for which droplet breakup occurs [16]. Following the MM-model, a whole class of “ellipsoidal” models have been introduced with further enrichments to account for a variety of other effects, including viscoelasticity [61, 112–114], confinement [29, 31–34, 87, 88, 115] and matching with more refined perturbative results at small Ca [105, 108, 109, 116]. A detailed review on the topic can be found in [42]. These ellipsoidal models become particularly useful when studying the properties of a single droplet under the influence of turbulent fluctuations [13, 15, 17]. Depending on the characteristic size of the droplet, turbulent fluctuations can provide either inertial distortions [13], when the droplet size is above the characteristic dissipative scale, or laminar distortions [15, 17], for smaller droplets. It has to be noted that analytical models cannot be used to describe the deformation of large droplets accurately and in particular the MM-model fails to capture non-ellipsoidal deformations. Therefore, it is crucial to develop ab initio models, such as multicomponent LBM with appropriate boundary schemes in order to enforce time-dependent fluid deformations. If combined with a Lagrangian history of a turbulent strain matrix, the model allows for a comprehensive characterization of the statistics of droplet shape, size and orientation in a realistic turbulent environment [17]. A key parameter to quantify the reaction of the droplet to the time-dependent signal is the ratio between the droplet relaxation time

$$t_d = \frac{\eta_d R}{\sigma} \quad (4.1)$$

and the fluid time scale

$$t_f = \frac{R}{u_0} \quad (4.2)$$

where u_0 is the maximal shear flow intensity. Depending on the ratio t_d/t_f the droplet is either able to follow the fluid variations ($t_d/t_f \rightarrow 0$), or starts to decouple when $t_d/t_f \approx 1$. This influences its deformation and possibly the alignment with the flow. Furthermore, a turbulent signal has a broad spectrum rather than a single time scale t_f , thus resulting in a multi-chromatic behaviour coupled to the non-linear response of the droplet deformation process. This is an ideal workspace for LBM mesoscopic models to operate: they intrinsically allow for both droplet deformation at the mesoscale, and they can be constructed to reproduce the desired hydrodynamical flow at large scales. Droplet deformation properties have been the subject of various articles [12, 29, 41, 43, 44, 48, 85, 103, 117–119], but these typically contain studies of deformation and orientation in steady state flows [12, 80, 85, 119], or studies of the critical droplet breakup condition [46, 88], with particular emphasis on the comparison between the (diffuse interface) hydrodynamics of LBM and the sharp interface results [12, 87, 88, 119]. Droplet dynamics has also been simulated [25, 105, 108, 109, 111, 120], but the associated quantitative validation has been scarcely detailed in the literature. This chapter aims at filling this gap from the methodological point of view: after revisiting the validation of LBM for steady state flows, we introduce a time dependency to the system and quantitatively compare LBM against the analytical predictions of ellipsoidal models at changing the ratio between the droplet relaxation time t_d and the fluid time scale t_f . The chapter is organized as follows: section 4.2 gives a brief overview on the static droplet deformation of Lattice Boltzmann simulations compared with relevant theoretical models. In section 4.3 the behaviour of a simple oscillatory shear in a 2D LBM channel flow is tested, which will be relevant for section 4.4 where we investigate the response of an isolated droplet to a time-dependent oscillatory channel flow in a 3D LBM model.

4.2. Static droplet deformation

The first step is to test our algorithm in the case of the deformation of a single droplet in a constant shear flow confined in a channel, see figure 4.1. Inertia is characterised by the Reynolds number $\text{Re} = R^2G/\nu$ where, in the

4. Droplet in a time-dependent flow: LBM and MM comparison

case of a simple shear flow, the shear rate is $G = 2u_0/L_z$, with u_0 being the maximum shear at the wall and L_z the channel width. Now we let the droplet evolve in the shear flow and measure its deformation. We consider only set-ups with an aspect ratio $\alpha \equiv 2R/L_z = 0.75$ and keep the viscosity ratio $\chi = 1$ throughout all simulations. According to [121] the droplet will be stable up to a value of $Ca \approx 0.4$ regardless of our choice for the confinement ratio α . A series of LBM runs is shown in figure 4.2 and three different values for the kinematic viscosity ν in lbu (Lattice Boltzmann units). We may see that for the lowest value of ν the deformation D is deviating substantially from the theoretical predictions for a confined droplet, given both by the Shapira-Haber model [29] and the MM-confined model [41].

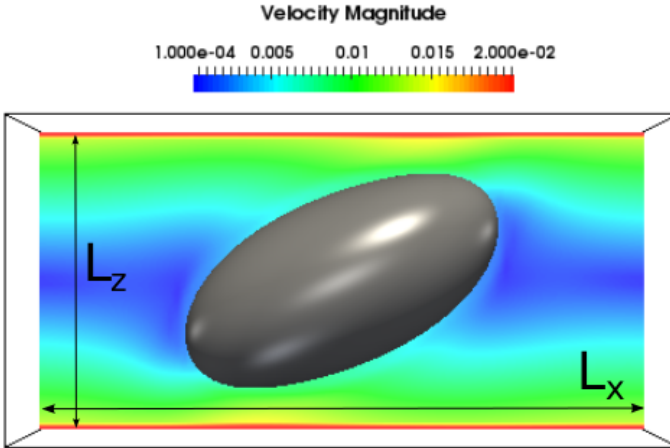


Figure 4.1.: Screenshot of a multicomponent LBM simulation. A droplet is ellipsoidally deformed via an external shear flow, created by the moving channel walls. The relevant system parameters are: the initial droplet radius R , the shear rate G , the channel width L_z and the other lengths of the simulation domain L_x and L_y (not shown). The magnitude of the overall velocity field in lbu is given via a colour gradient.

For the two lower Re values the simulations agree much better with the MM-confined model predictions. Figure 4.2 also shows the static deformations for a higher resolution in the bottom panel where the respective Reynolds number Re lies in the same range as for the plots in the top panel. In this case the droplet deformation of our LBM scheme agrees even better with the theoretical predictions for a confined droplet. Thus we can deduce both: that we need a significantly low Reynolds number and that we

may only compare our simulation results to models which account for the confinement of the droplet. To our knowledge this is the first benchmark of LBM against theoretical predictions for the influence of droplet inertia in static droplet deformation in a system with a significant confinement ratio.

4.3. Probing the parameter space: single component oscillating shear flow

After having benchmarked the static droplet deformation against a variety of theoretical models we investigate the

droplet behaviour under a time-dependent linear shear flow. Before considering explicitly the case of a binary fluid (see section 4.4) we need to determine a suitable range for our LBM parameters. We remark that LBM works well as a “hydrodynamic solver” only if the LBM populations are close to the hydrodynamical manifold. Hence it is crucial to design a set of “working parameters” for which we know that our LBM scheme correctly solves the time-dependent hydrodynamical equations. Specifically, for the case of a time-dependent shear flow, we will compare our LBM scheme against the exact time-dependent solution of an oscillating shear flow [91]. For simplicity we modify the boundary conditions for a 2D channel flow by setting $v_x(0, t) = u_0 \cos(\omega t)$ and $v_x(L_z, t) = 0$, i.e. one side of the channel is oscillating with a shear frequency $\omega_f = \omega/(2\pi)$ and the other one is static (see figure 4.3). Making use of the incompressibility condition $\nabla \cdot \mathbf{v} = 0$ we obtain for the Navier-Stokes equation:

$$\partial_t v_x = \nu \partial_z^2 v_x. \quad (4.3)$$

Making the ansatz

$$v_x(z, t) = e^{-i\omega t} (A \cos(kz) + B \sin(kz)) \quad (4.4)$$

leads to the dispersion relation

$$k = \frac{1 + i}{\delta}, \quad (4.5)$$

where $\delta \equiv \sqrt{\frac{2\nu}{\omega}}$ is the penetration depth of the system. The solution for v_x reads

$$v_x(z, t) = u_0 e^{-i\omega t} \frac{\sin(k(L_z - z))}{\sin(kL_z)}, \quad (4.6)$$

4. Droplet in a time-dependent flow: LBM and MM comparison

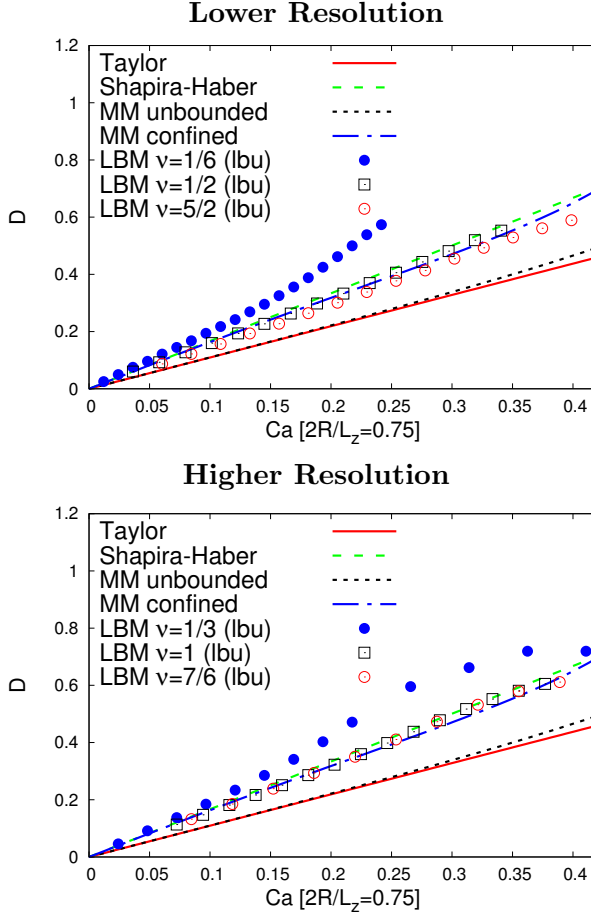


Figure 4.2.: Droplet deformation test benchmarked against several theoretical models: perturbative models in the capillary number Ca , Taylor (unconfined droplet) [19, 20] and Shapira-Haber (accounting for droplet confinement) [39, 40] and models extending the Ca range to higher values, MM-unbounded [16] and the MM-confined [41] model. The extent of the deformation measured by the parameter D is plotted against the capillary number Ca . We choose a series of three Reynolds number ranges by selecting three kinematic viscosities. We can see that the agreement between the LBM simulation and the theoretical predictions improves significantly for lower Reynolds numbers. This is due to the reduction of inertia in the system. Top panel: Resolution $80 \times 40 \times 40$ Bottom panel: Resolution $160 \times 80 \times 80$. To account for similar Reynolds number ranges at a higher resolution the simulations in the bottom panel have higher viscosity values than the one in the top panel.

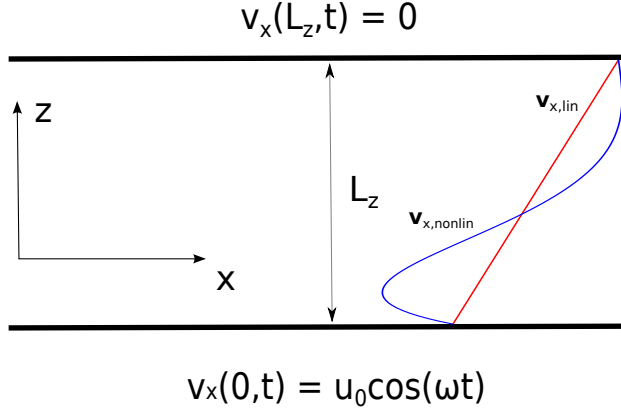


Figure 4.3.: Sketch of the single phase model set-up. A 2D channel of width L_z with one stationary and one oscillating wall. The flow in the x -direction is periodically extended. Two typical velocity profiles of the oscillating channel flow are shown, a linear one in red and a nonlinear one in blue.

whose real part is denoted by $v_x^{(0)}(z, t)$. The velocity profile $v_x(z, t)$ has a linear limit, which is given by the penetration depth δ and the channel width L_z . If $L_z/\delta \ll 1$ the condition for a linear profile is fulfilled, and we get

$$v_x^{(\text{lin})}(z, t) = u_0 \cos(\omega t) \left(1 - \frac{z}{L_z}\right). \quad (4.7)$$

Thus we can find an upper bound for the frequency

$$\omega_c \sim \frac{\nu}{L_z^2} \quad (4.8)$$

so that $L_z/\delta_c \sim 1$, with δ_c being the critical penetration depth of the system. With the analytical solution at hand we can now test our LBM scheme for an external shear flow in a channel including an exact time dependence and perform a “scanning” of the parameter space. In the following we define two error functions based on an L^2 -norm. Deviations from the exact analytical solution $v_x^0(z, t)$ are given by

$$E_x^{(0)} = \left[\frac{1}{L_x L_z} \int_0^{L_x} dx \int_0^{L_z} dz (v_x(x, z, t) - v_x^0(z, t))^2 \right]^{\frac{1}{2}}. \quad (4.9)$$

4. Droplet in a time-dependent flow: LBM and MM comparison

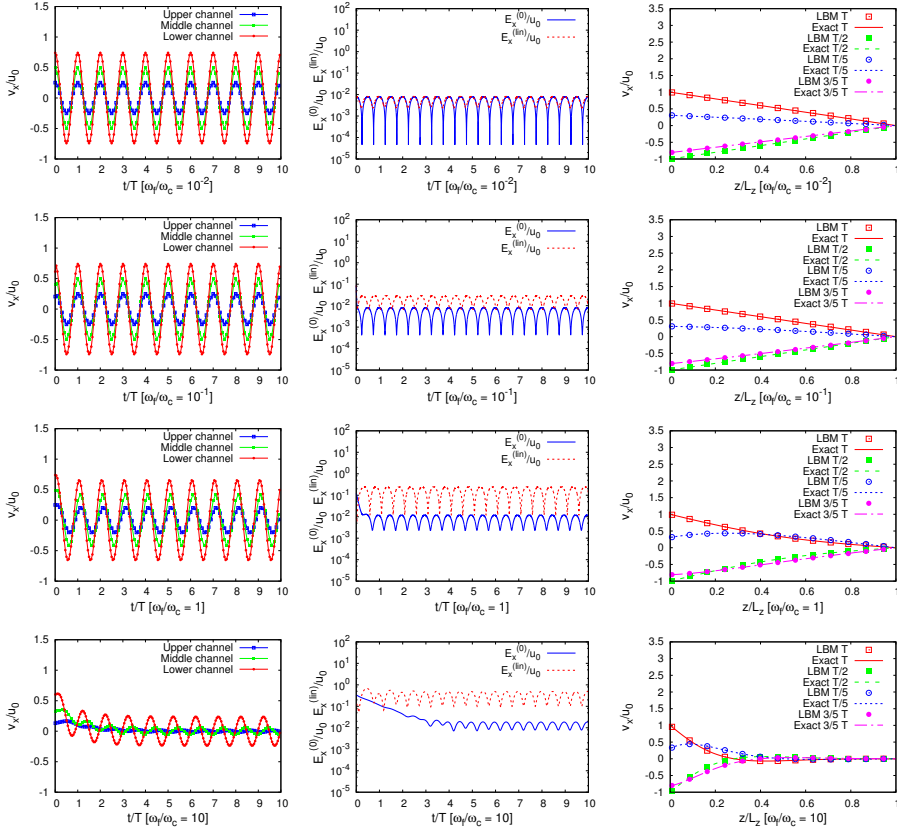


Figure 4.4.: Summary of a LBM benchmark series (channel width $L_z = 128$, relaxation time $\tau = 1$, maximal shear velocity $u_0 = 10^{-3}$) for a single component in the presence of an oscillating shear. Left panels: time evolution of the velocity field at different height locations: upper channel ($z = 3L_z/4$), middle channel ($z = L_z/2$) and lower channel ($z = L_z/4$). We see a transient for higher frequencies $\omega_f/\omega_c \sim 10$, which is due to the relaxation of the velocity field $v(x, z, t)$ to the analytical solution in equation (4.6) from a zero velocity initialisation state. Middle panels: normalized error with respect to the exact solution (equation (4.9)) and normalized error with respect to the linearised solution (equation (4.10)). Right panels: Velocity profile $v_x(z, t)$ as a function of the dimensionless cross-flow coordinate z/L_z at different times $t = T/5, T/2, 3T/5, T$ (in units of the shear period $T = 1/\omega_f$). In all plots we non-dimensionalise the shear frequency ω_f by the critical frequency ω_c . We may notice qualitatively that the velocity profile is becoming gradually more nonlinear with increasing frequency ω_f after passing the critical region $\omega_f/\omega_c \approx 0.1$. This is in agreement with the system parameter scan shown in figure 4.5.

Moreover we define an error function with respect to the linearised solution $v_x^{(\text{lin})}$

$$E_x^{(\text{lin})} = \left[\frac{1}{L_x L_z} \int_0^{L_x} dx \int_0^{L_z} dz (v_x(x, z, t) - v_x^{(\text{lin})}(z, t))^2 \right]^{\frac{1}{2}}. \quad (4.10)$$

We perform several simulations with different oscillation frequencies ranging from $\omega_f = 10^{-7}$ to $\omega_f = 10^{-4}$. We can estimate the critical frequency $\omega_c \approx 10^{-5}$ via equation (4.8), which is supported by figure 4.4, as the velocity profile starts to become linear at around this frequency value. We can also see that the error $E_x^{(0)}$ with respect to the exact solution is (almost) independent of the oscillation frequency ω_f . In addition, we now like to know whether our LBM simulations produce similar results for a choice of different system parameters. A sample of the parameter space is shown in table 4.1. Figure 4.5 is key in understanding the validity of our LBM simulations for the single phase oscillatory shear flow. We can see both that the exact analytical error $E_x^{(0)}$ is generally well behaved (fluctuations around a mean value) for the entire frequency range and that the error to the linearised solution $E_x^{(\text{lin})}$ is well behaved for a frequency range $\omega_f/\omega_c \leq 10^{-1}$ and is increasing for higher frequencies. Thus, we may determine a frequency threshold of about $\omega_f/\omega_c \approx 10^{-1}$ for the linear shear regime for which our LBM solution is both stable and linear.

4.4. Multicomponent oscillating flow

After having investigated the parameter space for a single phase system, we add the droplet. We follow the discussion in [73] yielding a perturbative solution in Ca. Firstly we consider the MM equation in a different non-dimensionalised form with respect to equation (2.13):

$$\begin{aligned} \frac{dM_{ij}}{dt} = & \text{Ca}(t) [f_2(S_{ik}M_{kj} + M_{ik}S_{kj}) + \Omega_{ik}M_{kj} - M_{ik}\Omega_{kj}] \\ & - f_1 \left(M_{ij} - 3 \frac{III_M}{II_M} \delta_{ij} \right), \end{aligned} \quad (4.11)$$

where the time t is given in units of the droplet relaxation time t_d . It is important to note that $\text{Ca}(t)$ is now time-dependent due to the time-dependent external shear flow [70–73]. Following the discussion in [73], we

4. Droplet in a time-dependent flow: LBM and MM comparison

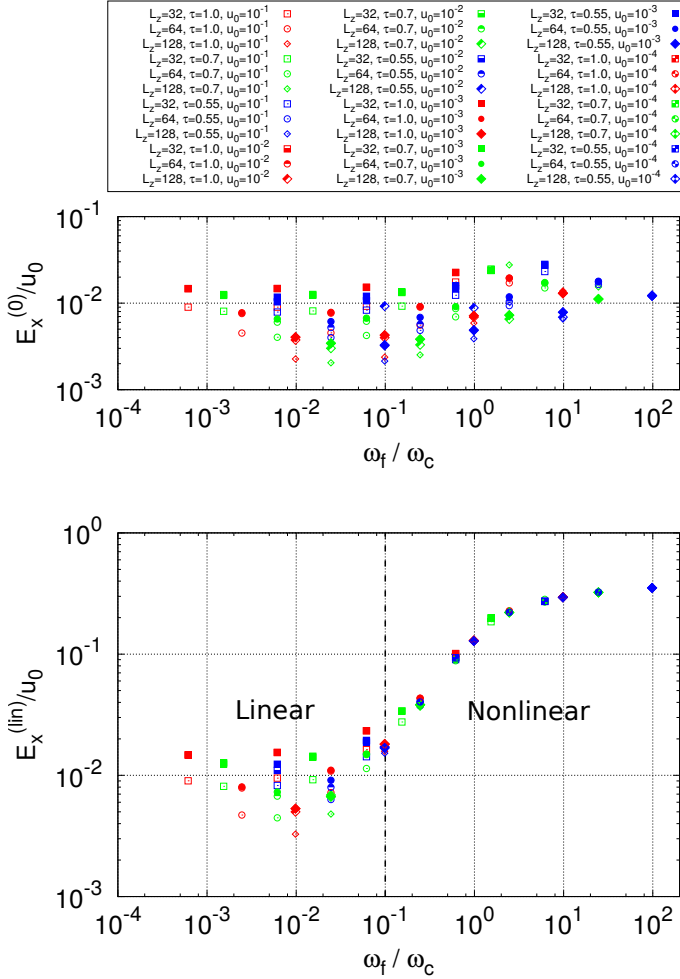


Figure 4.5.: Scatter plot of the averaged analytical error function $E_x^{(0)} \approx \frac{1}{2u_0}(E_{x,max}^{(0)} + E_{x,min}^{(0)})$ and averaged linear error function $E_x^{(lin)} \approx \frac{1}{2u_0}(E_{x,max}^{(0)} + E_{x,min}^{(0)})$ as a function of the renormalised frequency $\frac{\omega_f}{\omega_c}$ with $\omega_c = \frac{\nu}{L_z^2}$ and $\omega_f \equiv \frac{\omega}{2\pi}$. The analytical error $E_x^{(0)}$ is relatively well behaved with a mean value of around 10^{-2} when averaged over the whole frequency range for all parameter set-ups. On the other hand the linear error $E_x^{(lin)}$ shows a clear dependence on the normalised frequency ω_f/ω_c . The linear error is well behaved up until a value of $\omega_f/\omega_c \sim 10^{-1}$, where the shear velocity profile starts becoming non linear, which is demonstrated by the drastic increase in $E_x^{(lin)}$. The two regions, linear and nonlinear, are separated by a dashed vertical line at $\omega_f/\omega_c = 10^{-1}$.

expand the morphology tensor M_{ij} as a perturbation series in the capillary number $\text{Ca}(t)$, see appendix B. Ignoring an initial transient, we end up with the following first order solutions for the squared ellipsoidal axes

$$\begin{aligned}
 \hat{L}^2 &= 1 + \text{Ca}_{\max} f_2 \left(\frac{\omega t_d \cos(\omega t_d t) - f_1 \sin(\omega t_d t)}{f_1^2 + \omega^2 t_d^2} \right) \\
 &\quad + \mathcal{O}(\text{Ca}_{\max}^2), \\
 \hat{W}^2 &= 1 - \text{Ca}_{\max} f_2 \left(\frac{\omega t_d \cos(\omega t_d t) - f_1 \sin(\omega t_d t)}{f_1^2 + \omega^2 t_d^2} \right) \\
 &\quad + \mathcal{O}(\text{Ca}_{\max}^2), \\
 \hat{B}^2 &= 1 + \mathcal{O}(\text{Ca}_{\max}^2),
 \end{aligned} \tag{4.12}$$

where Ca_{\max} denotes the maximal capillary number and t is given in units of t_d . The quantities L^2 , B^2 and W^2 denote the maximal, medium and minimal eigen-directions of the morphology tensor M_{ij} at all times t and are defined via

$$\begin{aligned}
 L^2 &= \|\hat{L}^2, \hat{W}^2\|_{\infty}, \\
 W^2 &= 2 - \|\hat{L}^2, \hat{W}^2\|_{\infty}, \\
 B^2 &= \hat{B}^2,
 \end{aligned} \tag{4.13}$$

where $\|a, b\|_{\infty} \equiv \max(|a|, |b|)$ is the maximum norm between two scalar quantities a and b . Besides the three ellipsoidal axes L , B and W another quantity is of particular interest to us. Analogously to [73] we applied a sinusoidal shear rate, so that for the time-dependent capillary number $\text{Ca}(t) \sim \sin(\omega t_d t)$ (t in units of t_d). Thus we can identify a phase shift ϕ between the external oscillatory shear and the droplet's response given by the time evolution of the squared ellipsoidal axes in equation (4.12):

$$\phi = \arctan \left(\frac{\omega t_d}{f_1} \right) + \mathcal{O}(\text{Ca}_{\max}^2), \tag{4.14}$$

which is (for the linearised solution) independent of Ca_{\max} . With our theoretical model at hand we can now run LBM simulations of the droplet in the oscillatory shear flow and check the agreement with the perturbative

4. Droplet in a time-dependent flow: LBM and MM comparison

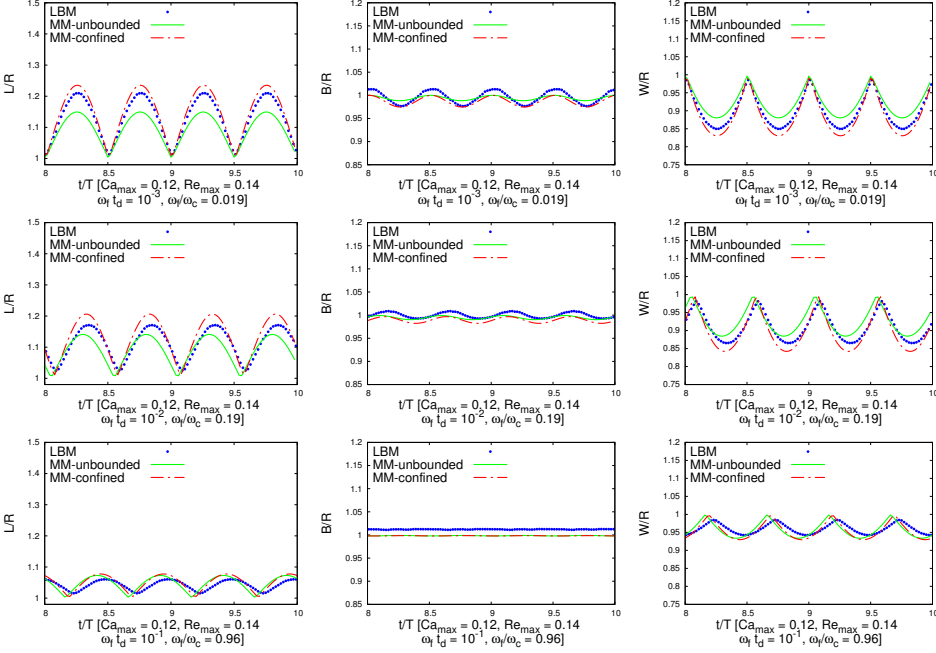


Figure 4.6.: Numerical benchmark for LBM against the MM-confined solution of equation (4.11). The time t is given in units of the shear period $T = 1/\omega_f$. W and L denote the minor and major axes respectively with B being the vorticity axis, where the ellipsoidal axes obey $L > B > W$ at maximal deformation. Four system parameters are of particular relevance: Ca_{\max} and Re_{\max} denote the maximal capillary and Reynolds number (given for the maximum shear at the channel walls) which remain fixed in the plots. ω_f/ω_c is a measure of the linearity of the shear flow, where $\omega_f/\omega_c \sim 1$ may be seen as a limiting value for linearity (see section 4.3). $\omega_f t_d$ denotes the oscillation frequency in units of the reciprocal droplet relaxation time and is the control parameter here. We may observe qualitatively that as the oscillation frequency tends to values close to $\omega_f t_d \sim 1$ the droplet deformation decreases and undergoes a phase shift with respect to the outer shear flow at the walls.

theoretical predictions in equation (4.12). However, the perturbative analytical solution is only valid in a small capillary Ca_{max} range. We can also solve the time-dependent MM-confined equation (4.11) and compare the numerical solution (obtained via a RK-4 scheme) to our LBM simulation results instead of the perturbative solution. It should be remarked that our LBM simulation results may only be compared to the MM-confined model, when the droplet remains an ellipsoid at all times. In order to have a complete overview of the droplet deformation it is paramount to visualise all three major ellipsoidal axes L , B , W , where $L > B > W$ at maximum deformation. Let us look at the top row of figure 4.6. Considering the time evolution of the major axis L and minor axis W we can see that MM-unbounded model is not properly accounting for the confinement of the system ($\alpha = 0.75$). On the other hand our LBM simulation results are in relatively good agreement with the numerical solution of MM-confined. Interestingly, the vorticity axis B is also deformed in time, which is not the case in the perturbative model, since the deformation is due to higher orders $\mathcal{O}(\text{Ca}_{\text{max}}^2)$ in this case. Moving one row further down in figure 4.6, i.e. increasing the previous frequency by a factor 10 we can observe two changes. Firstly, the value of the droplet deformation D is decreasing (for both LBM and the MM-confined solution), and secondly, the time evolution is shifted with respect to the previous row. These effects may be explained by the droplet inertia which tries to resist the outer shear flow. Since $\omega_f t_d \sim 10^{-2}$ we are in the regime where the droplet relaxation time scale is relatively close to the oscillatory shear period $1/\omega_f$. Therefore, we may expect both a decrease in deformation and a phase shift ϕ between the outer shear flow and the time-dependent droplet deformation $D(t)$, as is also predicted by the analytical perturbative solution (see equation (4.14)). The phase shift ϕ is measured in the LBM simulations by the difference in simulation time between the maximal shear intensity G and the maximal droplet deformation D . Increasing the frequency even more to $\omega_f t_d \approx 10^{-1}$ the deformation decreases substantially and the phase shift ϕ is close to $\pi/2$. This indicates that as $\omega_f t_d \rightarrow 1$ the droplet is behaving as if the flow was not present at all. We call this the “transparency” effect, since the droplet seems to be (almost) transparent to the surrounding flow field, which makes itself noticeable by the droplet’s out of phase response and drastic decrease in the deformation parameter D . This decrease in deformation due to a phase shift between applied shear and droplet response has also been experimentally confirmed

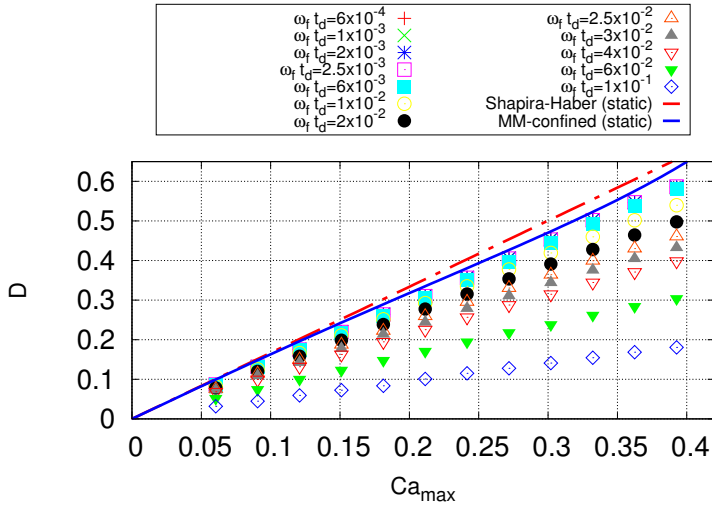


Figure 4.7.: LBM obtained droplet deformation D against Ca_{max} for various values of the normalised shear frequency $\omega_f t_d$. The transparency effect, i.e. the reduction of deformation D for $\omega_f t_d \rightarrow 1$ (see equation (4.12) and figure 4.6) is confirmed. For further clarification the Shapira-Haber and the MM-confined static deformation curves are shown, from which we may see that a relatively low oscillation frequency of about $\omega_f t_d \sim 10^{-3}$ results already in a noticeable decrease in D .

by Cavallo et al. [72], where the authors use a different small amplitude model as a benchmark for their experimental results. For further analysis figure 4.7 shows the LBM droplet deformation results as a function of Ca_{\max} for the simulated frequency range. In figure 4.7 the transparency effect is shown in a more quantitative way. We observe for various simulations, that the deformation drops significantly for increasing frequency ω_f , independently of the capillary number Ca . For further comparison of the droplet deformation scale D the Shapira-Haber [39,40] and MM-confined curves [41] are given as well. Figure 4.8 shows both the deformation D and the phase shift ϕ between the droplet response and the oscillatory shear flow as a function of the normalised frequency $\omega_f t_d$. The general trend is that the deformation D is stationary up until $\omega_f t_d \sim 0.01$ at which point D starts decreasing until the droplet becomes “transparent” to the outer shear flow. We may also see that the phase shift ϕ is starting to increase rapidly at $\omega_f t_d \sim 0.01$ from $\phi \sim 0$ up to $\phi \sim \pi/2$. This reinforces the idea of the droplet transparency effect. Similarly to a forced harmonic oscillator the shear flow is out of phase with the droplet’s response, because the oscillatory shear period $1/\omega_f$ is of comparable size to the droplet relaxation time t_d . The numerical solution of the MM-confined equation (4.11) shown in figure 4.8 is in good agreement with the perturbative analytical solution equation (4.12) for both D and ϕ . The LBM results predict a smaller deformation D and a larger phase shift ϕ compared to the MM-confined model. This may be explained by the very thin droplet interface in the LBM simulation which is roughly the size of 1 grid point. From this estimation we can deduce a relative error of about 0.02 to both the time-dependent values of L and W , resulting in a relative error of about 0.01 for the deformation parameter D . Moreover, it is useful to qualitatively consider streamline plots of the droplet dynamics in both the low and high frequency regions (see figure 4.9). In the low frequency regime for $\omega_f t_d = 0.001$ in figure 4.9 we see the familiar case of static droplet deformation [87], where we have a tilted ellipsoidally deformed droplet (in agreement with the MM-confined model) in the case of maximum deformation coinciding with the instance of the maximum shear due to $\phi \ll 1$. In the high frequency regime $\omega_f t_d = 0.1$ in figure 4.9 we see now that the droplet is only slightly deformed in the case of maximal deformation. Since the phase shift $\phi \approx \pi/2$ now, the velocity magnitude of the oscillatory shear flow is almost 0 at the walls. We observe that the regions of highest shear flow intensity are in fact close to the droplet interface

(disregarding the two channel wakes produced by the droplet). Thus the internal droplet dynamics substantially influences the oscillatory shear flow close to the interface in the high frequency regime. This is a consequence of the two-way coupling of the Multicomponent LBM scheme.

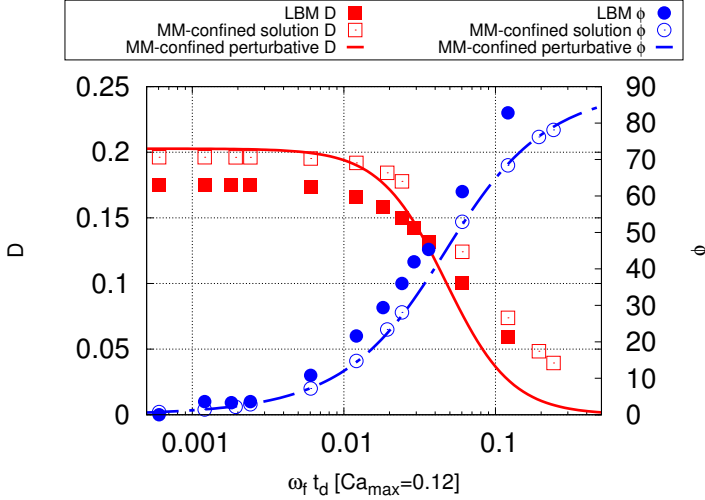
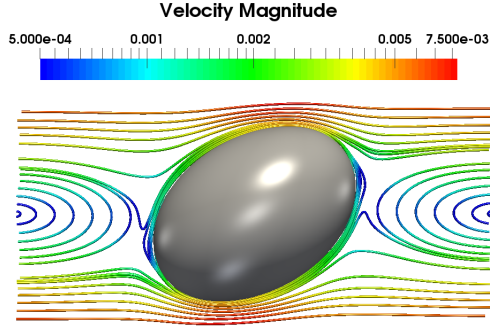


Figure 4.8.: Droplet deformation D and phase shift ϕ between the shear flow and the droplet’s response for a fixed maximal capillary number Ca_{max} against the normalised frequency $\omega_f t_d$. The LBM measured droplet deformation D is in good agreement with the MM-confined prediction (see figure 4.2 for the static benchmark). The droplet transparency effect seems to come into effect at around $\omega_f t_d \sim 10^{-2}$, where a gradual decrease in D is noticeable in both MM-confined and LBM results. MM-confined and LBM agree furthermore on the phase shift ϕ which increases from $\phi \sim 0$ to $\phi \sim \pi/2$ for the highest measured frequencies. This indicates an out of phase droplet response to the underlying shear flow. For further clarification the linearised perturbative MM-confined solution, equation (4.12), is also shown.

4.5. Conclusion

We have demonstrated that a Shan-Chen multicomponent LBM set up with particularly chosen boundary conditions yields reliable results for confined time-dependent droplet deformation. After validations in the static case [19, 20, 39, 40], we have checked the LBM results against a variety of time-dependent theoretical models [16, 41, 73]. Specifically, after introducing a

Low shear frequency $\omega_f t_d = 0.001$, $Ca_{\max} = 0.12$



High shear frequency $\omega_f t_d = 0.1$, $Ca_{\max} = 0.12$

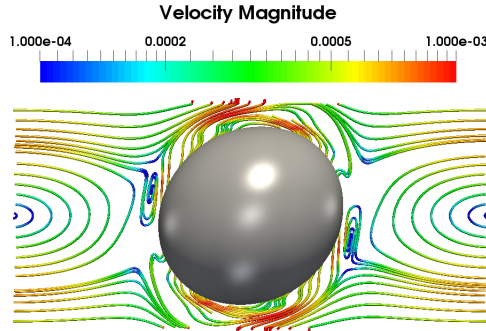


Figure 4.9.: Streamline plots of the LBM droplet simulations at maximum deformation for $Ca_{\max} = 0.12$ and $Re_{\max} \approx 0.1$. Top panel: Low frequency regime $\omega_f t_d = 0.001$. The droplet is ellipsoidally deformed and tilted in the channel, similarly to static droplet deformation dynamics [87]. The droplet produces two wakes in the channel and the velocity magnitude is largest at the channel walls. Bottom panel: High frequency regime $\omega_f t_d = 0.1$. The droplet is only marginally deformed due to the “transparency effect” at non-dimensionalised high frequencies $\omega_f t_d$. We observe once again two wakes in the flow field in the vicinity of the droplet. Due to $\phi \approx \pi/2$ (phase shift between underlying oscillatory shear and droplet deformation) the velocity magnitude is largest at the droplet interface instead of the channel walls. The droplet is deforming the underlying oscillatory shear flow through its own internal dynamics (two-way coupling).

time dependence into the system via a monochromatic shear, the LBM simulations agree fairly well with theoretical models and discrepancies are likely due to the interface thickness in the LBM model. The simulations in this work have been carried out with a boundary scheme using ghost nodes which is, on the one hand, equivalent to a wall bounce back scheme, but, on the other hand, may be extended to model more complex external flows than those treated here. Therefore, our simulations, both in the case of single phase and multicomponent flows, are useful validation tests of a boundary method involving ghost nodes, which can be extended to an exact flow boundary scheme, similarly to [101, 102]. The work in this chapter is extended to consider the rather interesting aspect of frequency dependent droplet breakup in highly confined flows in chapter 5. Furthermore, we will see in chapters 6 and 7 that the underlying LBM ghost node boundary flow scheme described here may be extended to accurately simulate an “ab-initio” droplet in a turbulent flow [13, 15, 17].

L_z (lbu)	τ (lbu)	u_0 (lbu)	ω_f (lbu)	$E_{x,min}^{(\text{lin})}/u_0$	$E_{x,max}^{(0)}/u_0$
128	1.0	10^{-2}	10^{-7}	$0.7461 \cdot 10^{-2}$	$0.2442 \cdot 10^{-2}$
128	1.0	10^{-2}	10^{-6}	$0.7527 \cdot 10^{-2}$	$0.6827 \cdot 10^{-2}$
128	1.0	10^{-2}	10^{-5}	$1.2556 \cdot 10^{-2}$	$1.1707 \cdot 10^{-2}$
128	1.0	10^{-2}	10^{-4}	$1.8881 \cdot 10^{-2}$	$9.9081 \cdot 10^{-2}$
64	1.0	10^{-3}	10^{-7}	$1.542 \cdot 10^{-2}$	$0.063 \cdot 10^{-2}$
64	1.0	10^{-3}	10^{-6}	$1.543 \cdot 10^{-2}$	$0.595 \cdot 10^{-2}$
64	1.0	10^{-3}	10^{-5}	$1.633 \cdot 10^{-2}$	$1.171 \cdot 10^{-2}$
64	1.0	10^{-3}	10^{-4}	$2.909 \cdot 10^{-2}$	$4.833 \cdot 10^{-2}$
128	0.7	10^{-3}	10^{-7}	$0.447 \cdot 10^{-2}$	$0.679 \cdot 10^{-2}$
128	0.7	10^{-3}	10^{-6}	$0.486 \cdot 10^{-2}$	$0.701 \cdot 10^{-2}$
128	0.7	10^{-3}	10^{-5}	$5.087 \cdot 10^{-2}$	$1.106 \cdot 10^{-2}$
128	0.7	10^{-3}	10^{-4}	$12.972 \cdot 10^{-2}$	$1.558 \cdot 10^{-2}$
128	1.0	10^{-3}	10^{-7}	$0.243 \cdot 10^{-2}$	$0.803 \cdot 10^{-2}$
128	1.0	10^{-3}	10^{-6}	$0.660 \cdot 10^{-2}$	$0.810 \cdot 10^{-2}$
128	1.0	10^{-3}	10^{-5}	$1.185 \cdot 10^{-2}$	$1.192 \cdot 10^{-2}$
128	1.0	10^{-3}	10^{-4}	$9.900 \cdot 10^{-2}$	$1.893 \cdot 10^{-2}$

Table 4.1.: System parameter scan of the single phase oscillatory channel flow (see section 4.3). A few representative cases are reported of changing the channel width L_z , the LBM relaxation time τ , the maximum wall velocity u_0 , the shear oscillation frequency ω_f .

5. Droplet breakup in a confined and time-dependent flow

In this chapter ¹ we investigate droplet breakup in confined and time-dependent oscillatory shear flows using the same set up as in chapter 4. We see that breakup is not only dependent on the oscillatory frequency of the outer shear flow, but also on start up conditions and the degree of confinement: two very different flow start up conditions yield two quantitatively different results in the case of low shear frequencies and high degrees of confinement. Moreover, we investigate the effect of inertia and flow topology on the breakup conditions and the mismatch between the two flow start up protocols.

5.1. Introduction

Fluid dynamics phenomena, involving droplet dynamics, deformation and breakup, are prominent in the field of microfluidics and even in general complex flows at larger scales. Beyond the practical importance in a variety of concrete applications [1–4], they are also relevant from the theoretical point of view, due to the complexity of the physics involved [19, 22, 25, 27, 103]. The value of the capillary number Ca at breakup is denoted by Ca_{cr} , the critical capillary number. A lot of attention has been dedicated to droplet deformation and breakup in stationary flows [22–24], and in particular the effect of the degree of confinement α , see equation (2.19), on the flow dynamics [26, 28, 29]. Confinement is frequently encountered in experimental set ups of droplet dynamics in simple shear flows [26, 28–38] and can be enhanced by changing α . There are some theoretical models which were developed to capture the experimental phenomenology of confined droplet dynamics, analytical models [39, 40], which extended the theory by Taylor [19, 20], and

¹Submitted as: Milan, F., Biferale, L., Sbragaglia, M., Toschi, F., *Lattice Boltzmann simulations of droplet breakup in confined and time-dependent flows*

phenomenological models [16, 41, 42]. The validity of the analytical models were verified in [43] and the phenomenological models in [44]. Of particular interest are the results in [28], which show that, for non vanishing α breakup differs substantially from the unconfined shear case both qualitatively and quantitatively for various viscosity ratios χ . Additionally, the dependency of the critical capillary number Ca_{cr} on the droplet's inertia is a central area of interest [12, 25, 45–64]. Furthermore, breakup is influenced by the start up conditions, as demonstrated in experimental and theoretical studies [65–69]. This phenomenon is rather subtle and can have different effects depending on the protocol in use. The dependency on the rate of increase of the shear rate G was confirmed by [65] via supporting calculations based on the model by Taylor [19]. A theoretical model developed by Hinch et al. [66] shows that stable droplet equilibria below the critical capillary number Ca_{cr} are only possible for a sufficiently low increase in G . Furthermore Renardy [69] has shown that, although these stable equilibria require a slow increase in the shear rate G , they are unique and do not depend on the rate of change of G . We stress that even though the effect of start up conditions on breakup has been investigated [65–69], the role of confinement with varying start up conditions on droplet dynamics and breakup is not clear. Moreover, it is unclear how breakup is affected, if the flows are time-dependent [70–74]. The aim of this chapter is to take a step further in this direction. With the use of numerical simulations we show that at capillary numbers close to breakup, confinement allows for the existence of a metastable flow configuration next to the solution of the Stokes equation found in [69]. This metastable state is prone to perturbations and collapses to the Stokes solution, if we have a time dependent flow with a sufficiently large shear frequency. It should be stressed that this result is unique to the case of a confined droplet in an oscillatory shear, as this metastable configuration is not present neither for an unconfined droplet in an oscillatory shear flow nor in the case of an oscillatory elongational flow. Our studies can be seen as an extension to [46, 69], where the influence of inertia on droplet breakup was studied, whereas we deal with time-dependent cases, where the temporal rate of change of the shear intensity is comparable to the droplet relaxation time. This chapter extends the work produced in chapter 4, where stable time-dependent droplet dynamics was investigated via a multicomponent Lattice Boltzmann scheme [74] and a phenomenological model [16, 41].

This chapter is organized as follows: in section 5.2 we outline the general details of droplet breakup with an emphasis on confined systems and simple shear flows. In section 5.3 we investigate breakup in a time-dependent (oscillatory) shear flow under strong confinement. A mismatch between two protocols, involving different start up conditions of the flow, leads us to investigate breakup conditions under the influence of inertia (section 5.4) and the effect of confinement (section 5.5). Moreover, we check whether the protocol mismatch depends on the flow topology (section 5.6).

5.2. Simulation set up and definitions

In this section we define what we mean when we speak of droplet breakup and characterise the simulation set ups. We deal with both a confined droplet in a simple shear flow and an unconfined droplet in a uniaxial extensional (elongational) flow. The velocity gradient matrix for both shear and elongational flows is given by

$$\nabla \mathbf{v} = \frac{G}{2} \begin{pmatrix} \beta & 0 & 2(1 - \beta) \\ 0 & \beta & 0 \\ 0 & 0 & -2\beta \end{pmatrix} \quad (5.1)$$

where $\|\nabla \mathbf{v}\| = G$ and β is a parameter characterising the flow type. The shear flow set up is equivalent to the one used in [74] with $\beta = 0$ in equation (5.1) except that the flow is unconfined and elongational with an oscillatory velocity gradient amplitude $G(t)$ given by equation (5.1) with $\beta = 1$. Droplet deformation can be characterised by the capillary number Ca . In the case of a shear flow including confinement the shear rate is given by

$$G = \frac{2u_0}{L_z} \quad (5.2)$$

with L_z being the channel width responsible for the droplet confinement and u_0 being the maximum wall velocity amplitude. This definition may also be extended to time-dependent shear flows [74]

$$G(t) = \frac{2u(t)}{L_z} \quad (5.3)$$

5. Droplet breakup in a confined time-dependent flow

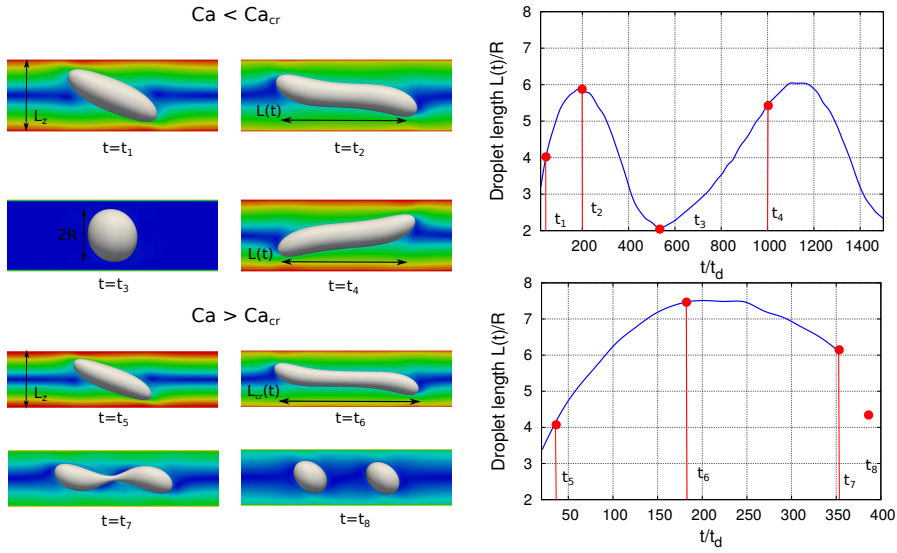


Figure 5.1.: Droplet in a confined oscillatory shear flow with a non-dimensionalised oscillation frequency $\omega_f t_d$. Snapshots of the droplet in the velocity field are shown for $Ca < Ca_{cr}$ and $Ca > Ca_{cr}$. The plots on the right panel shows the time evolution of the normalised droplet length $L(t)/R$. The degree of confinement of the system is given by $\alpha = 2R/L_z$, where R is the droplet radius of the undeformed droplet and L_z the wall separation.

In accordance with [28] we define the critical capillary number Ca_{cr} as the value of Ca for which an initially spherical droplet breaks up, which is achieved by a sudden increase in the shear rate amplitude G . We refer to this breakup protocol as the *Shock Method*. In addition we can gradually increase the shear rate G starting from a value for which the droplet is only marginally deformed [65, 66, 69]. A fixed increase ΔG , or Δu_0 in the case of equation (5.3), is equivalent to a fixed increment rate ΔCa for the capillary number. This way the droplet and the solvent flow are given more time to relax to their respective equilibrium distributions at specific Ca . We call this protocol the *Relaxation method*. A variation of the relaxation method for time-dependent oscillatory flows, i.e. where the shear amplitude $G(t) = G_0 \cos(\omega t)$, is to consider the flow and droplet configuration at a capillary number Ca close to Ca_{cr} and then to increase the oscillatory shear frequency $\omega_f = \omega/(2\pi)$ until breakup, starting from the stationary case of $\omega_f = 0$. As in [74] we use a dimensionless frequency $\omega_f t_d$ in our discussion, where t_d is the droplet relaxation time defined in equation (4.1). In the presence of a flow with non-zero frequency $\omega_f t_d$, we focus on Ca_{max} , which denotes the maximum value of the time-dependent capillary number $\text{Ca}(t)$ over one oscillatory cycle [74]. An instance of droplet breakup in an oscillatory simple shear flow is depicted in figure 5.1. The droplet is oscillating between two maximally elongated states for $\text{Ca} < \text{Ca}_{\text{cr}}$ and breaks up during the flow build up for $\text{Ca} > \text{Ca}_{\text{cr}}$ in the case of the shock method. The droplet elongation is characterised by the droplet length $L(t)$, which is defined as the longest axis of the elongated droplet and L_{cr} denotes the droplet length in the critical case $\text{Ca} \geq \text{Ca}_{\text{cr}}$. The time evolution of $L(t)$ is also shown for the two cases $\text{Ca} < \text{Ca}_{\text{cr}}$ and $\text{Ca} > \text{Ca}_{\text{cr}}$ in figure 5.1, which shows that breakup occurs at around $t = 17000$ lbu with lbu denoting Lattice Boltzmann Units. In all simulations in this article the viscous ratio $\chi \equiv 1$ and the density ratio $\rho_d/\rho_s \equiv 1$. If not explicitly stated otherwise, the confinement ratio is set to $\alpha = 0.75$.

5.3. Droplet breakup in an oscillatory shear flow

Similarly to [74] we consider a droplet in a confined oscillatory shear flow, see figure 5.2, for the flow pattern. The set up is shown in figure 5.1 with a confinement ratio $\alpha = 0.75$ and a time-dependent shear rate $G(t) = 2u_0/L_z \cos(2\pi\omega_f t)$, where ω_f is the frequency of the outer oscillatory flow [70–

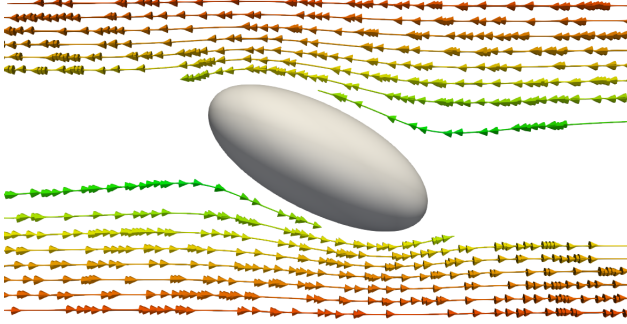


Figure 5.2.: Planar cut of a droplet in a shear flow, where the flow is visualised by streamlines coloured according to the magnitude of the velocity field.

74]. Our main focus is the dependency of Ca_{cr} on the normalised shear frequency $\omega_f t_d$ of the oscillatory outer flow. Droplet dynamics in oscillating shear flows feature a so called transparency effect [74], which states that the droplet is hardly deformed, if $\omega_f t_d \sim 0.1$, i.e. the time scale of the oscillating shear flow $1/\omega_f$ is of a similar order as the droplet relaxation time scale t_d . The droplet dynamics are hardly influenced by the shear frequency for $\omega_f t_d \sim 10^{-4}$ and the transparency effect is noticeable for $\omega_f t_d \sim 10^{-2}$ and higher frequencies, which leads to a sudden increase in the critical capillary number. To be able to compare the LBM simulations with experimental results [26, 28, 35, 36], we limit the range of the critical capillary number close to $Ca_{cr} \sim 1.0$. In figure 5.3 we can see that the droplet breakup behaviour is significantly different for our two LBM simulation protocols, the shock and relaxation method. The shock method implies that droplet breakup is independent of the oscillatory shear frequency $\omega_f t_d$, significant changes in Ca_{cr} only occur close to the transparency effect region at high frequencies ($\omega_f t_d \sim 10^{-2}$). The relaxation method is of a different nature: first of all Ca_{cr} in the low frequency region ($\omega_f t_d \sim 10^{-4}$) is larger than the values obtained with the shock method, see also section 5.5. Moreover, for intermediate frequencies $\omega_f t_d \sim 5 \times 10^{-3}$ we observe that breakup occurs at a significantly smaller Ca_{cr} than in the low frequency range and is now of a comparable value to Ca_{cr} obtained via the shock method. The mismatch between the two protocols in the low frequency regime in figure 5.3 is in disagreement with previous studies of start up conditions of droplet

breakup in confined simple shear flows [28, 69]. However, the shock method produces results in accordance with the literature [28], as the dashed line in figure 5.3 indicates. It should also be noted, that the destabilization of the “relaxation branch” is rather sudden and takes place at very small ω_{ftd} . This suggests that the protocol mismatch is due to a metastable solution (relaxation method) existing next to a stable solution (shock method) in the low frequency range $\omega_{ftd} \leq 0.02$. The protocol mismatch seems rather puzzling: according to Renardy [69] the solution should be unique. However, our set up differs in a few points from the one in Renardy [69]. First of all, the droplet is strongly confined ($\alpha = 0.75$) in our set up (see figure 5.1), which could have a strong effect on the values Ca_{cr} for varying start up conditions. Moreover, inertia might stabilise the droplet in the case of the relaxation method. Therefore, the protocol mismatch might disappear in the Stokes limit. In addition, one may also wonder, if the flow topology plays a role, as an inherently different flow field might lead to a similar protocol mismatch. Given these considerations, we investigate the cause of the mismatch by considering both inertial effects, as is the case in [69], see section 5.4, and the importance of confinement in stationary shear flows, see section 5.5, in the following sections. Regarding the importance of flow topology, we investigate time-dependent breakup in an elongational flow in section 5.6.

5.4. Inertial effects

In [69] it is shown that the solution of the Stokes equation in confined simple shear flows is unique and does not depend on neither the initial conditions of the droplet nor the solvent flow configuration. Thus, one might think that the protocol mismatch might be due to inertial effects and would disappear, if we were close the Stokes limit of $\text{Re} \equiv 0$. Interestingly, the LBM formalism allows us to directly set $\text{Re} = 0$, as we can eliminate the non-linear terms in the equilibrium distribution functions in the LBM algorithm, equation (3.6), which leads us to a modified equation (5.4), accounting only for the linear terms in the flow field $\mathbf{u}(\mathbf{x}, t)$. Inertial effects tend to stabilise the droplet [67, 68] for low $\text{Re} < 1$, whereas $\text{Ca}_{\text{cr}} \sim 1/\text{Re}$ for large $\text{Re} > 10$ [46]. This suggests, that the stabilisation effect of low Re are responsible for the protocol mismatch, which consequently should disappear in the Stokes limit $\text{Re} = 0$. We investigate the dependency of Ca_{cr} on Re ,

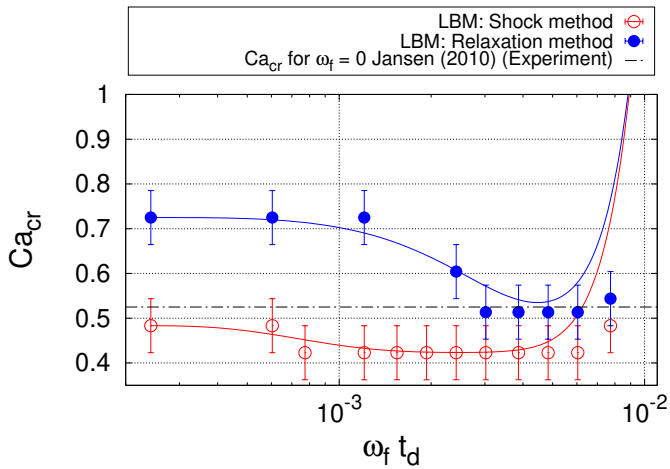


Figure 5.3.: Critical capillary number Ca_{cr} at varying frequencies $\omega_f t_d$. There is a mismatch between the predictions of the two breakup protocols. Whereas droplet breakup is largely independent in the case of the shock method, except for the asymptotic behaviour in the high frequency region, the relaxation method in the low frequency limit predicts a higher Ca_{cr} than the ones of the shock method. This mismatch is investigated in the article. The error bars are estimated via steps in the critical capillary number ΔCa , which indicate the steps taken during the flow start up in the relaxation method. Both curves are interpolated via bezier curves.

as shown in figure 5.4. For the case $Re = 0$ we use only the linear terms of the equilibrium distribution functions given by

$$g_i^{\text{eq,lin}}(\mathbf{x}, t) = \rho_b(\mathbf{x}, t) w_i (1 + 3 \mathbf{c}_i \cdot \mathbf{u}) \quad (5.4)$$

The simulations are carried out for a stationary shear flow, with the set up described in figure 5.1. We can see that the mismatch between the breakup protocols does not depend on inertia and is even present in the Stokes limit of $Re = 0$. We conclude that the mismatch between the two breakup protocols is not influenced by any stabilisation effects of inertia [67, 68] for the given range of Reynolds numbers $Re \sim 0.0, \dots, 1.5$.

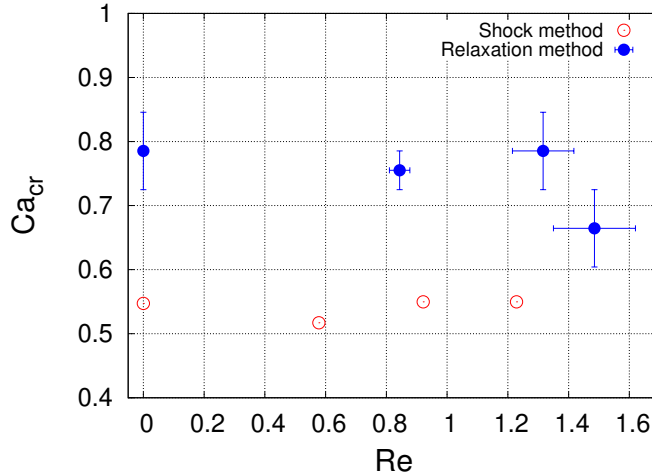


Figure 5.4.: Ca_{cr} vs Reynolds number Re . The mismatch between the shock and relaxation breakup protocols does not depend on inertia. This is especially clear in the case of the Stokes solution, for which $Re = 0$. The error bars are estimated via steps in the critical capillary ΔCa and Reynolds number ΔRe .

5.5. Confinement effects

Now we focus on both confinement and start up conditions in the shear rate amplitude G for droplet breakup in a stationary shear flow. The set up is once again the one in figure 5.1, a confined droplet in a stationary ($\omega_f t_d = 0$) shear flow, but now we vary the confinement ratio α and, in the case of the relaxation method, the rate of change of the shear amplitude G , resulting

in increments of the capillary number ΔCa . Our results are summarised in figure 5.5. We can see, as was shown in [69], that the critical capillary number Ca_{cr} is independent of the start up conditions for low confinement ratios ($\alpha \leq 0.5$), as both the shock method and the relaxation method yield the same results with respect to the simulation errors. However, if the droplet is strongly confined ($\alpha \geq 0.6$), the two methods yield very different results, with the Ca_{cr} predicted by the relaxation method being substantially larger than the one predicted by the shock method. Figure 5.6 shows the length of the elongated droplet as a function of the LBM simulation time for the different shear start up methods: we can see that for the shock method droplet breakup occurs soon after the maximal elongation, whereas for the relaxation method the droplet experiences a sequence of maximal extensions and subsequent retractions after breaking up, for a given Ca_{cr} at its critical length $L_{\text{cr}}(t)$. We conclude that both a slow start up of the outer flow (relaxation method) and a strong confinement of the droplet ($\alpha \geq 0.6$) are necessary for the mismatch reported in figure 5.3 in the low frequency limit. The eventual collapse of the relaxation method solution on to the one found by the shock method suggests, that the relaxation method branch in the low frequency limit in figure 5.3 is a metastable state, explaining the high susceptibility to small perturbations and the collapse to the configuration obtained by the shock method for intermediate oscillatory frequencies $\omega_f t_d$.

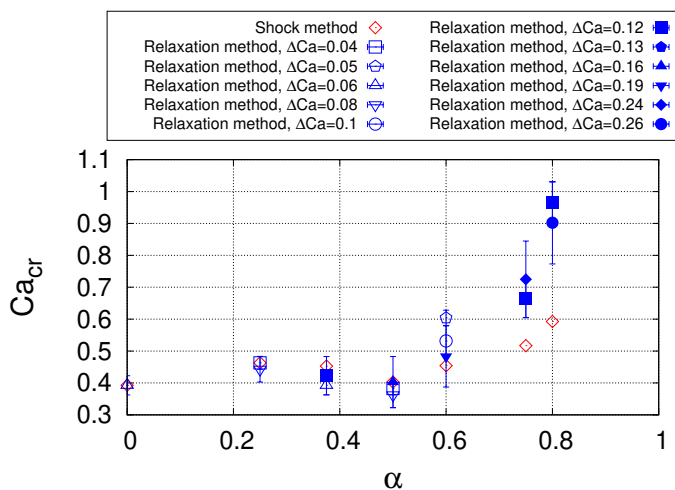


Figure 5.5.: Critical capillary number Ca_{cr} for different confinement ratios $\alpha = 2R/L_z$. We compare the values obtained by the LBM simulations with the shock method and the ones obtained by the relaxation method. Since the relaxation method is dependent on the start up conditions of the outer flow and the droplet, we provide a range of different increments ΔCa , where smaller ΔCa denote a slower and flow build up and vice versa. The error bars are estimated via steps in the critical capillary number ΔCa .

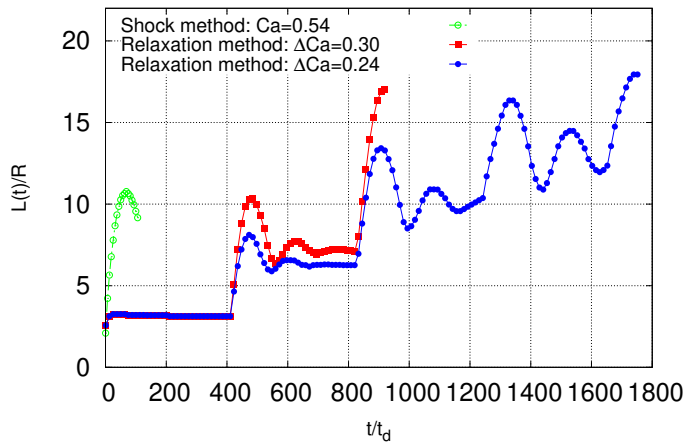


Figure 5.6.: Normalised droplet major axis $L(t)/R$ against the LBM simulation time t given in units of the droplet relaxation time t_d . The droplet breaks up shortly after its maximum elongation for the shock method. breakup in the relaxation method is dependent on the shear rate and thus capillary number increase: a) for a rate with increment $\Delta Ca = 0.30$ the droplet relaxes after reaching its maximum elongation for the first time to breakup at a longer length at a higher Ca_{cr} later on. b) for a smaller capillary number increase $\Delta Ca = 0.24$ the droplet length at Ca_{cr} increases even further and the $L(t)$ contains more full extensions and subsequent retractions.

5.6. Flow topology

After having dealt with confinement effects, we investigate the protocol mismatch in terms of the flow topology. Instead of an oscillatory shear flow, we consider breakup in an elongational (or uniaxial extensional) flow, see figure 5.7. This flow is by its very nature unconfined, so we would expect not to see a mismatch, as is the case for $\alpha = 0$ in the case of the confined shear flow, see section 5.5. The results are shown in figure 5.8. Interestingly, a mismatch between the two droplet protocols is absent and the predictions agree well with each other in terms of their respective errors. This shows that strong confinement ($\alpha \geq 0.75$) is necessary for the existence of the protocol mismatch shown in figure 5.3. Moreover, figure 5.8, shows that droplet breakup in an oscillatory elongational flow is frequency dependent, with an exponential dependence between the oscillation frequency $\omega_f t_d$ and the critical capillary number Ca_{cr} . The low frequency limit matches the stationary flow predictions of [51].

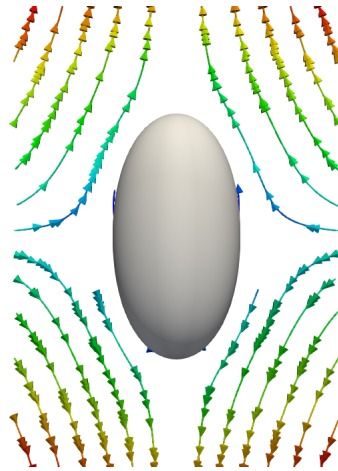


Figure 5.7.: The flow layout of a droplet in an elongational (uniaxial extensional) flow. The image is a planar cut, with the flow being rotationally symmetric around the elongated droplet axis in the image. The streamlines are coloured according to the magnitude of the velocity field of the solvent.

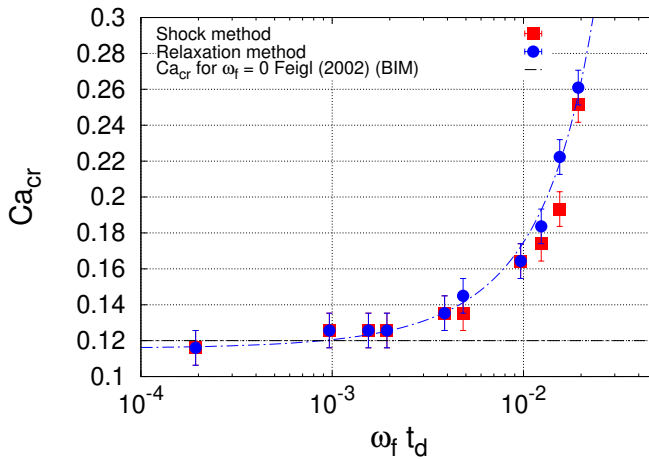


Figure 5.8.: Critical capillary number Ca_{cr} against different frequencies $\omega_f t_d$ for a droplet in an unconfined elongational flow. We consider the two breakup protocols, the shock method and the relaxation method. Even though the droplet breakup is dependent on the shear rate frequency $\omega_f t_d$, a protocol mismatch does not occur, contrary to the case of the confined shear flow topology. The error bars are estimated via steps in the critical capillary number ΔCa .

5.7. Conclusion

We have shown that the interplay of varying start up conditions and strong confinement ratios can lead to qualitatively and quantitatively different droplet breakup conditions in stationary shear flows, unlike the stable equilibria found for varying start up conditions [69] or the ones found for varying degrees of confinement [28]. Having investigated the effects of inertia, confinement and flow topology, we conclude that the protocol mismatch between the shock and the relaxation method are due to a high degree of confinement for a droplet in a shear flow ($\alpha = 0.75$). However, the breakup solution found via the relaxation method is only metastable, since it becomes unstable in the case of a time-dependent, oscillatory shear flow. The protocol mismatch is thus solely due to an extra metastable solution in a strongly confined shear flow and it disappears in the presence of small perturbations, e.g. amplitude variations in an oscillatory shear flow, in accordance with the uniqueness of the Stokes solution [28,69]. We have also shown the dependency of the critical capillary number Ca_{cr} on the normalised oscillation frequency $\omega_f t_d$ in both oscillatory shear and elongational flows. In the case of the elongational flow, Ca_{cr} increases with increasing $\omega_f t_d$, whereas no simple functional dependence can be found for the oscillatory shear flow, since Ca_{cr} also depends on the flow start up and degree of confinement. It would be interesting to see whether the metastable solution can be found in an experimental set up or whether it is too prone to perturbations to manifests itself.

6. LBM scheme for a sub-Kolmogorov droplet in HIT

In this chapter ¹ we elaborate on the ghost node boundary flow introduced in chapter 3 and show that it can be used to model droplet dynamics on the sub-Kolmogorov scale. Instead of using an analytical flow field, as was the case in chapters 4 and 5, we use a fully developed turbulent flow field, which we retrieve from pseudo-spectral simulation data of trajectories of passive tracers in homogeneous isotropic turbulence. We will outline the conditions for the local Reynolds number and the velocity profile on the sub-Kolmogorov scale and will test the algorithm in the case of a single phase turbulent flow.

6.1. Introduction

Exact flow boundary conditions for LBM are a very useful tool for multiscale physics simulations, as it is enabling scale separation in its very own nature. For example, we may model the dynamics of a droplet in a turbulent flow field on the sub-Kolmogorov scale, without having to simulate the scale of the largest turbulent eddies of size l_0 (see chapter 2). Exact flow boundaries for LBM were first developed by [100] for 2D lattices and then extended to 3D flows by [101, 122, 123] for perpendicular inlet and outlet flows. In [102] it is shown that exact boundary flow conditions can be implemented in 3D LBM simulations for the D3Q19 lattice. The method presented in [102] is useful for no-slip LBM boundary flow conditions [124–126], as it is able to eliminate numerical artefacts. Moreover, the D3Q19 exact boundary flow method in [102] seems to be most adapt for LBM hybrid simulations [127–129], for example coupling the results of a DNS solver for the incompressible NSE with a multicomponent LBM simulation. Even though the scheme presented

¹In preparation as: Milan, F., Sbragaglia, M., Biferale, L., Toschi, F., *Sub-Kolmogorov droplet dynamics in isotropic turbulence using a multiscale Lattice Boltzmann scheme*

in [102] seems rather suitable in modelling a sub-Kolmogorov droplet in homogeneous isotropic turbulence, we use the ghost node boundary flow method outlined in section 3.5. The main reason for this is that the method in [102] cannot determine both the density $\rho_b(\mathbf{x}, t)$ and the velocity field $\mathbf{v}(\mathbf{x}, t)$ at the lattice domain boundary. Since we require a constant density ratio of ρ_a/ρ_s for our hybrid simulations, we use the ghost node boundary scheme, which does not set constraints to either the density nor the velocity field at the boundary.

6.2. Structure of the algorithm

We have introduced the ghost node boundary flow method in section 3.5 as an exact flow boundary method: the boundary scheme enables us to enforce a density field $\rho(\mathbf{x}, t)$ and $\mathbf{u}(\mathbf{x}, t)$ at the boundaries at any LBM simulation time step t . A concrete set up for the sub-Kolmogorov droplet in homogeneous isotropic turbulence is given in figure 6.2. A droplet with radius R in the undeformed stage is at the centre of a simulation box of length L_s . The blue dots at the faces of the simulation box denote the ghost nodes, which according to equation (3.24) contain the macroscopic boundary values, the density $\rho_b(\mathbf{x}, t)$ and the velocity $\mathbf{u}(\mathbf{x}, t)$. As in previous chapters we deal with a density ratio of 1 and thus choose $\rho_b(\mathbf{x}, t)$ accordingly, whereby $\rho_b = \text{constant}$. However, the velocity field $\mathbf{u}(\mathbf{x}, t)$ is now updated via pseudo-spectral (PS) data of passive trajectories in turbulent flows², see figure 6.1. All the turbulent trajectories have a Taylor Reynolds number of $\text{Re}_\lambda = 420$. We consider droplets below the Kolmogorov scale, i.e. $R \ll \eta_K$, as we can limit ourselves to a linear velocity profile in this case [14], where we use the notation $G_{ij}(t) \equiv \partial_j v_i(\mathbf{x}, t)$ for the velocity gradient tensor. The typical velocity increments [6] of separation \mathbf{l} of size $|\mathbf{l}| = l$ are

$$\delta v_i(\mathbf{x}, \mathbf{l}) = v_i(\mathbf{x} + \mathbf{l}) - v_i(\mathbf{x}) \quad (6.1)$$

which can be approximated by

$$\delta v_i(\mathbf{x}, \mathbf{l}) = \underbrace{v_i(\mathbf{x}) - v_i(\mathbf{x})}_{=0} + G_{ij} l_j + \mathcal{O}(l^2) \quad (6.2)$$

²<https://data.4tu.nl/repository/uuid:a64319d5-1735-4bf1-944b-8e9187e4b9d6>

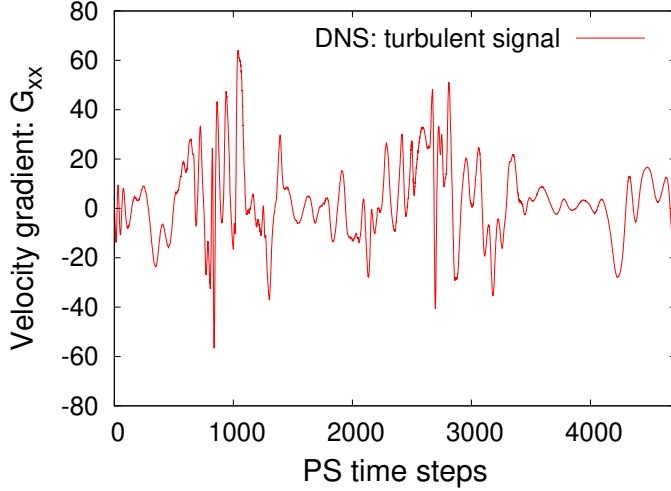


Figure 6.1.: The DNS turbulent signal for the component G_{xx} of the velocity gradient tensor G_{ij} . The data is taken from passive tracer trajectories in a homogeneous isotropic turbulent flow obtained via PS simulations.

for $l \sim R$. Since the droplet's centre of mass remains fixed, i.e. we are in the frame of reference of the droplet, we obtain the following velocity relation in the case of a single phase flow:

$$v_i^{(0)}(\mathbf{x}, t) = G_{ij}(t) x_j \quad (6.3)$$

which is a linear velocity profile in the distance \mathbf{x} from the droplet's centre of mass. With $v_i^{(0)}(\mathbf{x}, t)$ we denote the turbulent velocity profile imposed by the boundary, whereas $v_i(\mathbf{x}, t)$ is the LBM obtained velocity profile given by equation (3.8). Now we test whether our LBM scheme can relax to the imposed velocity field given in equation (6.3).

6.3. Validation results

Now that we have established the approximations we make to the velocity profile on the sub-Kolmogorov scale, see equation (6.3), we would like to create a pseudo-spectral LBM hybrid method, which takes the turbulent velocity gradients $G_{ij}(t)$ as an input. In order for the LBM model to yield accurate predictions, we need to simulate a fully developed turbulent flow at the

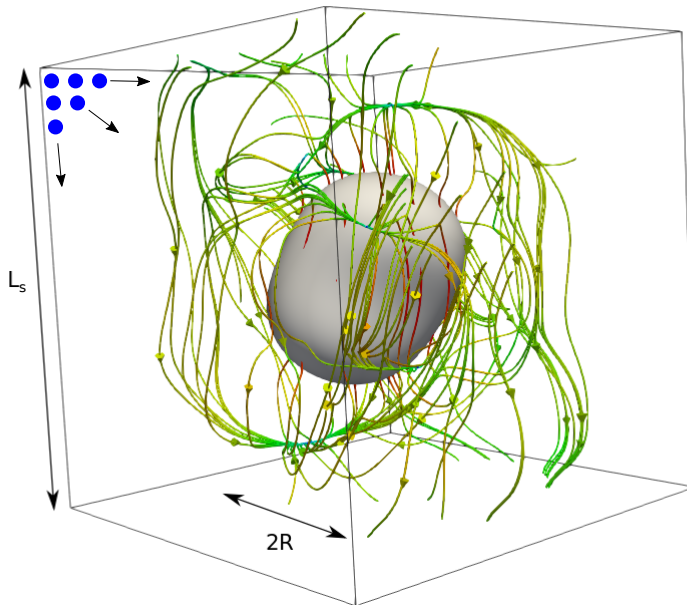


Figure 6.2.: LBM simulation set up: the droplet of scale R in the simulation domain with dimensions $L_s \times L_s \times L_s$. The turbulent flow is initialised at the boundary nodes and visualised via streamlines coloured according to the velocity magnitude $\|\mathbf{v}\|$. The blue dots indicate the ghost nodes, which are crucial in coupling the pseudo-spectral turbulent flow data to the LBM simulation.

domain boundaries, which then evolves into the centre of the domain. This is achieved by using both the ghost node boundary flow scheme described in section 3.5, which stores suitable equilibrium distribution functions on ghost nodes, and the pseudo-spectral values for $G_{ij}(t)$. The simulation set up is shown in figure 6.2 with the length of the simulation box L_s and the diameter of the undeformed droplet $2R$ highlighted.

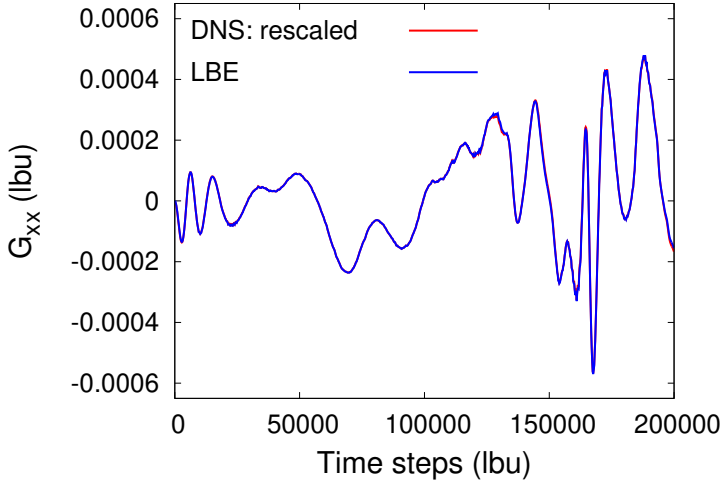


Figure 6.3.: Comparison between the velocity gradient of the pseudo-spectral code and the LBM code after rescaling. Since, both curves, the DNS turbulent input data and the LBM reproduced G_{xx} , overlap, LBM is able to qualitatively reproduce the turbulent velocity gradient.

with the time evolution of the flow completely determined via the turbulent velocity gradient tensor $G_{ij}(t)$. Now we test the convergence of the LBM algorithm for the single phase, where we need to recover the linear profile of the turbulent flow field, see equation (6.3), to a given accuracy. Thus, recovering the velocity field in equation (6.3) effectively means recovering the turbulent velocity gradient $G_{ij}(t)$ of the pseudo-spectral DNS simulations, as the velocity profile is linear. We choose an LBM sampling time Δt measured in lbu, which allows the LBM algorithm to relax to the velocity value required by equation (6.3). In figure 6.3, we see that our LBM scheme reproduces indeed the turbulent signal $G_{ij}(t)$ we provided it with, since the original rescaled DNS signal for the $G_{xx}(t)$ component converges, with the value for $G_{xx}(t)$ obtained with LBM. The rescaling for $G_{ij}(t)$ is

$$G_{ij}(t) \mapsto \frac{u_{\text{LBM}}}{L_s \|G_{ij}(t)\|_\infty} G_{ij}(t) \quad (6.4)$$

where $\|\dots\|_\infty$ denotes the maximum norm and u_{LBM} is a typical LBM velocity scale for which the Mach number $\text{Ma} \leq 0.1$. In order to choose the parameter Δt we need to check the global convergence of the LBM velocity field $\mathbf{v}(\mathbf{x}, t)$ with the one imposed at the boundary, see equation (6.3). The corresponding L_2 -error is provided in figure 6.4 and is defined via:

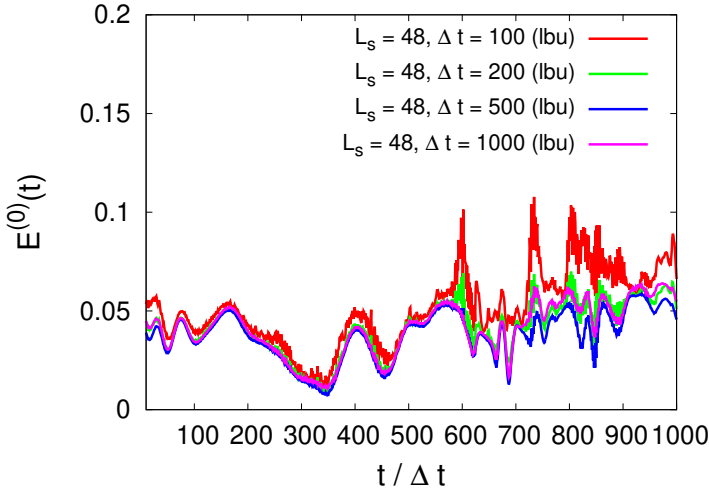


Figure 6.4.: Convergence of the time dependent LBM boundary scheme for a single phase homogeneous and isotropic turbulent flow (domain size: $48 \times 48 \times 48$). The time averaged global error can be estimated to be about $\langle E^{(0)}(t) \rangle_t \sim 0.05$ for a chosen range of Δt in terms of LBM time steps t (in lbu).

$$E^{(0)}(t) = \frac{1}{u_{\text{rms}}^{(0)}(t)} \left[\frac{1}{L_s^3} \int_0^{L_s} dx \int_0^{L_s} dy \int_0^{L_s} dz (\mathbf{v}(x, y, z, t) - \mathbf{v}^{(0)}(x, y, z, t))^2 \right]^{\frac{1}{2}} \quad (6.5)$$

where $\mathbf{v}(x, y, z, t)$ and $\mathbf{v}^{(0)}(x, y, z, t)$ are the velocity fields of the LBM simulation and the imposed turbulent linear velocity profile respectively. $u_{\text{rms}}^{(0)}(t)$ is the rms value of $\mathbf{v}^{(0)}(x, y, z, t)$. Since we would like to choose a minimal Δt , as to optimise run time, we choose $\Delta t = 200$ (lbu), since this value yields a time averaged global error of $\langle E^{(0)}(t) \rangle_t < 0.1$. This is a

reasonable error threshold, since LBM simulations for droplet dynamics in oscillatory shear flows in chapter 4 yield a similar maximal error [74].

6.4. Conclusion

We have shown that similar to previous LBM flow boundary conditions [101, 102] the LBM ghost node boundary flow method, see section 3.5, in conjunction with pseudo-spectral turbulent flow data is able to reproduce temporal turbulent velocity profiles. The algorithm is only suited for droplets on the sub-Kolmogorov scale, where the linear profile of equation (6.3) is valid. The turbulent gradient data is rescaled in order to adapt to varying domain sizes and to respect the Mach number limit of LBM simulations of incompressible flows, i.e. $Ma \leq 0.1$. Consequently, droplet dynamics and breakup can be modelled fully resolved on the sub-Kolmogorov scale, which we will explore in chapter 7.

7. Dynamics and breakup of a sub-Kolmogorov droplet in HIT

This chapter ¹ deals with the dynamics and breakup of the sub-Kolmogorov droplet in homogeneous and isotropic turbulence. We employ the ghost node boundary flow method of chapter 3 and use pseudo-spectral data of turbulent passive tracer trajectories to simulate a fully developed turbulent flow field, as outlined in chapter 6. Now we deal with a multicomponent flow once again, where we place ourselves in the frame of reference of the droplet, i.e. the droplet remains fixed at the centre of the simulation domain and the solvent flow is simulated around it. We investigate breakup predictions for several pseudo-spectral turbulent flow fields via the MM-model and compare the results to the DNS-LBM hybrid method.

7.1. Introduction

The dynamics and breakup behaviour of immiscible droplets in laminar flows have been studied extensively in the literature [25,26,29,37,46,103,105]. Less is known about the dynamics of droplets in homogeneous isotropic turbulent flows, which pose the challenge of solving a multi-physics problem, since the flow properties of the turbulent scales have to be accurately transferred to the scale of the droplet [12,13]. Furthermore, the dynamics and breakup statistics of sub-Kolmogorov droplets have also been studied extensively [15,17,18], which is of particular interest, since the viscous stresses dominate over the inertial stresses, if the droplet size is smaller than the Kolmogorov scale of the outer flow [14]. Both [17] and [18] make use of the MM-model [16] to describe droplet dynamics in homogeneous and isotropic turbulence, which only accounts for ellipsoidal deformations and thus can model breakup only via a cut off criteria. Our studies differ in such a way that we not only use the

¹In preparation as: Milan, F., Sbragaglia, M., Biferale, L., Toschi, F., *Sub-Kolmogorov droplet dynamics in isotropic turbulence using a multiscale Lattice Boltzmann scheme*

MM-model to measure the deformation of the droplet, but compare it with fully resolved LBM simulations using the SCMC diffuse interface method [77, 78]. LBM in conjunction with SCMC has been extensively used in the field of microfluidics and droplet breakup [12, 55, 83–90] making it a well suited tool to predict breakup behaviour with high accuracy. Our numerical method can be seen as a new hybrid approach to the sub-Kolmogorov droplet dynamics: The simulation domain is of the order of the size of the droplet and the surrounding turbulent flow is used as an input via an open boundary condition method [74], similar to [101, 102]. This enables us to study the deformation and breakup behaviour of a sub-Kolmogorov droplet in fully developed isotropic turbulence, which we can compare to the results obtained via the widely used MM-model.

7.2. Flow behaviour of the sub-Kolmogorov droplet

Chapter 6 described the outline of a hybrid DNS-LBM algorithm to simulate a turbulent solvent flow for droplets on the sub-Kolmogorov scale. Moreover, we have explained in section 2.4, that the local Reynolds number $Re < 1$ on the sub-Kolmogorov scale, even though the Taylor Reynolds number Re_λ may be several magnitudes larger, see equation (2.34). Consequently, we are very close to the Stokes limit of $Re \rightarrow 0$ and may neglect inertial effects. Thus, we can make use of a relation of Stokesian suspension dynamics [130]: the velocity field $\mathbf{v}^{(0)}(\mathbf{x}, t)$ of the undisturbed flow is combined with the velocity field of the suspended particle $\mathbf{v}_d(\mathbf{x}, t)$, in our case a deformable droplet, to yield the actual velocity of the flow ²:

$$\mathbf{v}_a(\mathbf{x}, t) = \mathbf{v}^{(0)}(\mathbf{x}, t) + \mathbf{v}_d(\mathbf{x}, t) \quad (7.1)$$

In case of a weakly deformed, almost spherical droplet, the only possible motion of the suspended particle would be rotation, as translation is ruled out in our simulations, see chapter 6. A spherical droplet rotating with angular velocity $\boldsymbol{\omega}_d(t)$ would then modify the flow field by [130]

$$\mathbf{v}_d(\mathbf{x}, t) = \boldsymbol{\omega}_d(t) \times \mathbf{x} \left(\frac{R}{|\mathbf{x}|} \right)^3 \quad (7.2)$$

²The equations are modified to include an explicit time dependency for the flow.

where $|\mathbf{x}| = \sqrt{\mathbf{x} \cdot \mathbf{x}}$, with \mathbf{x} being the distance vector from the droplet's centre of mass. The actual velocity field is then given by

$$\mathbf{v}_a(\mathbf{x}, t) = \mathbf{v}^{(0)}(\mathbf{x}, t) + \boldsymbol{\omega}_d(t) \times \mathbf{x} \left(\frac{R}{|\mathbf{x}|} \right)^3 \quad (7.3)$$

Although equation (7.3) seems like it is of great use to the study of sub-Kolmogorov droplets in homogeneous and isotropic turbulence [131], it should be stressed, that it is only valid for weakly deformed droplets, whose motion is purely restricted to rotation. Therefore, we do not use equation (7.3) in our droplet simulations in the next chapter, where we deal with large amplitude deformations and breakup.

7.3. Breakup predictions: LBM vs MM

Since we have established the validity of the hybrid PS-LBM algorithm in chapter 6, we can investigate droplet dynamics and breakup for a single droplet on the sub-Kolmogorov scale. Analogously to equation (2.8) we can define a measure for the deformation D_{LBM} for our LBM simulations:

$$D_{\text{LBM}}(t) = \sqrt{1 - \frac{\Omega_0(t)}{\Omega(t)}} \quad (7.4)$$

where $\Omega(t)$ is the time-dependent surface area of the deformed droplet and $\Omega_0(t)$ is the surface area of an undeformed spherical droplet of the same volume as the deformed droplet. $D_{\text{LBM}}(t)$ represents a bounded measure for droplet deformation, because $D_{\text{LBM}}(t) = 0$, in case of minimal deformation, for which $\Omega(t) = \Omega_0(t)$, and $D_{\text{LBM}}(t) \rightarrow 1$ for $\Omega(t) \rightarrow \infty$ in case of a hypothetically arbitrary large surface area $\Omega(t)$. It should be noted that $D_{\text{LBM}}(t)$ scales with the droplet length $L(t)$, see chapter Chapter 5, for elongated droplets and thus $D_{\text{LBM}}(t) \sim D$, where D is the droplet deformation according to major and minor ellipsoidal axes, see equation (2.8). We start our simulations by small amplitude deformations, so that the droplet is only ellipsoidally deformed, for which we expect the LBM and MM-model results to match, see figure 7.2. As we can see from figure 7.1, this is indeed the case, because both predictions for the deformation D , LBM and the MM-model, coincide for a maximum capillary number $\text{Ca}_{\text{max}} \ll \text{Ca}_{\text{cr}}$. Figure 7.1 shows the deformation curves for five separate turbulent flows predicted by the

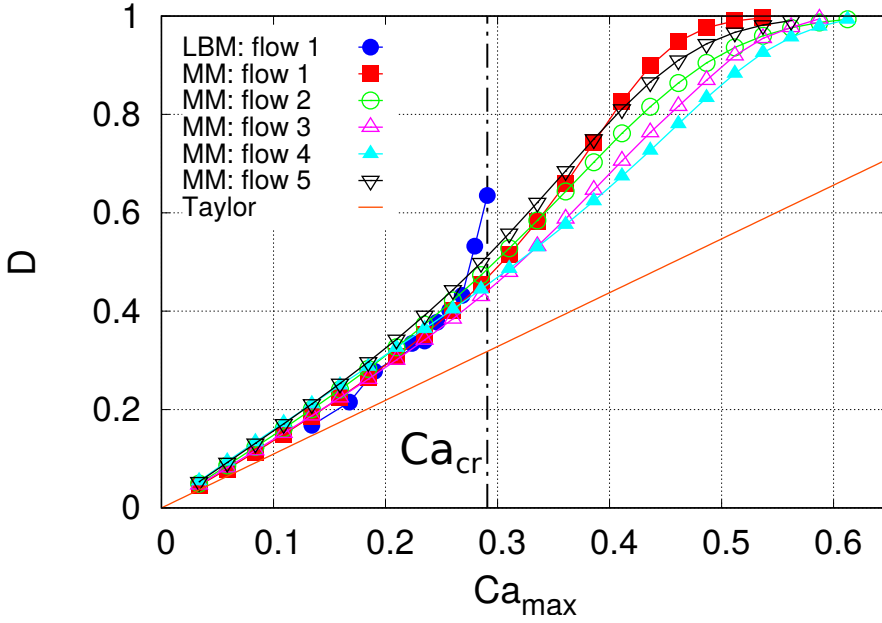


Figure 7.1.: MM-model predictions for the ellipsoidal droplet deformation D as a function of Ca_{\max} for various turbulent flows. The critical capillary number Ca_{cr} is estimated via a cut off for D in the MM-model. The Taylor deformation law, see equation (2.9), is shown for comparison in the low Ca_{\max} limit. We can see that the LBM results coincide with the one of the MM-model, up until a maximum capillary number $Ca_{\max} \approx 0.291$, where the droplet is no longer ellipsoidally deformed, which causes the deviations from the MM-model predictions, see figures 7.3 and 7.4. The critical capillary number obtained via LBM is $Ca_{cr} = 0.286 \pm 0.006$, which is lower than the one predicted in the MM-model, which is lies in the range $Ca_{cr}^{MM} = 0.58 \pm 0.05$. Therefore, it appears that the MM-model is not able to predict the correct critical capillary number Ca_{cr} for sub-Kolmogorov droplet breakup.

MM-model and one produced via the hybrid DNS-LBM simulations. We have chosen five different turbulent flows for the MM-model predictions to account for the irregularity of turbulence. The MM-model deformation curves and the LBM curve collapse for the intermediate range of Ca_{\max} until breakup occurs for the LBM curve at around $Ca_{\max} \approx 0.291$, see figures 7.3 and 7.4. Figure 7.3 shows the elongated droplet for a maximal capillary number $Ca_{\max} \approx Ca_{\text{cr}}$, just before and after breakup. Interestingly, the droplet is now elongated in a similar way to the one in figure 5.1. Figure 7.4 shows the same droplet breakup as figure 7.4 with the velocity field shown via streamlines. We can see that the turbulent flow possesses a significant rotational part in the instance of the breakup. Let us consider the deformation diagram of figure 7.1 again: LBM and the MM-model predict two very different ranges for the critical capillary number Ca_{cr} . Firstly, this is due to the fact, that breakup in the MM-model is determined via a cut off in the deformation D , as the model does not account for a breakup mechanism per se. Secondly, the MM-model can only model ellipsoidally deformed droplets, even in the case of large amplitude flows. Therefore, the MM-model is unable to model the elongated droplet of the DNS-LBM hybrid simulations, shown in figure 7.3, and thus cannot give a very accurate prediction for the critical capillary number Ca_{cr} . The MM-model prediction for the critical capillary number is $Ca_{\text{cr}}^{\text{MM}} = 0.58 \pm 0.05$, where the error has been estimated via the spread of the MM deformation curves in figure 7.1. LBM predicts a lower range of $Ca_{\text{cr}} = 0.286 \pm 0.006$, which is more accurate due to the fully resolved LBM SCMC model, even though the error might be larger, if more turbulent flow trajectories were considered, as has been the case for the MM-model in figure 7.1. The LBM error in Ca_{cr} is estimated via a step in the maximal critical capillary number $\Delta Ca_{\max} \approx 0.011$. ΔCa_{\max} represents the change in capillary number between individual data points in figure 7.1.

7.4. Conclusion

The DNS-LBM hybrid scheme for sub-Kolmogorov droplets in fully developed homogeneous and isotropic turbulence has been used to model droplet deformation and breakup. The LBM results were also compared to MM-model predictions of droplet deformation and breakup. We have found that LBM predicts a significantly lower critical capillary number Ca_{cr} than the

MM-model, see figure 7.1. The reason for this is probably two-fold: firstly breakup is chosen via a cut off procedure for the deformation parameter D in the MM-model and secondly the droplet is far from an ellipsoidal shape in the region of maximum capillary numbers $Ca_{\max} \leq Ca_{\text{cr}}$, see figures 7.3 and 7.4. This suggests, that even though the MM-model and DNS-LBM predictions agree very well in the capillary number region $Ca_{\max} \ll Ca_{\text{cr}}$, accurate predictions of sub-Kolmogorov droplet breakup can only be carried out via fully resolved simulations, such as the DNS-LBM hybrid algorithm, instead of phenomenological models such as the MM-model [17, 18]. It would be interesting to investigate droplet deformation statistics of Sub-Kolmogorov droplets with the DNS-LBM hybrid algorithm and once again use the MM-model for comparison [17, 18]. In addition, it would be interesting to see the range of critical capillary numbers Ca_{cr} predicted by the DNS-LBM hybrid model by extending the LBM results of droplet breakup in figure 7.1 for various turbulent flow fields. Finally, a further extension would be the addition of the velocity field modification outlined in equation (7.3) for weakly deformed rotating sub-Kolmogorov droplets.

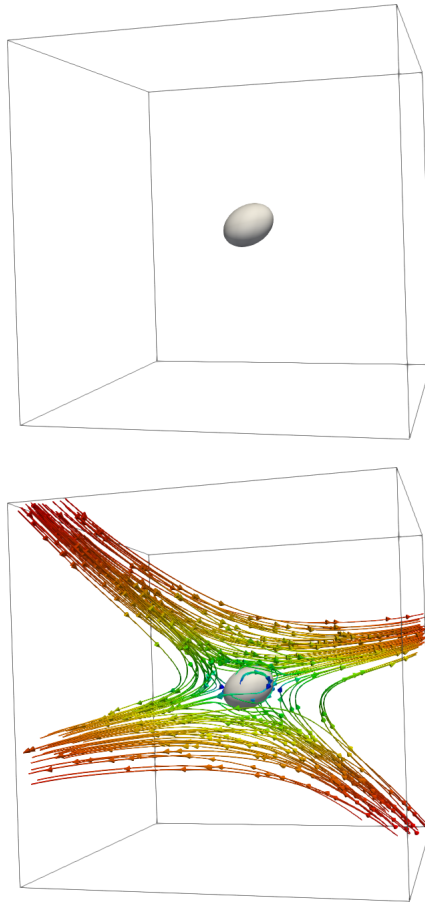


Figure 7.2.: Sub-Kolmogorov droplet for a capillary number $Ca_{\max} \ll Ca_{cr}$ with and without the velocity field shown via streamlines. The droplet is ellipsoidally deformed, which is the regime where LBM and MM predictions coincide.

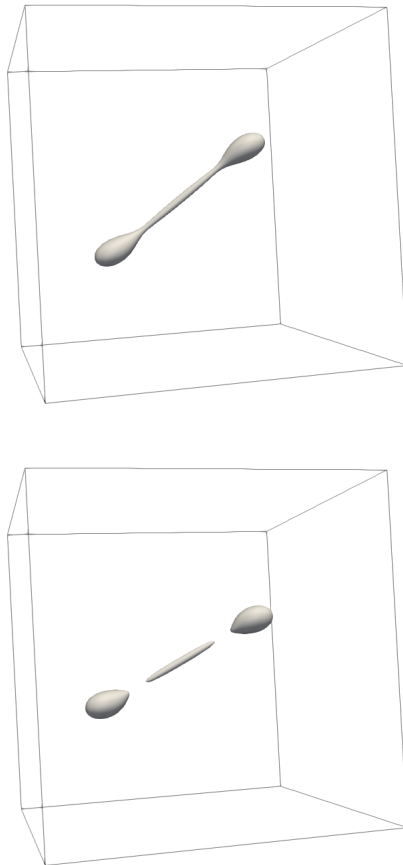


Figure 7.3.: Sub-Kolmogorov droplet for a capillary number $Ca_{\max} \approx Ca_{cr}$ before and after breakup. The elongated droplet shape indicates that substantial deviations from the MM-model predictions might be possible.

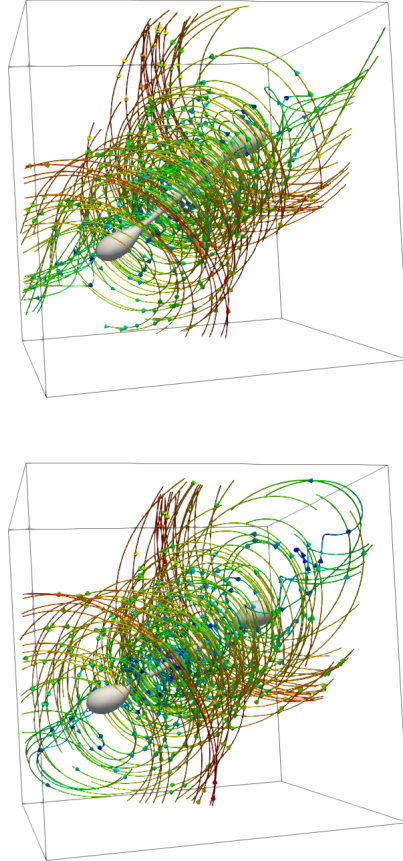


Figure 7.4.: Sub-Kolmogorov droplet with the velocity field indicated via streamlines for a capillary number $Ca_{\max} \approx Ca_{cr}$ before and after breakup. We see that the elongated shape of the droplet is due to both a strong strain and rotational part in the turbulent flow field at this time instance.

8. Conclusion and outlook

The main two goals of this thesis were droplet dynamics and breakup in confined time-dependent laminar flows and the development of a DNS-LBM hybrid algorithm to study sub-Kolmogorov droplet deformation and breakup in homogeneous isotropic turbulent flows. We will summarise and explain the results of those two goals in the following sections.

8.1. Droplets in laminar time-dependent flows

As was mentioned in the introduction, first attempts to model droplet deformation, both in unconfined [19–21] and confined systems [39, 40], are based on the Stokes flow equations, see equation (2.4). Thus, we tested the ghost boundary flow algorithm of section 3.5 for flows close to the Stokes limit, with a simple time-dependence added to the flow in the form of an oscillatory shear rate, see chapter 4. We have tested the validity of the ghost boundary flow algorithm for a simple single phase time-dependent flow problem, a flow created by an oscillating moving wall in an infinitely long channel [91]. After reproducing the exact solution given in [91] with LBM, we analysed the deformation of a single droplet in the channel flow, with two oscillating walls, now producing a time-dependent shear rate. The LBM results were tested with predictions of the MM-model [16, 41, 42] and that of a linearised MM-model [73]. Moreover, we investigated the “transparency effect”, which occurs for a specific choice of the oscillation shear frequency in relation to the droplet’s relaxation time. In chapter 5 we investigated large scale droplet deformation and breakup of a confined droplet in an oscillatory shear flow. A striking question which arose, was the reason for a mismatch between two different flow start up protocols, the “shock method” and the “relaxation method”. This led us to investigate the dependency of this mismatch on inertia [46, 69], degree of confinement [28] and flow topology [67, 68]. We concluded, that the reason for the mismatch was due to a high degree of confinement, $\alpha \geq 0.75$ and would disappear under the

influence of small scale flow perturbations, such as the time-dependency of an oscillatory shear flow. After having investigated rather interesting cases of time-dependency effects in laminar multicomponent flows, we moved to the turbulent regime to analyse the dynamics of sub-Kolmogorov droplets.

8.2. Sub-Kolmogorov droplets in turbulent flows

Before starting our investigation of sub-Kolmogorov droplets in homogeneous isotropic turbulent flows, we outlined the structure of the ghost node boundary flow algorithm of section 3.5 for the use in HIT on the sub-Kolmogorov scale in chapter 6 and compared it briefly to other exact boundary flow algorithms [100–102] and hybrid methods [127–129]. We explained the way the pseudo-spectral data of passive tracer trajectories in HIT was used to mimic an exact flow at the LBM simulation domain boundary and showed that we can reproduce the turbulent flow in single phase LBM simulations with the newly developed DNS-LBM hybrid scheme. Eventually, chapter 7 saw the DNS-LBM hybrid method of chapter 6 be put to use. Firstly, we mentioned that sub-Kolmogorov droplet dynamics are challenging to analyse in a variety of settings [14, 15] and that the MM-model is the method of choice to model droplets in HIT [17, 18]. However, we have demonstrated that the fully resolved DNS-LBM hybrid method and the MM-model yield different results for large amplitude sub-Kolmogorov droplet deformation and break up. Therefore, we may conclude that, one should prefer the DNS-LBM hybrid simulations over the MM-model, if accurate predictions about breakup on the sub-Kolmogorov scale are essential.

8.3. Outlook

This work on droplet dynamics in time-dependent and turbulent flows has led to many interesting questions to be answered along the way. Firstly, the protocol mismatch in chapter 5 has never been observed in the literature before. It would be interesting to see, if an experimental setup with a sufficiently isolated and stable shear flow and smooth flow startup conditions was able to reproduce the protocol mismatch. Furthermore, a detailed comparison of sub-Kolmogorov droplet dynamics statistics using the DNS-LBM hybrid scheme vs the MM-model would be of interest as well, in addition with further DNS-LBM breakup statistics for the results shown in figure 7.1.

A further extension of the work could be to modify the velocity field in the DNS-LBM hybrid setup according to equation 7.3 for weakly deformed sub-Kolmogorov droplets.

A. Numerical solution of the MM-model

The droplet deformation equation of the MM-model [16], given in equation (2.13), is a non-linear equation in the droplet deformation tensor M_{ij} and was thus solved numerically. We will briefly outline the numerical solver used for the MM-model in this chapter and discuss its validation tests for different solvent flows, for which analytical solutions of the MM-model of [16] are used. Before we start to discretising the MM-model equation (2.13), we perform a non-dimensionalisation

$$\frac{dM_{ij}}{dt'} = [f_2(S'_{ik}M_{kj} + M_{ik}S'_{kj}) + \Omega'_{ik}M_{kj} - M_{ik}\Omega'_{kj}] - \frac{f_1}{\text{Ca}} \left(M_{ij} - 3\frac{III_M}{II_M}\delta_{ij} \right) \quad (\text{A.1})$$

where we have rescaled the shear tensor with the shear rate G , so that $S'_{ij} = S_{ij}/G$, $\Omega'_{ij} = \Omega_{ij}/G$ and $t' = t/G$. The constants f_1 and f_2 of the rescaled MM equation (A.1) are given by

$$f_1(\chi) = \frac{40(\chi + 1)}{(2\chi + 3)(19\chi + 16)} \quad (\text{A.2})$$

$$f_2(\chi) = \frac{5}{2\chi + 3} \quad (\text{A.3})$$

where f_1 and f_2 are solely dependent on the viscous ratio χ ¹. The rescaled Maffettone-Minale equation (A.1) is tested for three specific shear flows in [16]. We would like to validate those cases numerically with a Runge-Kutta 4 (RK4) integration scheme. In order to solve equation (A.1) with the

¹The corresponding values for MM-unbounded in equation (2.16) differ from the values given in equation (A.2) via corrective terms in the capillary number Ca . Even though the parameters of equation (2.16) increase the accuracy of the model, the analytical solutions of the MM-model in this chapter use the non-corrective parameters given in equation (A.2)

parameters given in equation (A.2), we consider an RK4 scheme for a first order dynamical differential equation $\dot{x} = f(x, t)$, where the n -th timestep is given by [132]

$$k_1 = f(x_n, t_n) \quad (\text{A.4})$$

$$k_2 = f\left(t_n + \frac{\Delta t}{2}, x_n + \frac{k_1}{2}\right) \quad (\text{A.5})$$

$$k_3 = f\left(t_n + \frac{\Delta t}{2}, x_n + \frac{k_2}{2}\right) \quad (\text{A.6})$$

$$k_4 = f\left(t_n + \Delta t, x_n + k_3\right) \quad (\text{A.7})$$

$$x_{n+1} = x_n + \frac{\Delta t}{6} \left(k_1 + 2k_2 + 2k_3 + k_4\right) + \mathcal{O}(\Delta t^5) \quad (\text{A.8})$$

with Δt being the discrete time step for the RK4 numerical integrator. With the help of this solver we can obtain a numerical value of the droplet deformation parameter D via the time evolution of the morphology tensor given in equation (A.1). We will apply three different types of solvent flows to the MM-model equation (A.1) in the following sections and compare the solution of the RK4 numerical solver to the analytical solutions provided by [16].

A.1. Simple shear flow

At first let us consider a simple shear flow with strain rate

$$S'_{ij} = \frac{1}{2} \begin{pmatrix} 0 & 1 & 0 \\ 1 & 0 & 0 \\ 0 & 0 & 0 \end{pmatrix} \quad (\text{A.9})$$

and rotation

$$\Omega'_{ij} = \frac{1}{2} \begin{pmatrix} 0 & 1 & 0 \\ -1 & 0 & 0 \\ 0 & 0 & 0 \end{pmatrix} \quad (\text{A.10})$$

According to [16] the steady-state values for the semi-axes of the ellipsoid are given by

$$L^2 = \frac{f_1^2 + Ca^2 + f_2Ca\sqrt{f_1^2 + Ca^2}}{(f_1^2 + Ca^2)^{\frac{1}{3}}(f_1^2 + Ca^2 - f_2^2Ca^2)^{\frac{2}{3}}} \quad (\text{A.11})$$

$$B^2 = \frac{f_1^2 + Ca^2 - f_2Ca\sqrt{f_1^2 + Ca^2}}{(f_1^2 + Ca^2)^{\frac{1}{3}}(f_1^2 + Ca^2 - f_2^2Ca^2)^{\frac{2}{3}}} \quad (\text{A.12})$$

$$W^2 = \frac{f_1^2 + Ca^2 - f_2^2Ca^2}{(f_1^2 + Ca^2)^{\frac{1}{3}}(f_1^2 + Ca^2 - f_2^2Ca^2)^{\frac{2}{3}}} \quad (\text{A.13})$$

yielding a deformation parameter of

$$D_{\text{shear}} = \frac{\sqrt{f_1^2 + Ca^2} - \sqrt{f_1^2 + Ca^2 - f_2^2Ca^2}}{f_2Ca} \quad (\text{A.14})$$

A.2. Uniaxial extensional flow

Secondly we check the model against a uniaxial extensional flow [16] with strain

$$S'_{ij} = \frac{1}{2} \begin{pmatrix} 2 & 0 & 0 \\ 0 & -1 & 0 \\ 0 & 0 & -1 \end{pmatrix} \quad (\text{A.15})$$

and an identically vanishing rotation

$$\Omega'_{ij} = 0 \quad (\text{A.16})$$

with semi-axes

$$L^2 = \left(\frac{f_1 + f_2Ca}{f_1 - 2f_2Ca} \right)^{\frac{2}{3}} \quad (\text{A.17})$$

$$B^2 = W^2 = \left(\frac{f_1 - 2f_2Ca}{f_1 + f_2Ca} \right)^{\frac{1}{3}} \quad (\text{A.18})$$

giving a deformation parameter

$$D_{\text{uniaxial}} = \frac{2f_1 - f_2Ca - 2\sqrt{(f_1 + f_2Ca)(f_1 - 2f_2Ca)}}{3f_2Ca} \quad (\text{A.19})$$

A.3. Planar hyperbolic flow

At last we test the MM-model for a planar hyperbolic flow

$$S'_{ij} = \begin{pmatrix} 1 & 0 & 0 \\ 0 & -1 & 0 \\ 0 & 0 & 0 \end{pmatrix} \quad (\text{A.20})$$

and an identically vanishing rotation

$$\Omega'_{ij} = 0 \quad (\text{A.21})$$

with semi-axes

$$L^2 = \frac{(f_1^2 + 2f_1f_2Ca)^{\frac{1}{3}}}{(f_1 - 2f_2Ca)^{\frac{2}{3}}} \quad (\text{A.22})$$

$$B^2 = \frac{(f_1^2 - 2f_1f_2Ca)^{\frac{1}{3}}}{(f_1 + 2f_2Ca)^{\frac{2}{3}}} \quad (\text{A.23})$$

$$W^2 = \frac{(f_1^2 - 4f_2^2Ca^2)^{\frac{1}{3}}}{f_1^{\frac{2}{3}}} \quad (\text{A.24})$$

and a deformation parameter

$$D_{\text{planar}} = \frac{f_1 - \sqrt{f_1^2 - 4f_2^2Ca^2}}{2f_2Ca} \quad (\text{A.25})$$

The corresponding numerical validation tests are given in figure A.1, from which we can see that the numerical solver is able to accurately reproduce the analytical solutions to the three different types of flow fields for various viscosity ratios χ .

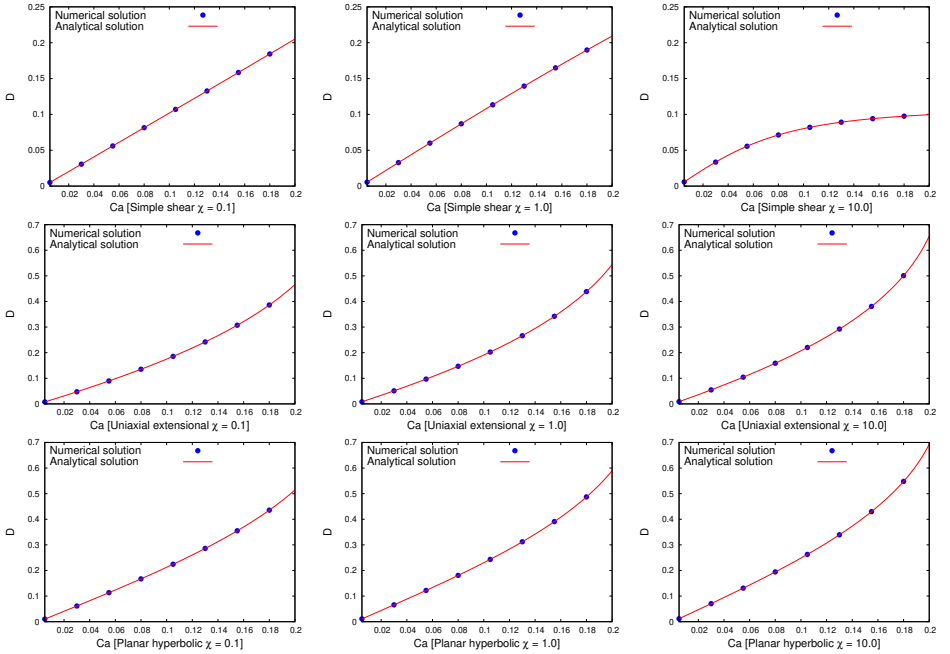


Figure A.1.: Numerical validation of the numerical RK4 solver for the MM deformation equation (A.1), for simple shear, uniaxial extensional and planar hyperbolic flows.

B. A linearised MM-model solution for an oscillatory shear flow

In chapter 4 we investigated the deformation of a single confined droplet in an oscillatory shear flow. We performed LBM simulations and compared their results to both a numerical and a perturbative solution of the MM-model. This chapter gives a brief outline of the ideas behind the linearised perturbative MM-model used during the discussion in chapter 4. The morphology tensor M_{ij} in the MM-model equation (4.11) may be expressed in a perturbation series in the time-dependent capillary number $\text{Ca}(t)$ [73]:

$$M_{ij}(t) = \delta_{ij} + \text{Ca}(t)M_{ij}^{(1)}(t) + \mathcal{O}(\text{Ca}^2(t)) \quad (\text{B.1})$$

where $M_{ij}^{(1)}(t)$ denotes a first order correction to the morphology tensor of an undeformed droplet δ_{ij} and the time t is given in units of the droplet relaxation time t_d . The time evolution of the capillary number is determined via the oscillatory shear rate, which we can express in complex form as

$$\text{Ca}(t) = i\text{Ca}_{\max}e^{i\omega t_d t} \quad (\text{B.2})$$

Using the relations in equations (B.1) and (B.2) and the initial condition $M_{ij}^{(1)}(0) = 0$, we obtain an evolution equation for the first order off-diagonal elements of $M_{ij}^{(1)}(t)$:

$$\frac{dM_{xz}^{(1)}(t)}{dt} = f_2 - (f_1 + i\omega t_d)M_{xz}^{(1)}(t) + \mathcal{O}(\text{Ca}^2(t)) \quad (\text{B.3})$$

where $M_{xz}^{(1)}(t) \sim \text{Ca}(t)$ is the off-diagonal element of M_{ij} in accordance with the applied shear in the x-z-plane, see figure 4.3. The solution to equation (B.3) is then given by

$$M_{xz}^{(1)}(t) = \frac{f_2(1 - e^{-f_1 t - i\omega t_d t})}{f_1 + i\omega t_d} + \mathcal{O}(\text{Ca}^2(t)) \quad (\text{B.4})$$

from which we can diagonalise the linearised morphology tensor $M_{ij}(t)$ to obtain up to first order in the maximal capillary number Ca_{\max} the complex eigenvalues \hat{L}_c^2 , \hat{W}_c^2 and \hat{B}_c^2 of $M_{ij}(t)$:

$$\begin{aligned}\hat{L}_c^2 &= 1 + \text{Ca}_{\max} f_2 \left(\frac{e^{i\omega t_d t} - e^{-f_1 t}}{\omega t_d - i f_1} \right) + \mathcal{O}(\text{Ca}_{\max}^2) \\ \hat{W}_c^2 &= 1 - \text{Ca}_{\max} f_2 \left(\frac{e^{i\omega t_d t} - e^{-f_1 t}}{\omega t_d - i f_1} \right) + \mathcal{O}(\text{Ca}_{\max}^2) \\ \hat{B}_c^2 &= 1 + \mathcal{O}(\text{Ca}_{\max}^2)\end{aligned}\tag{B.5}$$

The transient part $e^{-f_1 t}$ can be ignored for sufficiently large t . After taking the real part of the complex eigenvalues of M_{ij} we obtain the values given in equation (4.12).

Bibliography

- [1] R. W. Flumerfelt. Drop breakup in simple shear fields of viscoelastic fluids. *Industrial & Engineering Chemistry Fundamentals*, 11(3):312–318, 1972.
- [2] M. Singh, M. Haverinen, H., and P. Dhagat. Inkjet printing-process and its applications. *Advanced Functional Materials*, 22:673–685, 2010.
- [3] H. Shewan and J. R. Stokes. Review of techniques to manufacture micro-hydrogel particles for the food industry and their applications. *Journal of Food Engineering*, 119:781–792, 2013.
- [4] J. Rodriguez-Rodriguez, A. Sevilla, C. Martinez-Bazan, and J. M. Gordillo. Generation of microbubbles with applications to industry and medicine. *Annu. Rev. Fluid Mech.*, 47:405–429, 2015.
- [5] H. Tennekes and J. L. Lumley. *A First Course in Turbulence*. The MIT Press, 1st edition, 1972.
- [6] U. Frisch. *Turbulence: the legacy of A. N. Kolmogorov*. Cambridge University Press, 1st edition, 1995.
- [7] S. B. Pope. *Turbulent Flows*. Cambridge University Press, 1st edition, 2000.
- [8] P. A. Davidson. *Turbulence: An Introduction for Scientists and Engineers*. Oxford University Press, 2nd edition, 2015.
- [9] O. Hinze. Fundamentals of the hydrodynamic mechanism of splitting in dispersion processes. *AIChE J.*, 1:289–295, 1955.
- [10] J. C. Lasheras, C. Eastwood, C. Martínez-Bazán, and J. L. Montañes. A review of statistical models for the breakup of an immiscible fluid immersed into a fully-developed turbulent flow. *International Journal of Multiphase Flow*, 28:247–278, 2004.

- [11] L. Biferale, P. Perlekar, M. Sbragaglia, S. Srivastava, and F. Toschi. A lattice boltzmann method for turbulent emulsions. *J. Phys.: Conf. Ser.*, 318:052017, 2011.
- [12] A. E. Komrakovaa, O. Shardt, D. Eskinb, and J. J. Derksen. Lattice Boltzmann simulations of drop deformation and breakup in shear flow. *International Journal of Multiphase Flow*, 59:23–43, 2014.
- [13] D. O. Njobuenwu and M. Fairweather. Dynamics of single, non-spherical ellipsoidal particles in a turbulent channel flow. *Chemical Engineering Science*, 123:265–282, 2015.
- [14] V. Crsitini, J. Blawdziewicz, M. Loewenberg, and L. R. Collins. Breakup in stochastic Stokes flows: sub-Kolmogorov drops in isotropic turbulence. *Journal of Fluid Mechanics*, 492:231–250, 2003.
- [15] V. Spandan, D. Lohse, and R. Verzicco. Deformation and orientation statistics of neutrally buoyant sub-Kolmogorov ellipsoidal droplets in turbulent Taylor-Couette flow. *Journal of Fluid Mechanics*, 809:480–501, 2016.
- [16] P. L. Maffettone and M. Minale. Equation of change for ellipsoidal drops in viscous flow. *J. Non Newton. Fluid Mech*, 78:227–241, 1998.
- [17] L. Biferale, C. Meneveau, and R. Verzicco. Deformation statistics of sub-Kolmogorov-scale ellipsoidal neutrally buoyant drops in isotropic turbulence. *Journal of Fluid Mechanics*, 754:184–207, 2014.
- [18] S. S. Ray and Vincenzi D. Droplets in isotropic turbulence: deformation and breakup statistics. *Journal of Fluid Mechanics*, 852:313–328, 2018.
- [19] G. I. Taylor. The Viscosity of a Fluid Containing Small Drops of Another Fluid. *Proceedings of the Royal Society A: Mathematical, Physical and Engineering Sciences*, 138(834):41–48, 1932.
- [20] G. I. Taylor. The formation of emulsion in definable field of flow. *Proc. Royal Soc A*, 146(501-523), 1934.
- [21] F. Greco. Second-order theory for the deformation of a newtonian drop in a stationary flow field. *Physics of Fluids (1994-present)*, 14(3):946–954, 2002.

- [22] I. Fortelny and J. Juza. Description of the droplet size evolution in flowing immiscible polymer blends. *Polymers*, 11(761), 2019.
- [23] A. Acrivos and T.D. Taylor. The Stokes flow past an arbitrary particle. *Chemical Engineering Science*, 19:445–451, 1964.
- [24] J. Lyngaae-Jørgensen and A. Valenza. Structuring of polymer blends in simple shear flow. *Makromolekulare Chemie. Macromolecular Symposia*, 38(43-60), 1990.
- [25] S. Guido and F. Greco. Dynamics of a liquid drop in a flowing immiscible liquid. *Rheology Reviews*, 2:99–142, 2004.
- [26] A. Vananroye, R. Cardinaels, P. van Puyvelde, and P. Moldenaers. Effect of confinement and viscosity ratio on the dynamics of single droplets during transient shear flow. *Journal of Rheology (1978-present)*, 52(6):1459–1475, 2008.
- [27] P. J. A. Janssen and P. D. Anderson. A boundary-integral model for drop deformation between two parallel plates with non-unit viscosity ratio drops. *Journal of Computational Physics*, 227(20):8807–8819, 2008.
- [28] P. J. A. Janssen, A. Vananroye, P. Van Puyvelde, P. Moldenaers, and P. D. Anderson. Generalized behavior of the breakup of viscous drops in confinements. *J. Rheol.*, 54:1047–1060, 2010.
- [29] S. Guido. Shear-induced droplet deformation: Effects of confined geometry and viscoelasticity. *Current Opinion in Colloid & Interface Science*, 16:61–70, 2011.
- [30] P. De Bruyn, R. Cardinaels, and P. Moldenaers. The effect of geometrical confinement on coalescence efficiency of droplet pairs in shear flow. *Journal of Colloid and Interface Science*, 409:183–192, 2013.
- [31] R. Cardinaels, K. Verhulst, and P. Moldenaers. Influence of confinement on the steady state behavior of single droplets in shear flow for immiscible blends with one viscoelastic component. *Journal of Rheology (1978-present)*, 53(6):1403–1424, 2009.

- [32] R. Cardinaels and P. Moldenaers. Droplet relaxation in blends with one viscoelastic component: bulk and confined conditions. *Rheologica acta*, 49(9):941–951, 2010.
- [33] R. Cardinaels and P. Moldenaers. Critical conditions and breakup of non-squashed microconfined droplets: effects of fluid viscoelasticity. *Microfluid Nanofluid*, 10:1153–1163, 2011.
- [34] R. Cardinaels, A. Vananroye, P. Van Puyvelde, and P. Moldenaers. Breakup criteria for confined droplets: effects of compatibilization and component viscoelasticity. *Macromolecular Materials and Engineering*, 296(3-4):214–222, 2011.
- [35] A. Vananroye, P. van Puyvelde, and P. Moldenaers. Effect of confinement on droplet breakup in sheared emulsions. *Langmuir*, 22(9):3972–3974, 2006.
- [36] A. Vananroye, P. van Puyvelde, and P. Moldenaers. Effect of confinement on the steady-state behavior of single droplets during shear flow. *Journal of Rheology (1978-present)*, 51(1):139–153, 2007.
- [37] A. Vananroye, P. van Puyvelde, and P. Moldenaers. Deformation and orientation of single droplets during shear flow: combined effects of confinement and compatibilization. *Rheologica acta*, 50(3):231–242, 2011.
- [38] P. van Puyvelde, A. Vananroye, R. Cardinaels, and P. Moldenaers. Review on morphology development of immiscible blends in confined shear flow. *Polymer*, 49(25):5363–5372, 2008.
- [39] M. Shapira and S. Haber. Low reynolds number motion of a droplet between two parallel plates. *Int J Multiph Flow*, 14:483–506, 1988.
- [40] M. Shapira and S. Haber. Low reynolds-number motion of a droplet in shear flow including wall effects. *Int J Multiph Flow*, 16:305–321, 1990.
- [41] M. Minale. A phenomenological model for wall effects on the deformation of an ellipsoidal drop in viscous flow. *Rheol. Acta*, 47:667–675, 2008.

- [42] M. Minale. Models for the deformation of a single ellipsoidal drop: a review. *Rheol. Acta*, 49:789–806, 2010.
- [43] V. Sibillo, G. Pasquariello, M. Simeone, V. Cristini, and S. Guido. Drop deformation in microconfined shear flow. *Phys. Rev. Lett.*, 97:054502, 2006.
- [44] M. Minale, S. Caserta, and S. Guido. Microconfined shear deformation of a droplet in an equiviscous non-newtonian immiscible fluid: Experiments and modeling. *Langmuir*, 26:126–132, 2010.
- [45] D. Megias-Alguacil, K. Feigl, M. Dressler, Fischer P., and E.J. Windhab. Droplet deformation under simple shear investigated by experiment, numerical simulation and modeling. *Journal of Non-Newtonian Fluid Mechanics*, 126:153–161, 2005.
- [46] Y. Y. Renardy and Vittorio Cristini. Effect of inertia on drop breakup under shear. *Physics of Fluids*, 13(1):7–13, 2001.
- [47] S. Caserta, S. Reynaud, M. Simeone, and S. Guido. Drop deformation in sheared polymer blends. *Journal of Rheology*, 51(6), 2007.
- [48] C. E. Chaffey and H.A. Brenner. A second-order theory for shear deformation of drops. *J Colloid Interface Sci.*, 24:258–269, 1967.
- [49] T. Chinyoka, Y. Y. Renardy, M. Renardy, and Khismatullin D. B. Two-dimensional study of drop deformation under simple shear for Oldroyd-B liquids. *Journal of Non-Newtonian Fluid Mechanics*, 130:45–56, 2005.
- [50] J. J. Elmendorp and R. J. Maalcke. A study on polymer blending microrheology: Part 1. *Polymer Engineering & Science*, 25(16):1041–1047, 1985.
- [51] K. Feigl, S. F. M. Kaufmann, P. Fischer, and E. J. Windhab. A numerical procedure for calculating droplet deformation in dispersing flows and experimental verification. *Chemical Engineering Science*, 58:2351–2363, 2002.
- [52] H. P. Grace. Dispersion phenomena in high viscosity immiscible fluid systems and application of static mixers as dispersion devices in such systems. *Chem. Eng. Commun.*, 14:225–277, 1982.

- [53] J. Li, Y. Y. Renardy, and M. Renardy. Numerical simulation of breakup of a viscous drop in simple shear flow through a volume-of-fluid method. *Physics of Fluids*, 12(2), 2000.
- [54] H. Li and U. Sundararaj. Does drop size affect the mechanism of viscoelastic drop breakup? *Physics of Fluids*, 20, 2008.
- [55] H. Liu, A. J. Valocchi, and Q. Kang. Three-dimensional lattice Boltzmann model for immiscible two-phase flow simulations. *Phys. Rev. E*, 85:046309, 2012.
- [56] F. Mighri, P. J. Carreau, and A. Ajji. Influence of elastic properties on drop deformation and breakup in shear flow. *Journal of Rheology (1978-present)*, 42(6):1477–1490, 1998.
- [57] F. Mighri and M. A. Huneault. In situ visualization of drop deformation, erosion, and breakup in high viscosity ratio polymeric systems under high shearing stress conditions. *Journal of Applied Polymer Science*, 42:25822591, 2006.
- [58] S. Mukherjee and K. Sarkar. Effects of viscosity ratio on deformation of a viscoelastic drop in a newtonian matrix under steady shear. *Journal of Non-Newtonian Fluid Mechanics*, 160(2):104–112, 2009.
- [59] S. B. Pillapakam and P. Singh. A level-set method for computing solutions to viscoelastic two-phase flow. *Journal of Computational Physics*, 174(2):552–578, 2001.
- [60] N. Aggarwal and K. Sarkar. Deformation and breakup of a viscoelastic drop in a newtonian matrix under steady shear. *J. Fluid Mech.*, 584:1–21, 2007.
- [61] N. Aggarwal and K. Sarkar. Effects of matrix viscoelasticity on viscous and viscoelastic drop deformation in a shear flow. *J. Fluid Mech.*, 601:63–84, 2008.
- [62] V. Sibillo, M. Simeone, and S. Guido. Break-up of a newtonian drop in a viscoelastic matrix under simple shear flow. *Rheol Acta*, 43:449–456, 2004.
- [63] C. L. Tucker and P. Moldenaers. Microstructural evolution in polymer blends. *Annual Review of Fluid Mechanics*, 34(1):177–210, 2002.

- [64] X. Zhao. Drop breakup in dilute newtonian emulsions in simple shear flow: New drop breakup mechanisms. *Journal of Rheology*, 51(3):367–392, 2007.
- [65] S. Torza, R. G. Cox, and S. G. Mason. Particle motions in sheared suspensions XXVII. Transient and steady deformation and burst of liquid drops. *J. Colloid Interface Sci.*, 38:395–411, 1972.
- [66] E. J. Hinch and A. Acrivos. Long slender drops in a simple shear flow. *Journal of Fluid Mechanics*, 98(2):305–328, 1980.
- [67] J. F. Brady and A. Acrivos. The deformation and breakup of a slender drop in an extensional flow: inertial effects. *Journal of Fluid Mechanics*, 115:443–451, 1982.
- [68] B. J. Bentley and L. G. Leal. An experimental investigation of drop deformation and breakup in steady two-dimensional linear flows. *J. Fluid Mech.*, 167:241–283, 1986.
- [69] Y. Renardy. Effect of startup conditions on drop breakup under shear with inertia. *Journal of Multiphase Flow*, 34:1185–1189, 2008.
- [70] R. G. Cox. The deformation of a drop in a general time-dependent fluid flow. *Journal of Fluid Mechanics*, 37(3):601–623, 1969.
- [71] A. Farutin and C. Misbah. Rheology of vesicle suspensions under combined steady and oscillating shear flows. *Journal of Fluid Mechanics*, 700:362–381, 2012.
- [72] R. Cavallo, S. Guido, and M. Simeone. Drop deformation under small-amplitude oscillatory shear flow. *Rheol Acta*, 42:1–9, 2002.
- [73] W. Yu, M. Bousmina, M. Grmela, and C. Zhou. Modeling of oscillatory shear flow of emulsions under small and large deformation fields. *Journal of Rheology*, 46(6):1401–1418, 2002.
- [74] F. Milan, M. Sbragaglia, L. Biferale, and F. Toschi. Lattice boltzmann simulations of droplet dynamics in time-dependent flows. *Eur. Phys. J. E*, 41(6), 2018.
- [75] R. Benzi, S. Succi, and M. Vergassola. The lattice Boltzmann equation: Theory and applications. *Physics Reports*, 222:145–197, 1992.

- [76] S. Succi. *The Lattice Boltzmann Equation for Fluid Dynamics and Beyond*. Oxford University Press, 2001.
- [77] X. Shan and H. Chen. Lattice boltzmann model for simulating flows with multiple phases and components. *Physical Review E*, 47(3):1815–1819, 1993.
- [78] X. Shan and H. Chen. Simulation of nonideal gases and liquid-gas phase transitions by the lattice boltzmann equation. *Physical Review E*, 49(4):2941–2948, 1994.
- [79] M. Sbragaglia, R. Benzi, M. Bernaschi, and S. Succi. The emergence of supramolecular forces from lattice kinetic models of non-ideal fluids: applications to the rheology of soft glassy materials. *Soft Matter*, 8:10773–10782, 2012.
- [80] J. Onishi, Y. Chen, and H. Ohashi. A lattice Boltzmann model for polymeric liquids. *Prog. Comp. Fluid Dyn.*, 5:75–84, 2005.
- [81] M. Gross, M. E. Cates, F. Varnik, and R. Adhikari. Langevin theory of fluctuations in the discrete Boltzmann equation. *Journal of Statistical Mechanics: Theory and Experiment*, page P03030, 2011.
- [82] X. Xue, M. Sbragaglia, L. Biferale, and F. Toschi. Effects of thermal fluctuations in the fragmentation of a nanoligament. *Physical Review E*, 98(1):012802, 2018.
- [83] S. Farokhirad, T. Lee, and J. F. Morris. Effects of Inertia and Viscosity on Single Droplet Deformation in Confined Shear Flow. *Commun. Comput. Phys.*, 13(3):706–724, 2013.
- [84] J. Onishi, Y. Chen, and H. Ohashi. Dynamic simulation of multi-component viscoelastic fluids using the lattice Boltzmann method. *Physica A*, 362:84–92, 2006.
- [85] H. Xi and C. Duncan. Lattice Boltzmann simulations of three-dimensional single droplet deformation and breakup under simple shear flow. *Phys. Rev. E*, 59(3):3022–3026, 1999.
- [86] M. Yoshino, Y. Toriumi, and M. Arai. Lattice Boltzmann Simulation of Two-Phase Viscoelastic Fluid Flows. *Journal of Computational Science and Technology*, 2, 2008.

- [87] A. Gupta and M. Sbragaglia. Deformation and breakup of viscoelastic droplets in confined shear flow. *Physical Review E - Statistical, Nonlinear, and Soft Matter Physics*, 90(2):1–17, 2014.
- [88] A. Gupta, M. Sbragaglia, and A. Scagliarini. Hybrid lattice boltzmann/finite difference simulations of viscoelastic multicomponent flows in confined geometries. *Journal of Computational Physics*, 2015.
- [89] D. Chiappini, X. Xue, G. Falcucci, and M. Sbragaglia. Ligament breakup simulation through pseudo-potential lattice boltzmann method. In *AIP Conference Proceedings*, volume 1978, page 420003. AIP Publishing, 2018.
- [90] D. Chiappini, M. Sbragaglia, X. Xue, and G. Falcucci. Hydrodynamic behavior of the pseudopotential lattice boltzmann method for interfacial flows. *Phys. Rev. E*, 99:053305, 2019.
- [91] L. D. Landau and E. M. Lifschitz. *Fluid Mechanics*. Pergamon Press, 2nd edition, 1987.
- [92] H. Goldstein, C. Poole, and J. Safko. *Classical Mechanics*. Pearson, 3rd edition, 2014.
- [93] D. A. Wolf-Gladrow. *Lattice-Gas Cellular Automata and Lattice Boltzmann Models: An Introduction*. Springer Verlag, 2000.
- [94] T. Krüger, H. Kusumaatmaja, A. Kuzmin, O. Shardt, G. Silva, and E. M. Viggien. *The Lattice Boltzmann Method: Principles and Practice*. Springer Verlag, 2017.
- [95] U. D. Schiller. Thermal fluctuations and boundary conditions in the lattice boltzmann method, 2008.
- [96] M. Haussmann, S. Simonis, H. Nirschl, and M. J. Krause. Direct numerical simulation of decaying homogeneous isotropic turbulence numerical experiments on stability, consistency and accuracy of distinct lattice boltzmann methods. *International Journal of Modern Physics C*, page 1950074, 2019.
- [97] D. d’Humières, I. Ginzburg, M. Krafczyk, P. Lallemand, and L.-S. Luo. Multiple-relaxation-time lattice boltzmann models in three dimensions. *Phil. Trans. Roy. Soc. London*, 360(1792):437–451, 2002.

- [98] M. Sbragaglia and D. Belardinelli. Interaction pressure tensor for a class of multicomponent lattice boltzmann models. *Physical Review E*, 88:1–6, 2013.
- [99] M. Sega, M. Sbragaglia, S. Kantorovich, and A. Ivanov. Interaction pressure tensor for a class of multicomponent lattice boltzmann models. *Soft Matter*, 9:10092–10107, 2013.
- [100] Q. Zou and X. He. On pressure and velocity boundary conditions for the lattice boltzmann bgk model. *Physics of Fluids*, 9(6):1070–6631, 1997.
- [101] K. Mattila, J. Hyv aluoma, and T. Rossi. Mass-flux-based outlet boundary conditions for the lattice boltzmann method. *Journal of Statistical Mechanics: Theory and Experiment*, 2009:1742–5468, 2009.
- [102] M. Hecht and J. Harting. Implementation of on-site velocity boundary conditions for d3q19 lattice boltzmann simulations. *Journal of Statistical Mechanics: Theory and Experiment*, 2010:1742–5468, 2010.
- [103] F. Greco. Drop deformation for non-newtonian fluids in slow flows. *J. Non-Newtonian Fluid Mech.*, 107:111–131, 2002.
- [104] S. Guido, M. Simeone, and F. Greco. Deformation of a newtonian drop in a viscoelastic matrix under steady shear flow: Experimental validation of slow flow theory. *Journal of non-newtonian fluid mechanics*, 114(1):65–82, 2003.
- [105] V. Sibillo, M. Simeone, S. Guido, F. Greco, and P. L. Maffettone. Start-up and retraction dynamics of a newtonian drop in a viscoelastic matrix under simple shear flow. *Journal of non-newtonian fluid mechanics*, 134(1):27–32, 2006.
- [106] K. N. Premnath and J. Abraham. Three-dimensional multi-relaxation time (mrt) lattice Boltzmann models for multiphase flow. *Journal of Computational Physics*, 224:539–559, 2007.
- [107] M. Tom e, L. Grossi, A. Castelo, J. Cuminato, S. McKee, and K. Walters. Die-swell, splashing drop and a numerical technique for solving the oldroyd-b model for axisymmetric free surface flows. *J. Non-Newtonian Fluid Mech.*, 141:148–166, 2007.

- [108] P. L. Maffettone and F. Greco. Ellipsoidal drop model for single drop dynamics with non-newtonian fluids. *Journal of Rheology (1978-present)*, 48(1):83–100, 2003.
- [109] P. L. Maffettone, F. Greco, M. Simeone, and S. Guido. Analysis of start-up dynamics of a single drop through an ellipsoidal drop model for non-newtonian fluids. *Journal of non-newtonian fluid mechanics*, 126(2):145–151, 2005.
- [110] S. Guido and M. Villone. Three-dimensional shape of a drop under simple shear flow. *Journal of Rheology*, 42(2):395–415, 1998.
- [111] H. A. Stone. Dynamics of drop deformation and breakup in viscous fluids. *Annu. Rev. Fluid Mech.*, 26:65–102, 1994.
- [112] K. Verhulst, R. Cardinaels, P. Moldenaers, Y. Renardy, and S. Afkhami. Influence of viscoelasticity on drop deformation and orientation in shear flow part 1. stationary states. *J. Non-Newt. Fluid Mech.*, 156:29–43, 2009.
- [113] K. Verhulst, R. Cardinaels, P. Moldenaers, S. Afkhami, and Y. Renardy. Influence of viscoelasticity on drop deformation and orientation in shear flow. part 2: dynamic. *J. Non-Newt. Fluid Mech.*, 156:44–57, 2009.
- [114] S. Mukherjee and K. Sarkar. Effects of viscoelasticity on the retraction of a sheared drop. *Journal of Non-Newtonian Fluid Mechanics*, 165(7):340–349, 2010.
- [115] R. Cardinaels and P. Moldenaers. Relaxation of fibrils in blends with one viscoelastic component: From bulk to confined conditions. *Journal of Polymer Science Part B: Polymer Physics*, 48(12):1372–1379, 2010.
- [116] P. Yue, J. J. Feng, C. Liu, and J. Shen. A diffuse-interface method for simulating two-phase flows of complex fluids. *J. Fluid Mech.*, 515:293–317, 2004.
- [117] M. Minale. Deformation of a non-newtonian ellipsoidal drop in a non-newtonian matrix: extension of maffettone-minale model. *J. Non-Newtonian Fluid Mech.*, 123:151–160, 2004.

- [118] P. Yue, J. J. Feng, C. Liu, and J. Shen. Viscoelastic effects on drop deformation in steady shear. *J. Fluid Mech.*, 540:427–437, 2005.
- [119] R. G. M. van der Sman and S. van der Graaf. Emulsion droplet deformation and breakup with lattice Boltzmann model. *Comput. Phys. Commun.*, 178:492–504, 2008.
- [120] K. Verhulst, P. Moldenaers, and M. Minale. Drop shape dynamics of a newtonian drop in a non-newtonian matrix during transient and steady shear flow. *Journal of Rheology (1978-present)*, 51(2):261–273, 2007.
- [121] N. Ioannou, H. Liu, and Y. H. Zhang. Droplet dynamics in confinement. *Journal of Computational Science*, 17:463–474, 2016.
- [122] M. E. Kutaya, A. H. Aydilek, and E. Masad. Laboratory validation of lattice Boltzmann method for modeling pore-scale flow in granular materials. *Computers and Geotechnics*, 33:381–395, 2006.
- [123] K. Mattila, J. Hyväluoma, A. A. Folarin, and T. Rossi. A boundary condition for arbitrary shaped inlets in lattice-boltzmann simulations. *International Journal for Numerical Methods in Fluids*, 63:638–650, 2009.
- [124] I. Ginzbourg and D. d’Humières. Local second-order boundary methods for lattice boltzmann models. *Journal of Statistical Physics*, 84:927–970, 1996.
- [125] T. Inamuro, M. Yoshino, and F. Ogino. A boundary condition for arbitrary shaped inlets in latticeboltzmann simulations. *Physics of Fluids*, 7, 1995.
- [126] R. S. Maier, R. S. Bernard, and D. W. Grunau. Boundary conditions for the lattice boltzmann method. *Physics of Fluids*, 8, 1996.
- [127] E. G. Flekkøy, G. Wagner, and J. Feder. Hybrid model for combined particle and continuum dynamics. *Europhysics Letters*, 52:271–276, 1996.
- [128] R. Delgado-Buscalioni and P. V. Coveney. Continuum-particle hybrid coupling for mass, momentum, and energy transfers in unsteady fluid flow. *Physical Review E*, 67(046704), 2003.

- [129] R. Delgado-Buscalioni, K. Kremer, and M. Praprotnik. Concurrent triple-scale simulation of molecular liquids. *The Journal of Chemical Physics*, 128(114110), 2008.
- [130] E. Guazzelli and J. Morris. *A Physical Introduction to Suspension Dynamics*. Cambridge University Press, 1st edition, 2012.
- [131] M. P. Allen and D. J. Tildesley. *Computer Simulation of Liquids*. Oxford University Press, 1st edition, 1987.
- [132] W. H. Press, S. H. Teukolsky, W. T. Vetterling, and B. P. Flannery. *Numerical Recipes in C*. Cambridge University Press, 2nd edition, 1992.

Summary

This thesis deals with the numerical study of the dynamics and instability of a single droplet in complex flows, such as laminar time-dependent and turbulent flows. The numerical model to be used is the Lattice Boltzmann Method (LBM), which is able to accurately simulate fully resolved multicomponent flows with the help of a diffuse interface method. We have developed a novel LBM boundary scheme, which enables us to study droplets in turbulent flows on the sub-Kolmogorov scale. Turbulent droplet dynamics is a multiscale problem, because information from both the droplet and the largest turbulent scales are needed. Therefore the LBM boundary scheme must simulate arbitrary velocity fields at the domain boundary, which in case of this thesis are velocity fields of laminar oscillatory flows and homogenous and isotropic turbulent flows. Moreover, the LBM results are compared with the solutions to a phenomenological droplet deformation model, the Maffettone-Minale model (MM-model). In order to test the new LBM boundary scheme, we considered the case of droplet dynamics in a confined and oscillatory shear flow. We find that the LBM results and the results of a confined version of the MM-model match well. Furthermore, we considered the case of high frequency oscillatory shear flows in relation to the droplet relaxation time and analysed the “transparency effect”, for which the droplet is only marginally deformed, even in the case of large flow amplitudes. Additionally, we investigated LBM breakup predictions of a droplet in an oscillatory confined flow, in relation to the oscillatory frequency, the degree of confinement, inertial effects, flow start up conditions and flow topology. The LBM breakup simulations suggest that breakup in confined stationary shear flows may lead to different breakup conditions for different flow start up conditions in the presence of strong confinement. This mismatch between the LBM breakup results vanishes in the presence of small perturbations, such as small flow amplitude variations in an oscillatory shear flow. The newly developed LBM boundary scheme would allow for the introduction of an external turbulent flow field. This is achieved by using data of passive tracer trajectories in homogenous and isotropic

turbulent flows obtained via pseudo-spectral simulations. After rescaling and finding a suitable sampling algorithm of the turbulent flow data, we can recover the correct single phase linear turbulent velocity profile. This multiscale hybrid LBM algorithm is now suitable to predict sub-Kolmogorov droplet dynamics and breakup. We find, that the results of both LBM and the MM-model for the deformation dynamics agree well with each other for small capillary numbers. However, LBM yields different deformation and breakup predictions than the one of the MM-model in the large capillary number regime. This is due to the fact that the LBM hybrid scheme is able to model a fully resolved turbulent multicomponent flow, contrary to the MM-model simulations. This work investigates the effect of explicit flow time-dependencies for droplet deformation in confined shear flows, with the help of new LBM boundary method. Furthermore, this boundary method is extended to a novel multiscale hybrid LBM algorithm used to model a fully resolved sub-Kolmogorov droplet in homogeneous and isotropic turbulence. The work in this thesis also demonstrates the versatility of LBM and DNS-LBM hybrid algorithms for both multiphase and multicomponent flows in particular.

Acknowledgement

“The whole is more than the sum of its parts.” Even though this thesis displays the findings of my PhD research, it does not provide the complete picture of my development during my PhD research programme both professionally and personally. I would like to thank everyone who has been a part of it and made the four years of PhD research that much more enriching. First of all I thank my promoters, Prof. Luca Biferale, Prof. Mauro Sbragaglia and Prof. Federico Toschi. Through your expert knowledge and guidance I was able to tackle challenging numerical and multiphysics problems in my research project. In particular, I am grateful for the in-depth discussions on several problems regarding the research direction and content of this project. And last but not least, thank you for encouraging me to go to several schools and trainings to broaden my knowledge and giving me the opportunity to present my research results at international conferences worldwide. My gratitude also goes to Prof. Matthias Erhardt and Prof. Andreas Bartel who gave me the possibility to present my work at a different angle to a numerics audience and with whom I had stimulating discussions about Lattice Boltzmann boundary flows. I also thank the PhD defense committee members, Prof. Patrick Anderson, Prof. Luca Brandt and Dr. Wim-Paul Breugem for reviewing this thesis. I also thank the organisers of my European Joint Doctorate programme HPC-LEAP and the Marie Skłodowska-Curie Actions for making the research presented here possible.

I would particularly like to thank my fellow HPC-LEAP PhD researchers, Alessandro, Srijit, Slava, Simone, Wenping, Andy, Aurora, Salvatore, Ibo, Thomas, Teo and Vanessa. Special thanks goes to Guillaume, who would never lose his sense of optimism in stressful times and always was a source of encouragement to the other HPC-LEAP fellows. Starting a new job abroad is by no means easy, I was thus glad to be at the same institution as Georgios, a great friend with whom the start of the project was just a little easier. Colleagues don't necessarily become close friends, but work just feels much less of a burden, if they do. I am very happy that my research project was

closely linked to the one of Xiao. Not only was I able to learn a lot from you, be it programming related or a first understanding of Chinese culture, but also developed a very close friendship.

My gratitude also goes to my colleagues and friends at Rome Tor Vergata, Anupam, Riccardo, Massimo, Matteo, Claudio, Roberto, Simona and Tadeja. I thank Michele especially, who was not tired to help out every new PhD student with the encumbering Roman bureaucracy and made sure that the Leapers were feeling comfortable in Rome, even if some of them just dropped in for a conference. In particular, I thank Nhut and Abhi for organising the evening football matches. I would also like to thank Olmo, Maria, Nesrine, Daniele and Henriët for organising great house parties and always having an upbeat dynamics, no matter where or when.

A big thank you goes out to Marjan Rodenburg, who with great care and dedication handled every problem my colleagues and I were throwing at her. I would also like to thank my friends and colleagues at the department, Abhineet, Andres, Andrej, Alessandro, Arnab, Cosimo, Gianluca, Gianmarco, Giorgia, Hadi, Haijing, Han, Jonathan, Karun, Kim, Matteo, Rik, Marlies, Marteen, Sam, Sebastian, Steven, Vignesh and Twan. Special thanks goes to my officemates Pinaki and Abheeti, it was a privilege to share an office with you and I will dearly miss the office banter and I'm especially thankful for giving me a glimpse into Indian culture during the Bangalore trip. Furthermore, my gratitude goes to Bijan and Lenin. It was just that much easier to settle into Eindhoven with you, be it because of the coffee break discussions, campus walks or the weekend get-togethers.

I also thank my (mostly) non-academic friends in Eindhoven, Alejo, Calin, Marco, Mohit, Oscar, Santosh, Stefan, Ruxi and Ivan. I would also like to thank my family, my parents and my sisters, for their unwavering support during my PhD, especially during the more difficult times. And finally I am thankful for your understanding and loving support Diana, particularly during the stressful times of the writing process.

Curriculum Vitae

Felix Milan was born on November 22, 1990 in Bamberg, Germany. He studied physics at the University of Bayreuth with a focus on theoretical and computational physics in his final research project on applications of density functional theory to organic solar cells. After obtaining his B.Sc. degree, he moved to Leiden University for his M.Sc. studies in physics with a research focus in theoretical physics. He graduated cum laude with a theoretical and computational research project on chiral phase transitions of frustrated nematic systems. In 2015 he obtained a Marie-Curie fellowship to start in October 2015 a four year Joint European Doctorate in theoretical and applied physics at the University of Rome Tor Vergata and Eindhoven University of Technology. The results of this research programme are presented in this dissertation. He works at ASML, Veldhoven, as a functional metrology design engineer since October 2019.

Cover Illustration

Snapshot of a deformed sub-Kolmogorov droplet in a homogenous and isotropic turbulent flow. The contour of the droplet is shown in light grey, whereas the flow is visualised via streamlines, which are colour coded in terms of the velocity magnitude, increasing from blue to red. The simulation parameters (in lbu) are: radius of the initially undeformed droplet $R = 40$, the domain length $L_s = 288$ and $Re_\lambda = 420$.

List of publications and conferences

Journal articles

- F. Milan, L. Biferale, M. Sbragaglia and F. Toschi, *Sub-Kolmogorov droplet dynamics in isotropic turbulence using a multiscale Lattice Boltzmann scheme*, (submitted to Journal of Computational Science)
- F. Milan, L. Biferale, M. Sbragaglia and F. Toschi, *Lattice Boltzmann simulations of droplet breakup in confined and time-dependent flows*, (submitted to Physical Review Fluids)
- F. Milan, M. Sbragaglia, L. Biferale and F. Toschi, *Lattice Boltzmann simulations of droplet dynamics in time-dependent flows* European Physical Journal E, 2018, 41:6. <https://doi.org/10.1140/epje/i2018-11613-0>

Conferences contributions

- F. Milan, L. Biferale, M. Sbragaglia and F. Toschi, *Multi-scale LBM simulations of droplets in time-dependent flows*, Burgers Symposium 2017, Lunteren, the Netherlands, May 2017
- F. Milan, L. Biferale, M. Sbragaglia and F. Toschi, *Multi-scale LBM simulations of droplets in time-dependent flows*, 26th International Conference on Discrete Simulation of Fluid Dynamics, Erlangen, Germany, July 2017
- F. Milan, L. Biferale, M. Sbragaglia and F. Toschi, *Multi-scale LBM simulations of droplets in time-dependent flows*, 70th Annual Meeting of the American Physical Society Division of Fluid Dynamics, Denver, USA, November 2017

- F. Milan, L. Biferale, M. Sbragaglia and F. Toschi, *Lattice Boltzmann simulations of droplet dynamics in time-dependent flows (poster)*, Physics@Veldhoven 2018, Veldhoven, the Netherlands, January 2018
- F. Milan, L. Biferale, M. Sbragaglia and F. Toschi, *Multi-scale LBM simulations of droplets in generic time-dependent flows*, COST Action MP1305: Flowing Matter 2018, Lisbon, Portugal, February 2018
- F. Milan, L. Biferale, M. Sbragaglia and F. Toschi, *Lattice Boltzmann study of droplet dynamics and break-up in generic time-dependent flows*, 27th International Conference on Discrete Simulation of Fluid Dynamics, Worcester MA, USA, June 2018
- F. Milan, L. Biferale, M. Sbragaglia and F. Toschi, *Lattice Boltzmann study of droplet dynamics and break-up in generic time-dependent flows*, HPC-LEAP Concluding Conference, Cambridge, UK, July 2018
- F. Milan, L. Biferale, M. Sbragaglia and F. Toschi, *Lattice Boltzmann study of droplet dynamics and break-up in generic time-dependent flows*, 71st Annual Meeting of the American Physical Society Division of Fluid Dynamics, Atlanta, USA, November 2018
- F. Milan, L. Biferale, M. Sbragaglia and F. Toschi, *Multi-scale Lattice Boltzmann simulations of droplets in time-dependent and turbulent flows (poster)*, Physics@Veldhoven 2019, Veldhoven, the Netherlands, January 2019
- F. Milan, L. Biferale, M. Sbragaglia and F. Toschi, *Multiscale Lattice Boltzmann simulations of droplet dynamics in turbulent flows*, Burgers Symposium 2019, Lunteren, the Netherlands, May 2019
- F. Milan, L. Biferale, M. Sbragaglia and F. Toschi, *Multiscale Lattice Boltzmann simulations of droplet dynamics in turbulent flows*, 28th International Conference on Discrete Simulation of Fluid Dynamics, Bangalore, India, July 2019
- F. Milan, L. Biferale, M. Sbragaglia and F. Toschi, *Multiscale Lattice Boltzmann simulations of droplet dynamics in turbulent flows*, 17th European Turbulence Conference, Turin, Italy, September 2019

Invited talks

- F. Milan, L. Biferale, M. Sbragaglia and F. Toschi, *Lattice Boltzmann simulations of droplet dynamics in time-dependent flows*, Università degli Studi Niccolò Cusano, Rome, Italy, December 2017
- F. Milan, L. Biferale, M. Sbragaglia and F. Toschi, *The Lattice Boltzmann Method and applications for time-dependent multi component flows*, Bergische Universität Wuppertal, Wuppertal, Germany, March 2018

Journal articles out of scope of this thesis

- C. Schwarz, F. Milan, T. Hahn, M. Reichenberger, S. Kümmel and A. Köhler, *Ground State Bleaching at Donor-Acceptor Interfaces*, *Advanced Functional Materials*, 2014, 24, 64396448, 10.1002/adfm.201400297